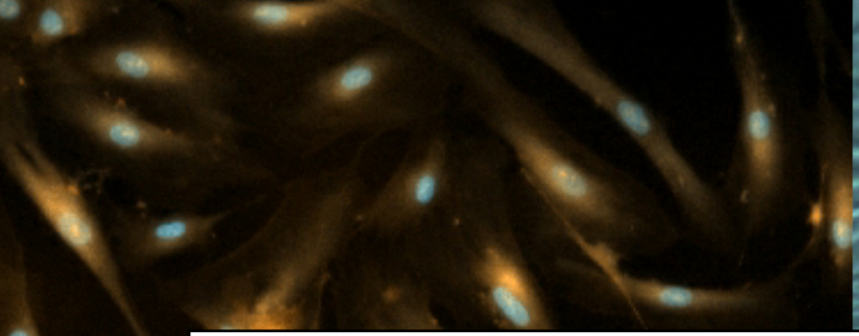
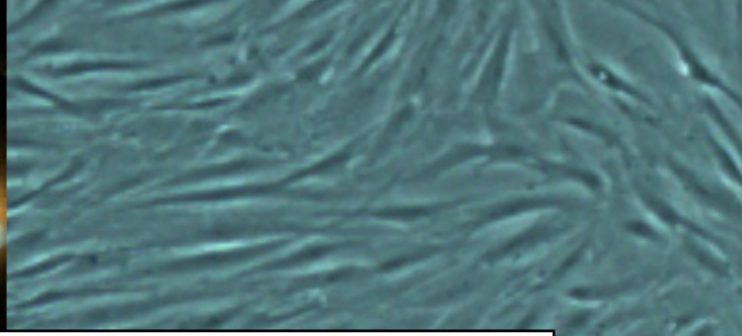

Polymeric Drug Delivery Systems

Camilla Lystlund Andersen

Master Thesis in Nanobiotechnology, February 3, 2017
Department of Physics and Nanotechnology, Aalborg University

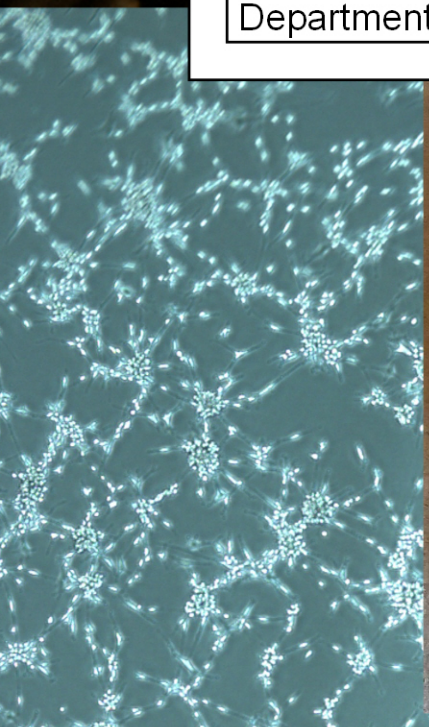

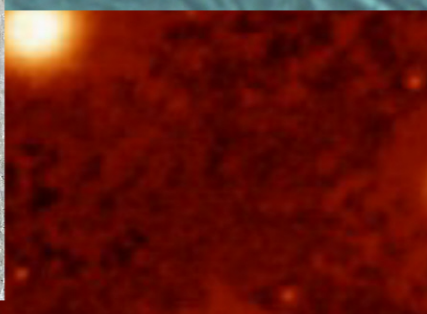
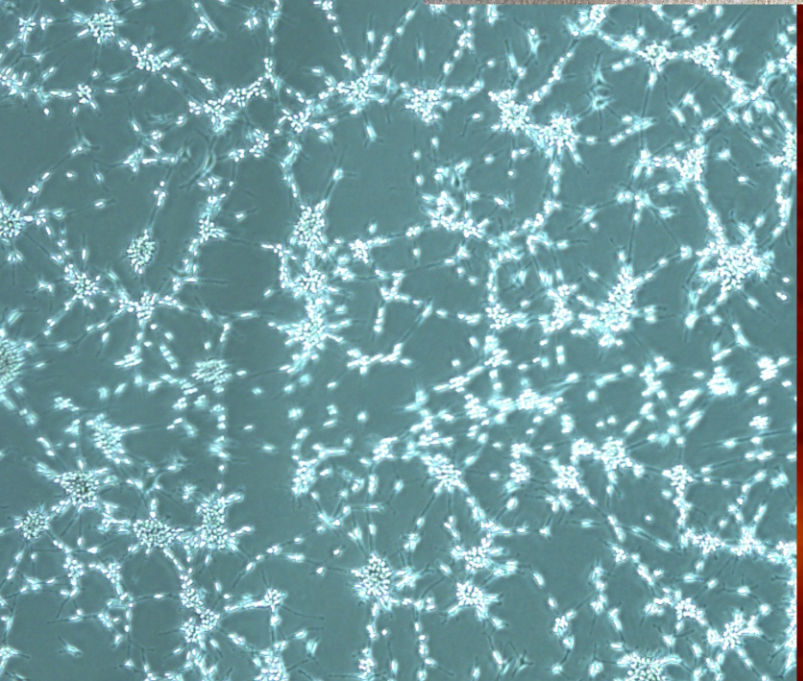
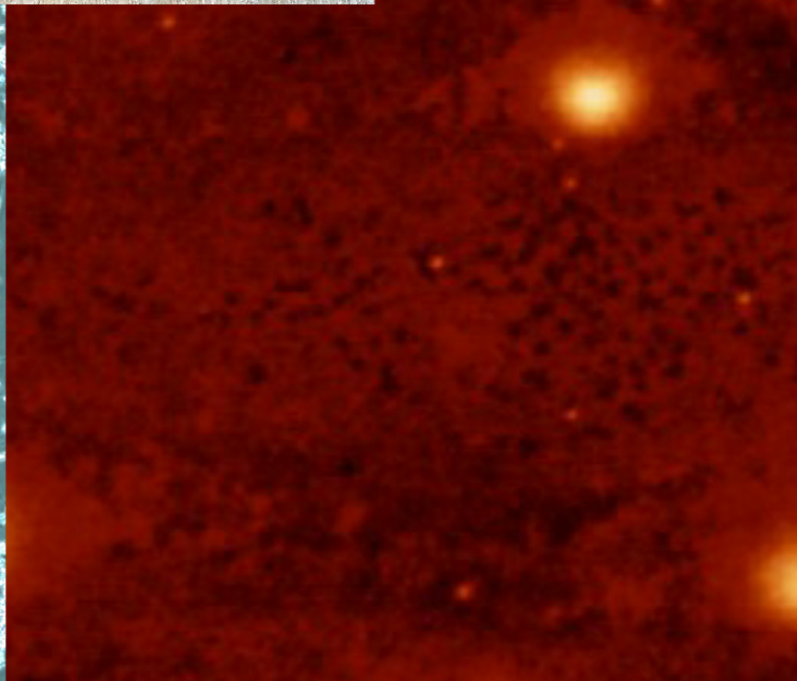

Department of Physics and Nanotechnology
The Faculty of Engineering and Science
Aalborg University
Skjernvej 4A
DK-9220 Aalborg Ø, Denmark
Telephone 9940 9215
Fax 9940 9235
http://nano.aau.dk

Theme: Avanced Nanobiotechnology
Titel: Polymeric drug delivery systems
Project period: Master, 9^{th} and 10^{th} semester 2016

Participants:

Camilla Lystlund Andersen

Supervisor:
Leonid Gurevich

Copies: 3
Pagecount:90
Total Pagecount:100
Number of Appendixes: 2

Completed: February 3, 2017

Abstract:

This Master project addresses the potential application of polyvinylpyrrolidone-based polymer micelles as a drug delivery system. 1 and 6 kDa polymer was used to form either micelles loaded with curcumin as a model hydrophobic drug, or to create empty micelles by applying chloroform as a temporary hydrophobic stabiliser. The physical properties of the synthesised micelles were studied using Nanoparticle Tracking Analysis to determine the size distribution of the micelles, and Atomic Force Microscopy to visualize them. Glioblastoma (U87) and Fibroblast (CRL 2429) cell lines were used for in vitro studies of the application of polymeric micelles in drug delivery, with the main focus being on the mechanisms of drug uptake in the cells as well as cytotoxicity. The cellular uptake of curcumin in micellar- and free form was studied using Optical Fluorescent Microscopy. Cytotoxicity assays were used to determine the mortality of the cell lines, when incubated with different concentrations of micellar and free curcumin, as well as empty micelles, for 24 hours. The studies of endocytosis mechanisms were carried out using different endocytosis inhibitors including dynasore, worthmaninn and sodium azide, followed by either microscopic visualization of the cells or cytometry measurements. Although no final conclusion was reached on the uptake mechanism, it was successfully demonstrated that the micellar form of curcumin drastically enhances the uptake and efficacy of the drug formulation, as compared with the free form.

Institut for Fysik og Nanoteknologi
Det Teknisk-Naturvidenskabelige Fakultet
Aalborg Universitet
Skjernvej 4A
9220 Aalborg Ø, Danmark
Telefon 9940 9215
Fax 9940 9235
`http://nano.aau.dk`

Tema: Avanceret Nanobioteknologi
Title: Polymerisk drug delivery system
Project period: Master 9. og 10. semester 2016

Deltagere:

Camilla Lystlund Andersen

Vejleder:
Leonid Gurevich

Kopier:3
Side antal:90
Total side antal:100
Antal af appendix: 2

Afsluttet: Februar 3, 2017

Abstrakt:

Dette speciale projekt omhandler potentielle anvendelser af polyvinylpyrrolidone-baserede polymer miceller som et drug delivery system. 1 og 6 kDa polymer blev anvendt til at danne enten miceller fyldt med curcumin som et karakteristisk hydrofobt lægemiddel; eller tomme miceller ved anvendelse af kloroform, som en midlertidig hydrofob stabilisator. De fysiske egenskaber af de syntetiserede miceller blev undersøgt ved anvendelse af Nanoparticle Tracking Analysis for at bestemme størrelses fordelingen af micellerne og atomar kraft mikroskopi til at visualisere dem. Glioblastoma (U87) og fibroblast (CRL 2429) celle linjer blev anvendt til in vitro undersøgelser i anvendelsen af polymer miceller til drug delivery, med hovedfokus påmekanismerne bag optagelsen af lægemidlet i cellerne, samt den cytotoksiske effekt. Den cellulære optagelse af curcumin i micellær- og fri form blev undersøgt ved brug af optisk fluorescens mikroskopi. Cytotoksisk analyse blev anvendt til at bestemme dødeligheden af cellelinjerne, når de blev induceret med forskellige koncentrationer af micellær- og fri curcumin, samt tomme miceller i 24 timer. Undersøgelserne af endocytose mekanismer blev udført under anvendelse af forskellige endocytose hæmningsstoffer, heriblandt dynasore, worthmaninn og natriumazid, efterfulgt af enten mikroskopisk visualisering af cellerne eller cytometri målinger. Selvom ingen endelig konklusion blev nået for optagelsesmekanismerne, blev der med succes vist at den micellære form af curcumin drastisk øger optagelsen og effekten af lægemidlets formulering sammenlignet med i den frie form.

Preface

This master project was written by Camilla L. Andersen a master student studying Nanobiotechnology, at the department of Physics and Nanotechnology at Aalborg University. The master project began the 2^{nd} of February 2016 and ended February 3^{th} 2017. The theme for the project is "Advanced Nanobiotechnology".

Reading guide: Reference to various sources, throughout this project are listed as [$*$], where the number refers to a specific source in the bibliography. The bibliography is placed in the end of the project, where the sources will be listed with their title, author and other relevant information, depending on the form of the source (Book, article etc.). For the most parts the references are listed after a specific section in which they are used, indication that the reference applies to the entire section.

Tables and figures are numbered in the order of appearance per chapter e.g. Figure 4.1, denotes the first figure in chapter 4. Each table and figure has a brief caption, which can also contain a reference.

Special thanks and recognition are given to *Christian Pablo Pennisi* and *Ole Jensen* for their help and guidance at the Laboratory for Stem Cell Research at Aalborg University.

Abbreviations:

IARC	International Agency for Research on Cancer
MPS	Mononuclear Phagocyte System
DDS	Drug delivery systems
BBB	Blood-brain barrier
CNS	Central nervous system
API	Active pharmaceutical ingredient
EPR	Enhanced Permeability and Retention effect
CMC	Critical Micelle Concentration
Nano-bio	Nanomaterial/biological
VDW	Van der Walls forces
DLVO	Derjaguin-Landau-Verwey-Overbeek
DMSO	Dimethyl sulfoxide
FBS	Foetal Bovine Serum
LDH	Lactate Dehydrogenase
MRI	Magnetic resonance imaging
NIH	National Institutes of Health
ECM	Extracellular matrix
APTMS	(3-Aminopropyl)trimethoxysilane
EtOH	Ethanol
EDTA	Ethylenediaminetetraacetic acid
CRL 2429	Fibroblast
U87	Glioblastoma
P/S	Pernicillin/Streptomycin
PBS	Phosphate-buffered saline
PVP	Polyvinylpyrrolidone
T	Trypsin
AFM	Atomic Force Microscope
NTA	Nanoparticle tracking analysis
CM	Curcumin Micelles
FSC	Forward scatter
SSC	Side scatter

Contents

1. Introduction

On a global scale, the spectrum of disease known as cancer is one of the most common causes of death. In 2008 alone around 12 million patients were diagnosed with cancer, with 25 million people already living with the disease and an estimate of 7 million cancer-related deaths. In the future, the continuing growth of the worlds population coupled with longer lifespans will result in these numbers only growing larger and are expected to almost double by 2030 according to the International Agency for Research on Cancer (IARC).[1, 2]

Cancer is not a new disease. While it can be traced back hundreds of years, with the earliest documented cases being found in Egyptian mummies [3, 4], it is only recently that our understanding of it has improved enough for it to be treated. However, today the treatment of cancer still remains one of the most challenging problems in medicine, and with the increasing numbers of patients, the pressure for more advanced treatment methods is high. Some of the current treatment methods are surgical intervention, radiation therapy and chemotherapy, but they are not without concerns.[2, 5]

In 1996 Michael Baum hypothesised [6] that surgical removing of tumours could cause an acceleration of tumour growth and metastatic growth, perhaps induced by the inflammatory response during wound healing. These effects may account for the poor survival benefits, when only a single method is used. This indicates that a second method to stop the continuing growth of cancer cells is necessary. Chemotherapy is an essential secondary treatment, although its efficiency is far from satisfactory. Traditional chemotherapy drugs are far from healthy towards the patient, as they are toxic to healthy cells as well as cancer cell. These problems are mainly caused by poor specificity in drug delivery, including problems with physiological barriers and drug resistance.[2, 7]

In order to improve the treatment methods further, the development of new drug delivery systems is driven by the demand to maximize the effect of the medicine and minimize the side effects. Several drug carriers have been developed as potential carriers: liposomes, micro-particles, nano-associates, nanoparticle, drug polymer-conjugates and polymeric micelles. A promising method, which has been extensively studied in the past decade includes micelles formed through self-assembly. They exhibit a number of properties, such as their small size ($<$100 nm), their ability to solubilize hydrophobic drugs in their core, while the hydrophilic corona interacts with the aqueous environments and forms hydrogen bonds. The hydrogen bonds form a tight shell around the micelles and prevent protein adsorption and cellular adhesion. This hydrophilic corona protects the micelles from the detection by the mononuclear phagocyte system (MPS) and as reduces their excretion, hence prolonging their circulation in the blood stream.[8, 9]

1.1 Drug delivery

Drug delivery systems (DDS) are methods or processes for administrating the introduction of a therapeutic agent into the body. DDS can improve the therapeutic agent exposure and efficacy by controlling parameters such as the release rate, time and location in the body. DDS processes include three concepts: the administration of the therapeutic product delivered to the destination, the release of the active additive by the product and the transport of the active additives across a biological membrane to the place of action.[10]

The DDS works as an integration between the patient and the therapy. It can be formed as a device to deliver the therapy or it can be a way for the therapy to fulfil its purpose. Nonetheless, it is of great importance to distinguish between the therapy and the device, since it is a criterion for the administrative control of the DDS by the various medicine control agencies. When a device loaded with a therapeutic agent is introduced in to a body, with the purpose of drug administrating, it is considered a drug. If the device, on the contrary, is loaded with a drug, ifs purpose is to prevent complications resulting from this device; it is then regulated as a device. The spectra between the category of drug and device are very wide, making the allocation decide on a cases to cases basis.[10]

1.1.1 Routes of delivery

A therapeutic drug can be administered into the human body by various anatomical routes. The choice of delivery route depends on three factors: the disease, the product and the desired effect. Depending on the situation, the drug can be directly administrated into the affected organ, or given systemically, or be targeted to the affected organ.[10, 11] There are various methods for a systemic drug delivery by anatomical routes; these can be seen in table 1.1. Some of the most frequent routes used for drug administration are oral and injections.

Table 1.1: *A classification of various systemic drug delivery methods by anatomical routes. Inspired by Kewal K. Jain [10].*

Delivery routes
Gastrointestinal system
- Oral
- Rectal
Parenteral
- Subcutaneous parenteral
- Intramuscular parenteral
- Intravenous parenteral
- Intra-arterial parenteral
Transmucosal: buccal and through mucosa lining the rest of gastrointestinal tract
Transnasal
Pulmonary: drug delivery by inhalation
Transdermal drug delivery
Intra-osseous infusion

1.1.1.1 Oral delivery

From a historical point of view, the oral route of drug administration is the oldest and most applied route for novel and conventional drug delivery. The reasons for its preference are the easy administration as well as the fact that the patients are more accepting towards it. However

the oral route has various limitations, depending on the properties of the drug. The absorption rate of drugs for systemic effect can vary in a non-predictable way. High concentrations of acids and digestive enzymes in the digestive tract can degrade drugs by making them unsolvable before they reach the bloodstream. The oral route may not be suitable for drugs targeted to specific organs. Several improvements have been implemented recently, in the formulation of drugs for oral delivery, to preserve their action.[10, 11]

1.1.1.2 Delivery by parenteral

Parenteral administration is an essential part of the medical practice and is the most commonly used invasive method of drug delivery. The parenteral route is the most effective route for delivering of active pharmaceutical substances with poor bioavailability and narrow therapeutic index, into the body, because it bypasses the intestinal tract. There are various routes of parenteral administration available, the most generally applied, include intramuscular, intravenous, intra-arterial and subcutaneous routes.[10, 11, 12, 13]

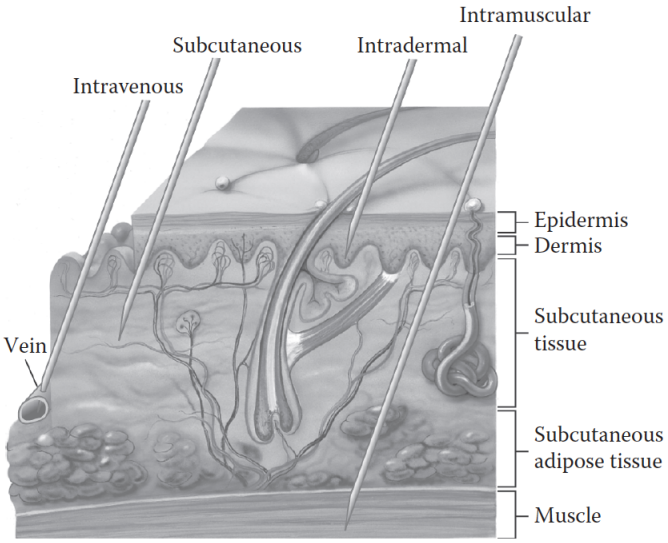

FIGURE 1.1: *The generally applied routes of parenteral administration. Taken from Ochoa et al. [12].*

The advantages of parenteral administration include rapid onset action and predictable and rather complete bioavailability. Furthermore, it is a very reliable drug delivery route, especially for patients that are comatose or too ill to ingest drugs orally. Patients that are bed ridden or hospitalized can also become dependent on parenteral nutritions: such as fluids, nutrients and electrolytes and many of the important pharmaceuticals are only available in injection form. Even with the many benefits, there are some drawbacks to the parenteral delivery. Firstly injection can be painful and uncomfortable for patient, which leads to complains. Secondly, there is a risk of infection, allergic reactions and embolism, as well as hypersensitivity reactions. Furthermore injection drugs are more expensive to manufacture, than conventional drugs since it requires specialized equipment, devices and techniques to prepare.[10, 12, 13]

1.1.2 Targeted drug delivery

Today the majority of applied pharmaceuticals will, upon ingestion/injection, be distributed throughout the body. A drug is transported around the body through systemic circulation without any specific direction, both upon ingestion and injection. In order for a drug to reach an affected site, it has to cross different biological barriers, as well as organs, cells and intracellular compartments. During this transportation, the drug can produce unwanted side effects on organs and tissues, or it can become inactivated. Therefore, in order to achieve the required concentration of a drug at a given affected site, it has to be administered in high quantities, where a large part of it ends up in normal healthy tissue.[14, 15]

The wasted part of the administrated drug can in some situations, depending on the drug, cause a lot of damage in the body, leading to unwanted and negative side effects.[14] A classical and common example of this is chemotherapy. Chemotherapy is used to treat different types of cancers by attacking the active cells. Cancer cells are active cells that are dividing and growing, but the same can be said of many healthy cells, which are found in human blood, digestive system, hair follicles and in the mouth. When chemotherapy drugs are being circulated throughout the body in high quantities, they can cause side effect by attacking healthy cells. These side effects differ depending on the drug and the patient receiving them.[16]

In order for chemotherapy to be a clinically effective form of treatment, the amount of drug at the target site has to maintain a desired concentration level for a sufficient time. A region of the body where this is especially difficult, is in the brain. The blood-brain barrier (BBB) prevents most therapeutic drugs from reaching the central nervous system (CNS) from the blood circulation, making it extremely difficult to deliver drugs to the brain.[17] 100% of large-molecule drugs, e.g. peptides, gene therapies, monoclonal antibodies etc., do not penetrate the BBB; this also applies to >98% of all small molecules. In the Comprehensive Medicinal Chemistry database there are >7000 drugs, where only 5% can treat the CNS, and are limited to treatment of depression, schizophrenia and insomnia.[18] There have been developed several brain drug delivering approaches, such as intra-cerebral and intracerebroventricular administration, which are highly invasive methods, as well as intranasal delivery, a non-invasive method. These approaches are not commonly used, since they are risky, costly and not suitable for less localized brain tumours.[17] Targeting nano-material objects, which behave as a unit in terms of transport and properties, have been widely investigated for brain drug delivery. Nano-materials have been found to internalize into cells, including the brain capillary endothelial cells by endocytosis and transcytosis.[17]

Drug targeting could be the solution to all these problems. Drug targeting can be defined as a drugs ability to accumulate its active pharmaceutical ingredient (API) in a target area of the body, independently of the method or site of administration. This would ideally lead to a high concentration in the target area, while keeping the concentration in the non-target areas below certain minimum levels, to prevent negative side effects. Furthermore, drug targeting has other noticeable advantages. The quantity of the API can be reduced greatly, together with the cost of the therapy. The concentration of API at the target site, can be largely increased, without causing side effects in unrelated tissues. The administration protocols may furthermore by simplified.[14, 15]

A conceptual version of a targeted pharmaceutical drug has to contain several different components: a pharmaceutical agent, a targeting moiety, a structure capable of carrying molecules per targeted moiety to the target. Recognition of the target can occur on different

levels: organ, cellular or molecular. On the organ level, specific cells of a given organ are targeted or individual components of the cells. The same can be stated for the molecular level, since each organ or tissue has a unique component (antigens, proteins or fusion gene [19]) specific to them. Numerous methods of targeted drug delivery have been described; not all include the use of targeted moieties, as some are based on physical principles or physiological features of the targeted area.[15, 20]

1.1.2.1 Passive targeting

The so-called Enhanced Permeability and Retention (EPR) effect is considered the basis of passive targeting and is commonly mentioned, in relation with tumours, infarcts, and inflammation areas. Tumours grow quickly and require constant access to nutrients and oxygen; therefore they stimulate the production of blood vessels. Growths of blood vessels are known as angiogenesis. The fast growth leaves the endothelial cells of the blood vessels poorly aligned with large fenestrations between them. This large spaces (200 - 800 nm) allows the drug carriers to leak from the blood vessels into the tumour, as illustrated on figure 1.2. This way, the drug carriers can bring the pharmaceutical agent into the tumour with the increased vascular permeability, and release the API. The size of the fenestrations differs from case to case, making it possible to control the efficiency of the EPR effect, from the size of the drug carrier.[15, 21]

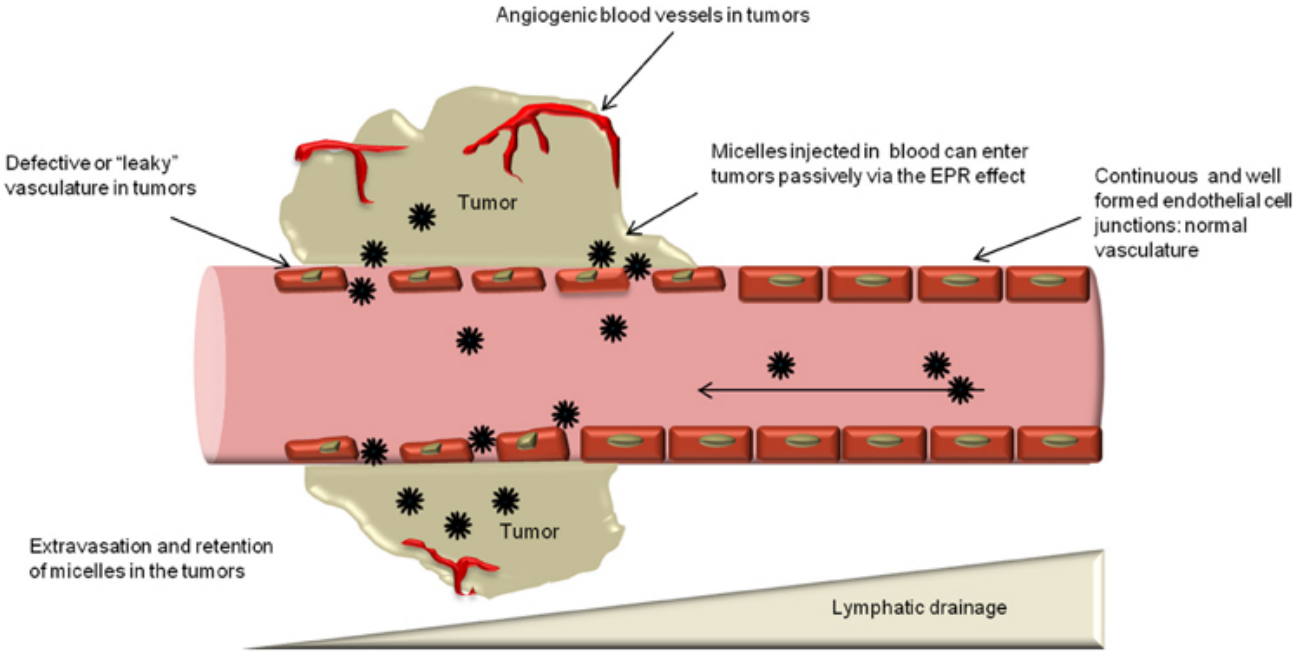

FIGURE 1.2: *A schematics of passive targeting and the EPR effect. The drug carriers (micelles) extravagate through the leaky vasculature and accumulated in the tumour, by cause of the poor lymphatic drainage. Taken from Jhaveri and Torchilin [21].*

In addition, the too fast blood vessels growth, the lymph vessels are also affected. Compressing them in the central portion of the tumour induces total collapse of the vessels, which results in poor lymphatic drainage. Both concepts allow the leakages of drug carriers and blood plasma components into the tumour, simultaneously letting them accumulate and reach a high concentration.[21]

Long-circulation time is a key component of passive targeting in order to obtain a sufficient level of accumulation in the tumour. To preserve the drug carriers in the blood circulation, the carriers are "masked" with water-soluble polymers, by grafting them on to the carriers surface.

This was proven by Torchilin and Trubetskoy [22] in their investigation of protective effect of polymers on nano-particulate drug carriers, where they look at the flexibility of polymers.[21, 22]

1.1.2.2 Active targeting

Passive targeting is an effective and valuable method, but there are some pathological situations where the vascular endothelial cells remain unaffected by the frequent growth, making no opportunity for the EPR effect to progress. The diseased area is often not that different from healthy tissue when it comes to vascular permeability, temperature and ph. A more universal and natural way of increasing drug targeting is trough active targeting. Active targeting explores the fact that certain proteins are overexpressed on the surface of the cancer cells and can be used to specifically recognise them. A wide range of moieties have been applied for the purpose, including antibodies and their fragments, peptides, proteins, sugars and small molecules (see figure 1.3).[9, 14, 15, 21, 23]

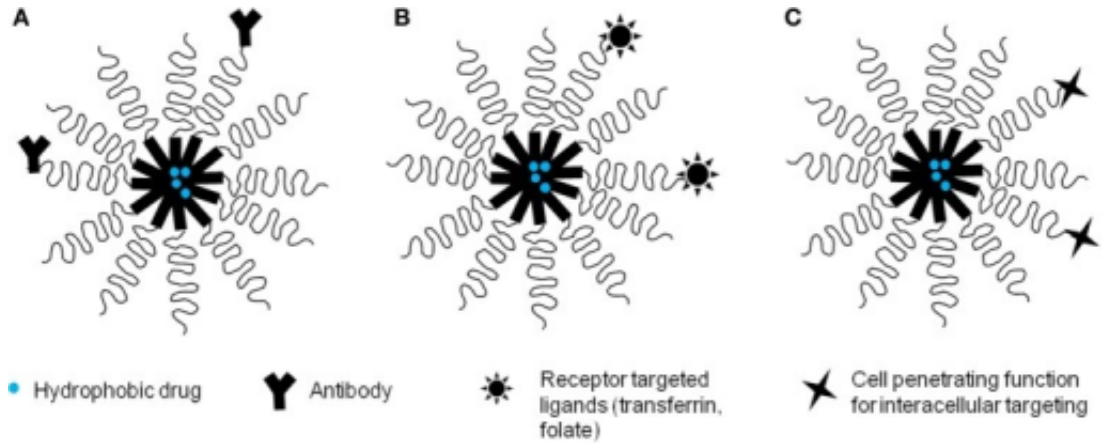

Figure 1.3: *An illustration of drug loaded micelles, with different targeting functions. Antibody-targeted micelle (**A**), ligand-targeted micelles (**B**) and micelle with a cell-penetration function (**C**). Taken from Jhaveri and Torchilin [21].*

Antibodies are the most popular and frequently applied moieties, due to the high specificity of their interactions, together with the diversity of their targets. However, although antibodies are popular, there are some challenges related to their use. When determining the effectiveness in targeted drug delivery, important parameters include blood circulation through the target, the targets size, numbers of binding sites for the target drug carrier in the target, and the number and affinity of targeting moieties on the drug carrier. One of the challenges of using antibodies is their size of ∼150 kDa, which influence the number of targeting moieties on the drug carrier, which is an important parameter to consider when determining the systems effectiveness. Other challenges include stability considerations and engineering problems during mass production.[15, 21]

1.2 Polymeric drug delivery systems

Polymeric drug delivery can potentially be a solution to many problems with conventional drug delivery, including degradation and loss of the therapeutic agent, harmful side effects and poor bioavailability.[24] The polymeric materials are in many aspects similar to the body's natural components and are chemically synthesised, making them unaffected to xenobiotic materials. Furthermore, they can be customized to achieve the desired physical and chemical properties and are therefore often used as components or supporting materials of devices to transport the therapeutic agent into the body.[25]

Polymeric DDS consist of soluble polymers, microcapsules, liposomes, micelles etc. Each of the carriers has its own advantages and dis-advantages, so the decision on which carrier to use in a specific project, requires certain consideration.[24] One of the notable factors is the carriers ability to stay in circulation. There are several reasons for the importance of long-circulation:

1. It may be necessary for the carrier to stay in the blood for long periods, in order to maintain a desired level of the therapeutic agent in the blood and to achieve a better availability.

2. Carriers can over time accumulate in pathological sites with affected vasculature such as tumours, and thereby improve or enhance the delivery to these areas. The so-called EPR effect.

3. Prolonged circulation can help achieve more efficient targeting effect for the target modified carriers.

From a clinical standpoint, it is of great importance that the various carriers are relatively small in size (100 - 200 nm), since it has been demonstrated that they effectively accumulate in tumours by the EPR effect.[24, 26] The important pathways for elimination of the long-circulation carriers are renal clearance, uptake by cells from the blood and extravasation, which are all independent processes. However, extravasation is of specific relevance, since it is an important factor for the bioavailability of the long-circulation carriers. This relevance and the importance of size have leaded to dividing the carriers into extravasation and non-extravasation ones, where the size threshold is the main difference. The non-extravasation group, where the size is above 5 - 10 nm, consists of cells, particles, larger liposomes etc. The extravasation group (below 5 - 10 nm) includes small liposomes, proteins, micelles etc., together with various polymers that are more than 40 kDa.[24]

1.2.1 Micelles

Micelles belong to a large family of dispersed systems, which are defined as systems with two or more phases with a well-defined interface. In this family, micelles belong to colloidal dispersions, which can be further divided into three principal groups: lyophilic, lyophobic and association colloids. Micelles are classified as association or amphiphilic colloid.[24]

Amphiphilic colloids are formed spontaneously by amphiphilic molecules, at certain conditions. Amphiphilic molecules consist of two distinct regions with opposite affinities towards a given solvent. At low concentration the molecules do not interact with each other in the solvent. However, increasing the concentration can result in aggregation. These aggregates contain a number of molecules in a spherical shape, and are known as micelles. The specific concentration values at which the micelles are formed are known as the critical micelle concentration (CMC).

At the CMC point, both the interface and bulk of the solvent become saturated with molecules and further increase in concentration lead to the formation of the micelle within the bulk phase. The relative CMC for amphiphilic molecules differ from each another. Micelles produced from small amphiphilic molecules have a high CMC and are unstable at high dilution values, where large amphiphilic molecule micelles have a rather low CMC, making them very stable upon strong dilution.[24]

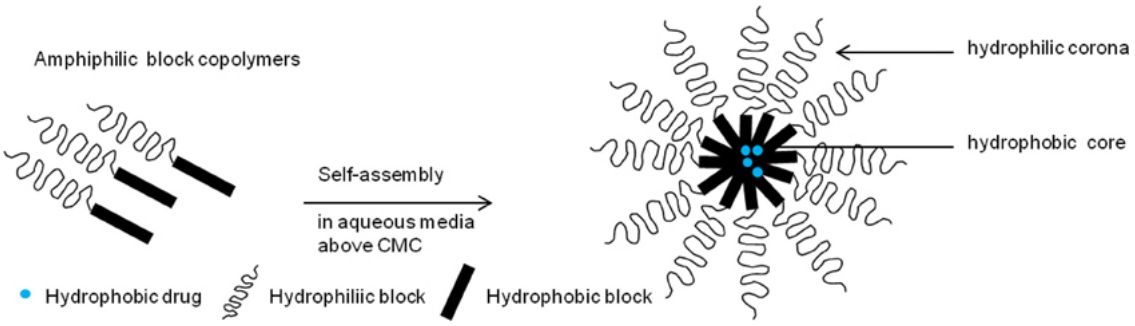

Figure 1.4: *General schematic, of formation of micelle from amphiphilic molecules. Taken from Jhaveri and Torchilin [21].*

Micelles are structured in a way that their outer surface, which is exposed to their aqueous surroundings, consists of compounds that do not react with blood or tissue components. This particularity feature allows micelles to remain in the blood for a long time, without being recognized by the immune system. This is an important feature for a drug carrier.[24, 27]

The Krafft point is another important parameter, which describes the micellization process and follows to some extend the principles of CMC. The amphiphilic polymers exist as unimers below the Krafft point and as micelles and unimers above.[24, 28]

1.2.1.1 Micellization

The formation of micelles can be understood through thermodynamics. Micelles are spontaneously formed because of the balance between entropy and enthalpy, where the driving force becomes the decrease of Gibbs free energy (G). The free energy decreases when the entropy increases as a result of core formation, which allows for packing of the hydrophobic blocks away from the aqueous environments; this is also called the hydrophobic effect. When the system is at or just above the CMC, the micelles are loose, and still contain a small percentage of water in their core. The micelle packing becomes tighter, more stable and size reducing, as the concentration of the surfactant rises above the CMC. With the increase in concentration, the remaining water is pushed out and the system equilibrium is shifted further towards micelle formation.[21, 24, 28]

At a low CMC value, the size and stability efficiency for a monomer surfactant is high. The decrease in CMC therefore results in an increase of the size and stability efficiency. This fact is of great importance from a pharmacological point of view. When micelles are used as a drug carrier in any biological system, they are diluted by biological fluids, e.g. blood. Only micelles with low CMC value will be stable at these conditions; at high CMC values the micelles will dissociate into unimers.[24, 28]

1.2.1.2 Solubilisation of micelles

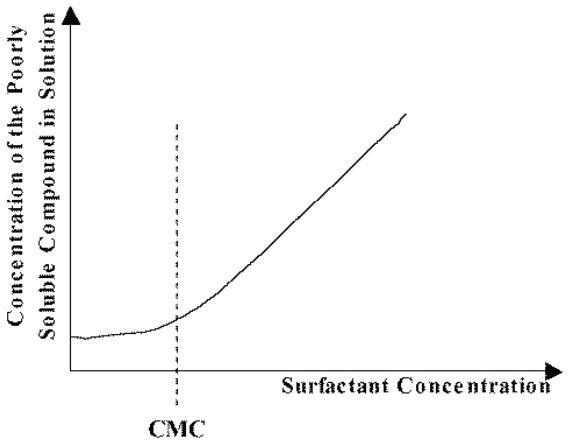

FIGURE 1.5: *A schematic plot of poorly soluble compounds vs. the concentration of the surfactant. Taken from Nell et al. [29].*

Micelles ability to increase the solubility of poor hydrophobic drugs is a significant property in the pharmaceutical industry. If the solubility of poorly soluble compounds were to be plot as a function of the concentration of surfactant, it would show that the solubility is very low until the concentration obtains CMC. This is illustrated in in figure 1.5. Above the CMC the solubility increases linearly together with the surfactant concentration, indicating that the solubility is connected to micellization.[24, 29]

Micelles formed of non-ionic surfactants are commonly known to have an anisotropic water distribution within their structure, where the water content decreases from the surface towards its core. The anisotropic water distribution leads to a polarity gradient, indicating that the spatial position of the solubilized drugs in a micelle is dependent on its own polarity. Consequently, nonpolar molecules will solubilize in the core of the micelle. Polar molecules will be absorbed on the surface, and the intermediate polarity substances will be distributed along surfactant molecules in specific intermediate positions. The micelles drug loading capacity depends on various factors like the chemical structure of the drug and the applied surfactant molecules, polarity of the drug, the location of the drug, pH and temperature etc. The length of the hydrophobic region of a surfactant molecule, in an aqueous environment, has an effect on the drug loading capacity of the micelle. An increase in the length helps the solubilisation of a hydrophobic drug inside the micelle core and simultaneously increasing the core size.[24]

Thermodynamically speaking, solubilisation is considered as a normal barrier of the drug between two phases (micelle and aqueous). The standard free energy of solubilisation ($\triangle\ G_s^\circ$) can be expressed by the partition coefficient (P):[24, 29]

$$\triangle\ G_s^\circ = -RTln(P) \tag{1.1}$$

Where R are the universal gas constant and T the absolute temperature. From equation 1.1 it can be determined that the free energy decreases as a result of the drug entering the micelle phase, as long as the drug is hydrophobic.[29]

The loading capacity of polymeric micelles, expressed by P, can be influenced by different factors, such as the compatibility between the hydrophobic region and the drug, the molecular characteristics and solution temperature. However the most important factor regarding the solubilisation capacity of polymeric micelles is the compatibility between the drug and the hydrophobic region, based on many individual studies. Therefore is the choice of the hydrophobic

region crucial that determines loading capacity and stability of the micelles. The compatibility can be assessed by a Flory-Huggins interaction parameter (χ_{sp}), which is defined as:[30]

$$\chi_{sp} = (\delta_s - \delta_p)^2 \cdot \frac{V_s}{kT} \tag{1.2}$$

δ_s and δ_p are Scatchard-Hildebrand solubility parameters, where the index "s" and "p" respectively represents the solubilised drug and polymer (hydrophobic region). V_s is the molecular volume of the solubilized, k is the Boltzmann constant and T is the temperature in Kelvin. The lower the χ_{sp} parameter, the greater the compatibility degree.[24, 30]

In 2004 Liu et al. [31] demonstrated that by considering the physical and chemical properties of a drug of interest (Ellipticine), a suitable polymer could be found trough comparison and calculations of the partial solubility parameters "s" and "p". These are then used to find the compatibility degree between the drug and polymer and improve formulation development in the future.[31] The compatibility degree also has an influence on the release rate of the drug from micelles. In the situation where the drug becomes more compatible with the hydrophobic region, a decrease in release rate can be expected.[24, 30]

Loading of a therapeutic agent into micelles implements stability, long circulation, better bioavailability and accurate loading conditions. However the drugs physical and chemical properties, like the hydrophobic/hydrophilic balance in the drug, can contribute to either a slow or fast release. The drug can be too stable in the micelle core, because of its partition coefficient (P) is too high.[24]

1.2.2 Polymeric micelles

Polymeric micelles represent a separate class of micelles and are formed by polymers containing both hydrophilic and hydrophobic parts, so-called copolymers.[32, 33] Copolymers contain two or more different monomeric groups organized in a polymeric chain, contrary to homo-polymers that are built of identical monomeric units.[24, 34] Copolymers can be divided according to their different arrangements, as seen in table 1.2.

TABLE 1.2: *The main structural arrangements of copolymers. The A and B stand for different monomers. Inspired by Whitehurst [35].*

Type	Description	Representation of copolymer
Homo-polymer	Identical monomers organized in a polymeric chain. Does not form micelles.	
Alternating Copolymer	Two different monomers that alternate in a regular fashion along the polymeric chain.	
Random Copolymer	The monomers are randomly distributed in the polymer chain	
Block copolymer	The monomers are blocked in long sequences. The number of blocks in a block copolymer may be different.	di-block  tri-block 
Graft copolymer	Branched copolymer with a backbone of one type of monomer and side-chains of another monomer.	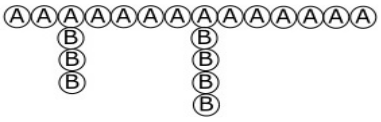

A and B refer to two different monomeric units, where A can refer to a hydrophilic unit and B a hydrophobic unit. Since copolymers are built from different monomeric units, their properties can be different along the length of the chain. The block copolymer is a linear polymer with long uninterrupted sequences of the monomeric units in its chain and can therefore have a various ranges of blocks in its molecule. Since there is a distribution of A and B sequence, as well as their length can they be written as: A_xB_y (di-block), $A_xB_yA_x$ (tri-block), $A_xB_yA_xB_y$ (tetra-block), which can be shortened to: $(A_xB_y)_n$ (multi-block). x, y and n represent average values.[27, 34]

It have repeatedly been proven that amphiphilic block AB-type copolymers with a hydrophilic block sequence, exceeding to some extent that of the hydrophobic block, form spherical micelles in aqueous solution. If the hydrophilic sequence becomes too large compared to the hydrophobic, micelles will not be formed and the copolymers will exist as unimers in water.[24] Micelles typically have a core-shell structure (see figure 1.4), that have a size distribution of 10-200 nm in diameter, depending on fabrication.[33, 36] Their small size makes them capable of extravasation through the leaky vasculature of tumour tissues and long-circulation, as mentioned in section 1.2. An advantage of polymeric micelles is their high structural stability, when compared to surfactant micelles, which can be contribute to the entanglement of hydrophobic polymer chains in the inner core. Additionally are the micelles core stabilized by the corona of hydrophilic polymeric chains.[24] The stability has two aspects, static and dynamic; the static is defined by the CMC, which is very low compared to surfactant micelles and the dynamic aspect is defined by the low dissociation rate of micelles.[24, 32, 33]

1.3 Mechanisms of endocytosis

Studying the influence of nanoparticles on the interactions during endocytosis is especially important for developing effective and safe nanoparticle drug delivery systems. Some knowledge has been derived from studies, with radiolabelled or fluorescent nano-materials like quantum dots, copolymers, liposomes etc. The studies focus primarily on the transport and effect of nano-materials throughout the body, by looking at their endocytic pathways or their impact on a narrow amount of cellular organelles. Very little has been done on combining the physical and chemical properties of the engineered nanoparticles with the cellular response. The same can be said for research into the properties of nano-materials that determine subcellular targeting.[37]

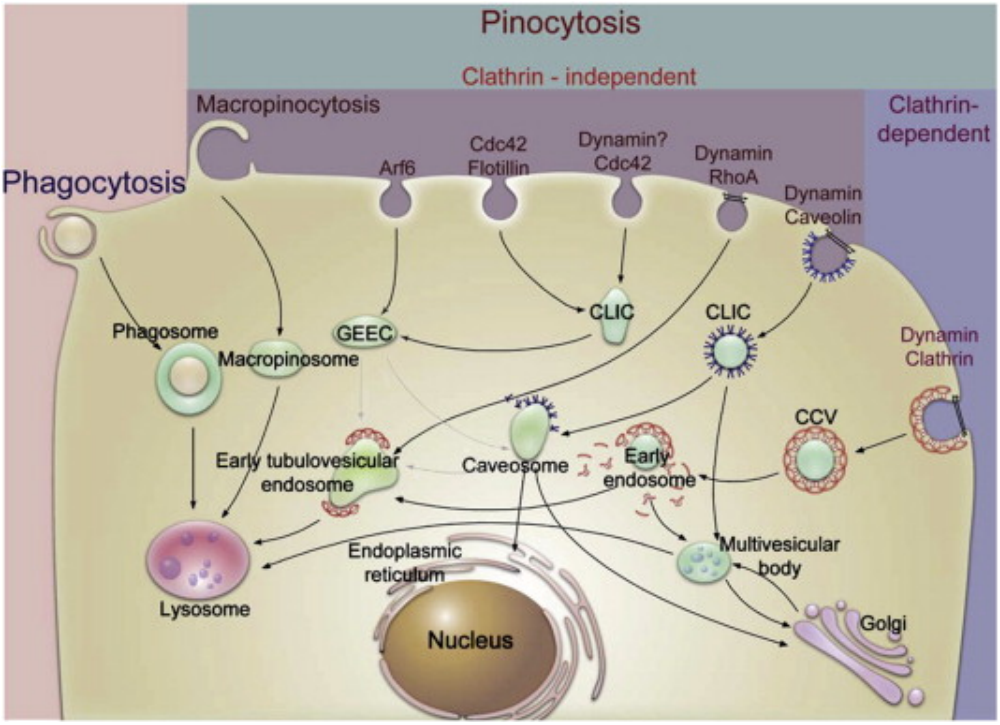

FIGURE 1.6: *Representation of the different mechanisms of endocytosis. There are a wide spread of pathways for particle or solvent uptake. In all cases, the initial stage proceeds from the membrane, involving engulfment of particle or other material into cellular vesicles. Afterwards the uptake is sorted through endosomes, where the uptake is transported to its final destination, to be recycled or transported across the cell. CCV: Clathrin-coated vesicles. CLIC: Clathrin-independent carriers. GEEC: Glycophosphatidylinositol-anchored protein. Taken from Sahaya et al. [38].*

The endocytosis process for nano-carriers, represent the active transport of nano-carriers, such as large molecules, particles and micelles into living cells. There are different types of endocytosis mechanisms; the main types are phagocytosis and pinocytosis.[39, 40] Phagocytosis is mainly associated with phagocytes (protecting cells), but other cells like fibroblast cells may also possess the phagocytic ability. The phagocytosis mechanisms can be divided in three steps: 1) Opsonisation of the nano-carriers in the bloodstream, where they are marked so that they can be targeted by phagocytes. 2) Recognition of the now opsonized nano-carrier by the phagocytic cells (receptors). 3) Internalization, where the nano-carriers are engulfed and the formation of a phagosome; a vesicle forms around the nano-carrier, where its size is dependent on the size of the carriers. The opsonisation step of the phagocytosis is the cause of the nano-carrier systems short time in the blood circulation, because they are easily opsonized. However nano-carrier systems with a hydrophilic surface are less opsonized, making the carriers less inclined for recognition,

which leads to longer circulation time.[41] The pinocytosis process includes the formations of caveolae and clathrin, as well as caveolae/clathrin-independent uptake, which depend on specific compounds and mechanics. The pinocytosis is referred to as cellular drinking, because it ingests soluble material from the surrounding environment by enclosing it in small uniform vesicles. Unlike phagocytosis, pinocytosis is a constitutive process that occurs continuously, whereas phagocytosis has to be triggered.[40, 41]

When exposing a biological system like cells, proteins or DNA to nano-materials, a series of nanomaterial/biological (nano-bio) interfaces materialize. The interfaces depend on dynamic bio-physiochemical interactions, kinetics and thermodynamic transactions between the two surfaces. It is not possible to describe all the interactions at the nano-bio interface with certainty, but the assembled knowledge provides a theoretical framework to describe some.[37]

1.3.1 Interface boundaries and forces

At the formation of the nano-bio interface, there exists a plethora of dynamic components. Three of these are: 1) the nanoparticle surface, which includes shape, size and curvature characteristics, determined by the physical and chemical composition of the nanoparticle; 2) The solid-liquid interface, starting when the nanoparticles interacts with the surrounding medium; and 3) The solid-liquid interface contact zone with biological substrates. The contact of the nanoparticles with charged or hydrophobic regions of the cell regulates the preferred pathway for interaction with the cellular environment, and the route of internalization and metabolism.[37, 42]

Each component has an influence on the interface between the nano-materials and the biological system. Some of the most important properties of the nanoparticle surface, that have an influence on the interface, include the chemical architecture of the materials, functionalization, porosity, crystallinity and hydrophobicity. Other properties like zeta potential, aggregation and biodegradability are determined by the suspending medium, together with the pH, temperature and existence of other organic molecules. These characteristic properties contribute in determining the forces that occurs at the nanoparticle/medium interface (solid-liquid interface), which demonstrate some of the principles seen between colloidal particles; van der Waals forces (VDW), electrostatic interaction (repulsive) or short range interactions from the charge and solvent interaction.[37] For example, if the particle material was SiO_2, then it is known from colloid science that typical interactions between SiO_2 particles include attractive VDW forces and repulsive electrostatic forces, the sum of which yields the Derjaguin-Landau-Verwey-Overbeek (DLVO) theory, if the particles are dissolved in water. When it comes

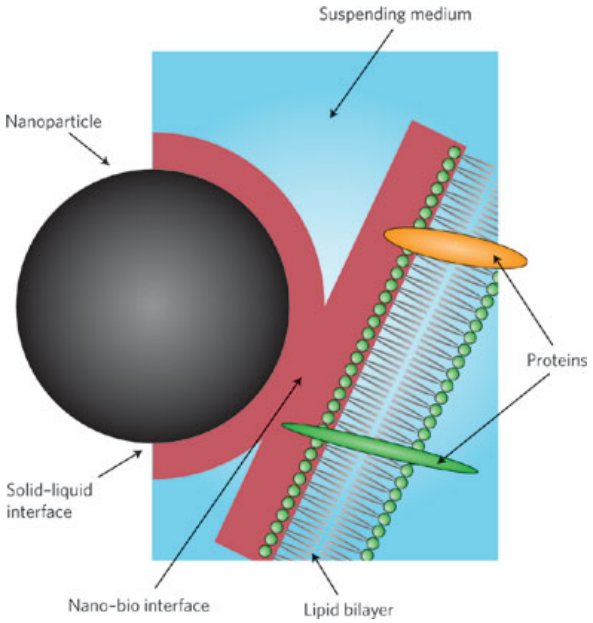

Figure 1.7: *Schematics of the interface between a nanoparticle and a lipid bilayer. The following element of the nano-bio interface are shown: 1) the nanoparticle surface (black sphere) 2) the solid-liquid interface, with the surrounding medium (red sphere) and nanoparticle interaction 3) The solid-liquid interface contact zone, which are shown as the nano-bio interface. Taken from Nell et al. [37].*

to biological fluids, the ionic strength often becomes higher around 150 mM, which indicates that the electrostatic forces are more likely to be observed only a few nano-meters from the surface. Furthermore, the high ionic strength covers the zero-frequency contribution from the VDW forces. The solvating force is also of importance, especially for inorganic and hydrophilic nanoparticles, by increasing stability through "hydration pressure" or "hydrophilic repulsion". Alternatively the surrounding fluid will dry out (dehydration) and aggregation will arise, caused by interaction at the surfaces hydrophobic attraction or hydrophobic effect.[37]

In understanding the nano-bio interface, the most challenging task is to characterise the solid-liquid interface at the contact zone. From a theoretical point of view, this interface is often assumed to have steady-state behaviour, due to the bulk properties of suspensions, such as net charge and average aggregation size. However, when considering the nano-bio interface, this approach must be adjusted. For instance, looking at a nanoparticle interacting with a fibroblast cell, the forces are similar to the interaction between two nanoparticles. An important difference however is the cell membrane. Fibroblast has a flexible membrane, which can change its shape elasticity under the influence of temperature or shear stress. Furthermore, a dynamic biological system contributes with an inhomogeneous environment, as a result of distribution and specific structural localization of proteins and lipids on the membrane surface. This result in a non-uniform distribution of charges, indicating that the nanoparticles may be exposed to different forces.[37] The continuous changes come from environmental influences, together with cellular housekeeping, e.g. a medium's properties can be changed by secreted cell products. There are many different interactions that may influence the biological system, which can change the characterising of the solid-liquid interface at the contact zone, and thereby the nano-bio interface. The size of a nanoparticle also has an influence on the interaction, as cells have a heterogeneous surface on the length scale of 10 - 50 nm in diameter, due to the presence of the surface proteins together with other structures. Thus, a micro-particle would experience a balanced energy level covering the surface, whereas a nanoparticle (10 - 50 nm) might not experience any change or interactions, depending on its specific location. With the possibility for endocytosis, the complications for the interactions accumulate and become very difficult to predict theoretically.[37] It will take time to investigate all the different interaction and explore theses interfaces in the same amount of detail as in colloidal chemistry.[37]

1.3.2 Protein corona

When nanoparticles are suspended in a biological fluid, they are instantly coated with proteins. The absorbed proteins can undergo conformational changes that can lead to exposure of altered functions and/or avidity effects. The protein corona is an important factor in the following surface properties of nanoparticles: charge, hydrodynamic size of the particle and the resistance to aggregation. The concurrent exchange of free proteins in the medium, together with the kinetics of protein association and disassociation, are important when determining the nanoparticle interactions with the cell surfaces and their receptors. [37]

The nano-material surface composition determines which biomolecules interact with the surface and thereby influence the particle interactions with the cell. Different proteins are known to form complexes with nanoparticles, the nature of which is affected by the dissociation-dissociation rates, respective binding interactions between specific particle types and the biological medium. Furthermore, the concentration of proteins surrounding the particle have an influence on the binding of the proteins, and the creation of the corona. Albumin, immunoglobulin and fibrinogen are proteins that bind strongly to polymeric micelles, carbon

nanotubes and liposomes. Immunoglobulin is a common antigen in the human body, which protects and leads to opsonisation of pathogens or particles, hence promoting phagocytosis [43].[37, 44]

1.3.3 Particle wrapping of a surface membrane

The nano-bio interface principles can be observed with particle adhesion to a cellular surface, which results in the wrapping of the cells membrane. The wrapping of the membrane at the adhesion sites depends upon specific and non-specific interactions to overcome the elastic forces of the membrane, opposing particle uptake. The "wrapping time" or the time for cellular uptake can be determined mathematically from different factors such as size, shape, energy of the system and elasticity of the cell membrane. Some factors have been mentioned in section 1.2, like that the optimal size for a spherical particle is between 10-50 nm. Surface ligand provide an effective means for binding interaction, thereby allowing the particle to interact with molecules or receptors on the cell membrane. Furthermore, a protein corona also effects the wrapping efficiency depending on its nature, thermodynamics and receptor diffusion.[37]

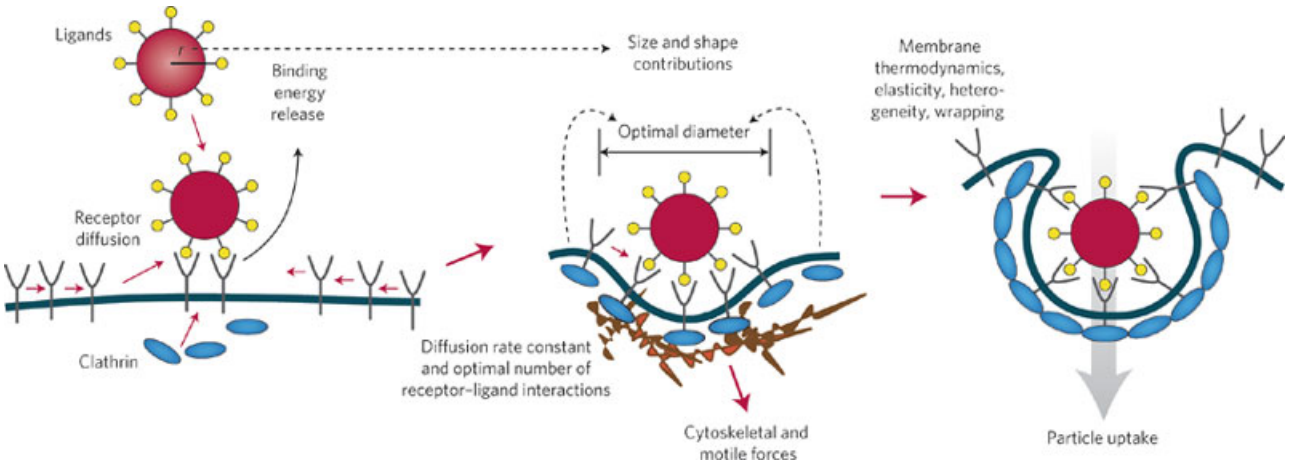

Figure 1.8: *For particle uptake to be established, some specific or non-specific binding interaction have to occur. Shown above is the specific binding interaction (Ligands - receptor), that is driven by a decrease in free energy at the adhesion sites to overcome the elastic forces. The particles coated with specific ligands that react with the respective receptors. The red circles represent nanoparticle, with ligands attached to their surface, shown as the yellow dots. The ligands interact with the Y-shaped receptors. The blue ellipses denote the protein clathrin, which is engaged in the energy-dependent uptake of particles. Taken from Nell et al. [37].*

These interactions conclude in a pinocytosis process called receptor-mediated or clathrin-mediated endocytosis, a process that is associated with drug delivery. In order to accomplish this process, the receptors must be present at the adhesion site by diffusion, for the formation of a number of critical interactions. Receptor diffusion establishes a resistive force with an optimal rate constant to attain wrapping. The number of receptors that diffuse to the membrane therefore influence the wrapping process, since a limited number of receptors could restrain particle wrapping. It is not necessary that the ligands are of biological origin; they can be constructed of chemical functional groups, metallic sites, polymer or surface function modification that promotes binding affinity. One criteria is that they potentially result in endocytosis or direct penetration of the membrane. Direct penetration is observed for Au nanoparticles with amphipathic compounds arranged on their surface, allowing them to slip through the cell membrane without causing damage[45].[37]

1.4 Curcumin

Curcumin is derived from the rhizome of the spice *Curcuma longa*. Curcumin has a wide spread of biological and pharmacological abilities; it is anti-inflammatory, an anti-oxidant, can be used to combat tumours among others.[46] Curcumin is a yellow/orange crystalline powder, with the chemical structure $C_{21}H_{20}O_6$ and is a bis-α,β-unsaturated β-diketone, which is commonly named diferuloylmethane. [47, 48] This indicates that curcumin exhibits keto-enol tautomerism with a predominated keto form in neutral and acid solutions and a stable enol in a basic medium. Commercially available curcumin is a mixture of three natural curcumin analogues from the *Curcuma longa* spice; diferuloylmethane, demethoxycurcumin, and bisdemethoxycurcumin, which represents, respectively approximately 77%, 17% and 6% of the mixture. [48, 49]

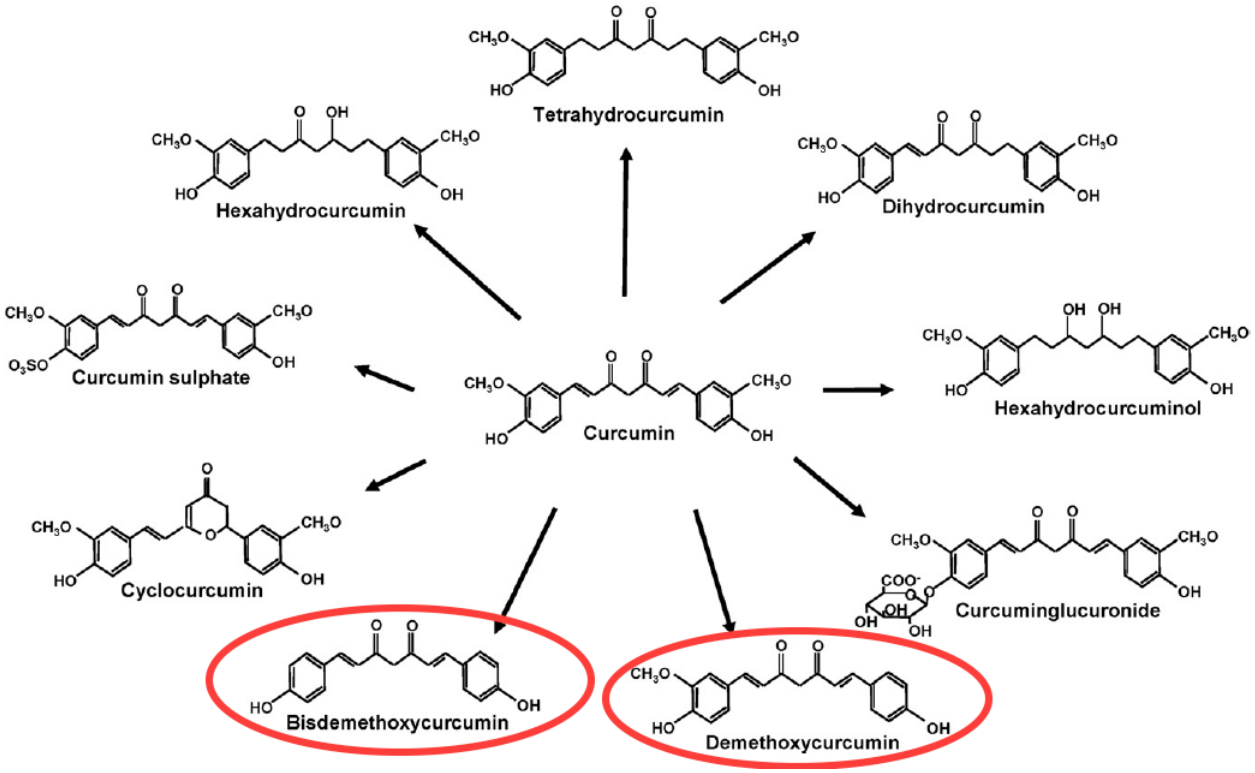

FIGURE 1.9: *The chemical structure represents curcumin and its natural analogues from its origin spice Curcuma longa, in addition to its important metabolites. The red circles indicate the curcumin analogues applied in the commercially available curcumin mixture. Taken from Anand et. al [49].*

Curcumin is soluble in acetone, ethanol and dimethyl sulfoxide (DMSO) and insoluble in water and ether. It has a melting point of 183 $°C$ and a molecular weight of 368.37 g/mol. Curcumins colour appearances are dependent on the pH value of the aqueous environment; at the pH level of 2.5 - 7, curcumin will appear yellow while for pH $>$ 7 it will appear red. In aqueous solutions the stability of curcumin is enhanced for high pH values, but it is only soluble at a low pH value. [50, 51] This is contrary to organic solutions, where curcumin is both stable and soluble at acidic ph. At unstable conditions defined as aqueous medium at neutral pH or higher, it degrades to ferulic acid and feruloylmethane. In a phosphate buffer system with a pH of 7.2, $>$90% of curcumin will rapidly degrade over a period of 30 min; antioxidants can prohibit this degradation, indicating that the degradation is caused by an oxidative mechanism. Degradation is extraordinary slow at pH values between 1 - 6, which are the conditions experienced in

the stomachs environment. In cell culture mediums with 10% foetal bovine serum (FBS) and human blood, curcumin is more stable; after 1 h <20% curcumin will start to degrade and at 8 h approximately 50% will have degraded. Fluorescence of curcumin can be observed as a broad band at different wavelengths, depending on the suspending solvent; in acetonitrile at λ_{max}= 524 nm, in ethanol at λ_{max}= 549 nm and in micellar solutions at λ_{max}= 557 nm. Some structures can be seen in toluene at λ_{max}= 460 - 488 nm.[50, 51]

In the last couple of decades, great effort have gone into isolating curcuminoids, a collective expression for curcumin analogues from other sources, including *Curcuma longa*, *Curcuma zedoaria* and *Curcuma aromatica*. *Curcuma zedoaria* and *Curcuma aromatica* are in close relation to *Curcuma longa* , and several groups have investigated and compared their biological and pharmacological activities.[49]

1.4.1 History

Throughout human history, plants have been used for various purposes and have evolved alongside all life. These plant-based products are millions of years old. Thousands of these products have originated as secondary metabolites, to protect the plants from their environment, diseases and infections. One of the many applications of the plants is as medicine, where they have had an important impact on health care in many ancient and modern cultures. In India a system of holistic medicine known as Ayurveda[1] use many plant-based drugs to treat different diseases, including cancer. The modern medicine have not encouraged or held nature based medicine in high account With a better understanding of the molecular mechanisms of some nature-based medicine products, the therapeutic abilities of plants can be fully understood. [50]

Curcuma longa also called Turmeric, is an Indian spice belonging to the ginger family, which contains the active component curcumin, has been thoroughly investigated for its therapeutic use. The curcuminoids represents 3-5% of this spice [50]. Turmeric has a long history as a medicinal plant and has remained holy from time immemorial. In India this spice has many names; golden spice, spice of life and the earthy herb of the sun and in ancients times it was considered a holy spice the one herb above all others. Turmeric can be documented for its medical use for at least 6000 years in India.[47]

Turmeric is primarily cultivated in India, but is native to the south-east Asia, where related *Curcuma* plants grow in the wild, which it itself is not known to do. Other countries, like China, Indonesia and Thailand also cultivated Turmeric, but Indian Turmeric is considered the best on the world market, making India the world's largest producer, consumer and exporter. In a year (2002-2003) there was produced around 636000 tons of turmeric plants from an area of 175190 ha; this is 20.6% of the production of spices in India from 5.5% of the growth area. The production of Turmeric have increased annually by 7.6% in the past 30 years.[47]

1.4.2 Medical properties of curcumin

Curcumin is mostly known as a dietary spice or colouring agent in food and textile, but is additionally used as treatment for a wide variety of ailments. Investigations concluded over the past four decades have provided indications of how many and which ailments curcumin have an influence on. It has been found to reduce blood cholesterol, repress symptoms of type II

[1] An alternative medicine used in Hinduism, where the person is considered on a physical, psychological, social, and spiritual plane to prevent disease.

diabetes, and speed up wound healing among other things. Some of the medical properties of curcumin can be seen in figure 1.10.[40]

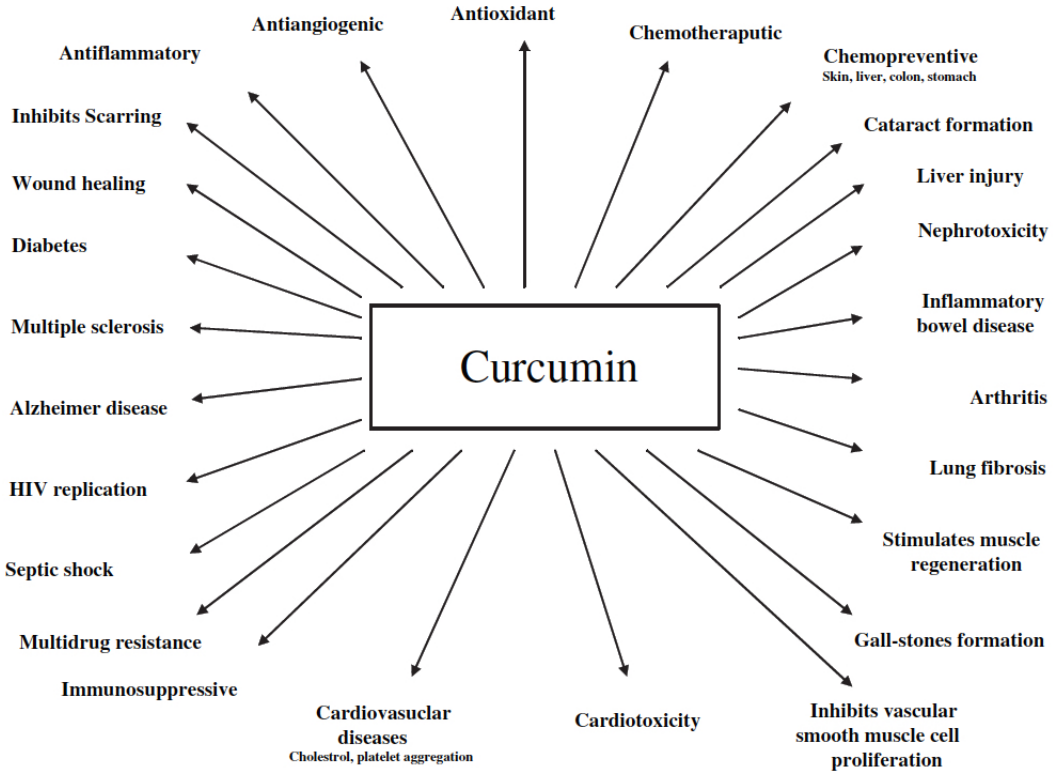

FIGURE 1.10: *A representation of the medical properties of curcumin. Reproduced from Alberts et. al [40].*

From all these studies, it is shown that curcumin affects a large number of targets, including growth factors, receptors, enzymes and gene regulating apoptosis. This multi-targeting ability might explain its therapeutic potential against cancer. Extensive studies have shown that due to the complexity and multiple signalling pathways including cancer evolution and growth, drugs that have an ability to target several different mechanisms, are more effective towards cancer, compared to the monotargeted anticancer drug currently in use.[52]

Curcumin has been shown to be effective against different variations of cancers, including leukaemia along with breast-, lung- and brain cancer. Regarding various malignant glioblastoma cells - a class of brain tumour cells resistant towards chemotherapy and radiation - it has been observed that curcumin inhibits the NF-κB signalling pathways in all the cell lines. Furthermore, curcumin affects a variety of other mechanisms, including the induction of non-apoptotic autophagy cell death, the inhibition of G6PT gene expression and the activation of both receptor-mediated and mitochondria-mediated proteolytic pathways etc.[52] In the study by Aoki et al. [53], the authors have shown that curcumin induces apoptosis of malignant glioma cells through naturally regulated destructive mechanisms both in *vitro* and in *vivo*. In the study, U87-MG cells were inoculated in an adult nude mouse and grown to a tumour of a volume of 50 - 70 mm^3. Afterwards intratumoral injections of curcumin every 24 h for 7 days were administered. The curcumins effect was evaluated on day 16 of the initial treatment. The experiment resulted in a threefold decrease in the tumour volume, compared to the control.[52, 53]

1.4.3 Curcumin loaded micelles

Although curcumin has great therapeutic potential and numerous applications to combat disease, its further development in clinical applications is hindered by its poor solubility, poor oral bioavailability and its fast degradation in the body.[54, 55] In order to fully exploit the potential of curcumin, an injectable drug formulation with controlled release properties, as well as protection from hydrolytic degradation, is needed for clinical applications.[46, 54, 55] In the study performed by Yang et al. [46], they produced curcumin encapsulated polymeric micelles by a single-step solid dispersion method, and investigated the curcumin micelles cytotoxicity in *vitro*, along with their size, stability, cellular uptake and their anti-tumour activity. The curcumin micelles had a size of 27.6 nm in diameter, and were found to be relatively stable for 48 hours after preparation. The cytotoxicity investigation has shown that curcumin micelles and free curcumin efficiently suppresses the growth of colon carcinoma cells, while blank micelles showed only a minor cytotoxicity as a drug carrier. The cellular uptake has been investigated using fluorescence microscopy and flow cytometry, where the cells incubated with curcumin micelles exhibited a larger amount of apoptotic bodies, when compared to cells with free curcumin. The study concludes that curcumin loaded micelles inhibited the growth of colon cancer, by enhancing the cellular uptake of curcumin and increasing apoptosis induction.[46]

In an another study performed by Liu et al. [55], they produced curcumin loaded polymeric micelles with a small particle size and high drug loading, through a one-step solid dispersion method, and investigated their characteristics as a potential water-based formulation of curcumin, along with the cytotoxicity the in *vitro* release behaviour and their anti-tumour activity. The curcumin micelles had a size of 28.2 nm and had archived a relatively high encapsulation efficiency of 98.91 %; additionally these curcumin micelles were stable and soluble in aqueous solutions. The release behaviour of curcumin micelles and free curcumin was investigated through a dialysis method, which revealed a fast release of free curcumin. Curcumin micelles however had a much slower and suitable release rate, indicating its applications as a drug delivery system by minimizing the curcumin exposure to healthy cells. The cytotoxicity investigation has shown that free curcumin and curcumin micelles efficiently inhibit growth of 4T1 cells, while blank micelles indicated a very low cytotoxicity. The curcumin micelles showed a higher cytotoxicity activity than free curcumin, suggesting that the micelles enhance the cytotoxicity of curcumin. The anti-tumour effects of free curcumin, curcumin micelles and blank micelles showed that blank micelles exhibited no anti-tumour effect, when compared to free curcumin and curcumin micelles, that both suppress the growth of tumours. The study concluded that curcumin micelles are an attractive water-based formulation of curcumin, with its effective and enhanced anti-tumour activity.[55]

1.5 Cell viability

Cell viability is often mentioned in the context of cryopreservation, but is not commonly defined in articles, so its exact meaning is often obscure. This is undesirable, since it can lead to a wrong interpretation of results.[56] Often cell viability is defined as the amount of healthy cells or damaged cells in a sample. Measuring cell viability is important for cell culturing as well as to cytotoxicity assays. Typically toxicity assays are run continuously over a period of time to investigate cell proliferation for a given initial population. There are a many different cell viability methods, which can be loosely characterised by the assays used to analyse the population and the individual cells. The assays that analyse the population are the most rapid, but provide less detailed information compared to the individual analysis.[57]

Over time viability assays have become more complex and more optimization oriented. Trypan blue dye exclusion assays are widely used assays today, but it was also one of the earliest methods and was based on a basic principle: Healthy viable cells have an intact membrane, while dead cells have a damaged membrane, indicating that the intact membrane can exclude the trypan blue dye, where the damaged membrane has lost control of its pathways into the cell, leaving it to appear blue. The methods is characterised as an individual cell assay, so the cells can be counted by the use of a microscope or an automated counting device. These counts can then be used to find the percent of viable cells in the sample. However, this method does have some disadvantages; it has been indicated that the number of dead cells increase upon adding the dye, thereby requiring the cells to be counted quickly [58]. [57]

With time new dyes, which rely on the metabolic activity of the cells, have become more popular, since they can used on adherent cells and thereby lead to high-throughput analysis. New technology has also resulted in providing major advantages, in the form of measurements. By using a plate reader, multiple treatment groups can be screened in a short time period. For optimization of viability assays, multiple method exist for investigations into the mechanisms of cell death; examples include the Resazurin-based methods and live/dead staining and the influence of dyes on the cells. In conclusion, the optimal viability assay varies depending on the cell type and culture conditions, and as such than one method should be used to confirm the individual assays.[57]

The cytotoxicity assay used in this thesis is a method of estimating the number of non-viable cells present in a multiwell-plate. The assay measures the release of lactate dehydrogenase (LDH) from cells with a damaged membrane. The LDH released from the cells to the growth medium are measured by a 10 min coupled enzymatic assay, thereby measuring the enzymatic activity of NADH dehydrogenase. NADH's activity results in the conversion of resazurin into resorufin. Resofurin is a fluorescent, which is being generated in proportion to the amount of LDH. This reagent mix does not harm healthy cells, making it possible to measure LDH release directly in the assay wells containing a mixture of non-viable and viable cells.[59]

1.5.1 Glioblastoma

Glioblastoma are also called grade IV astrocytoma, and are a part of a group of tumours which arise from glial cells or supporting tissue in the brain, called glioma. Astrocytoma is one type of glioma, named after the star-shaped cells (astrocytes) from which they grow. [60]

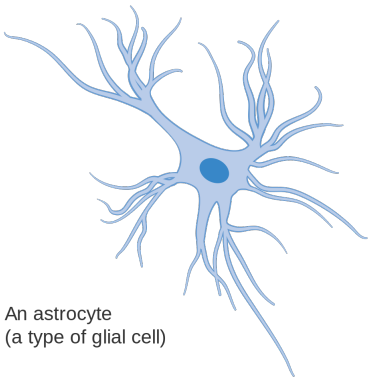

Figure 1.11: *A diagram of astrocyte cells. Taken from Cancer Research Uk. [61].*

The degree of astrocytoma abnormality is described with grades, on a scale of I to IV. Glioma tumours with a grade of I are considered benign, whereas grade II are also considered benign, but require frequent monitoring by MRI or CT scan every 6 - 12 months. Malignant glioma and high-grade glioma are terms for grades III and IV, where grade III has an increased growth index compared with grade I and II. Tumours are also grouped by their growth rate: slow growth (low grade), moderate (mid-grade) and rapid (high-grade), where grade III astrocytomas are considered to have mid-grade growth rate. [60]

Glioblastoma is the highest grade of glioma and is the most common and fatal primary brain tumour in humans. The National Institutes of Health (NIH) has found it to have the highest incidence rate among inter cranial malignity in the last 40 years. Glioblastoma develops rapidly from its onset and exhibits no clearly recognizable morphological changes in the cells before it reaches grade III. In elderly patients (over 55 years), it is characterized by a rapid growth rate and short survival time. Younger patients (under 45 years) in some cases exhibit epilepsy due to low-grade gliomas, which in time progress to a secondary glioblastoma. The occurrence of secondary glioblastoma are seen in ∼5% of the patients, and can only be diagnosed trough historical evidence of the tumours evolution or clinical observations. [60, 63, 64]

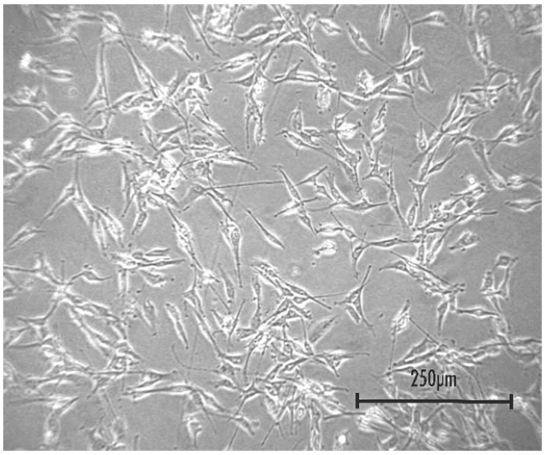

Figure 1.12: *An light micrograph of the cell line U87 glioma in DMEM + 10% of FBS. Taken from de Almeida Sassi et al. [62].*

For newly diagnosed patients, the standard treatment would be a surgical procedure for total removal of the tumour and, if possible, chemotherapy and radiation therapy to remove any remnants. The overall survival is 15 months, though 2 - 5% of patients may survive 3 years or more. The variation in survival rate is closely related to the patients performance status, which is defined from the individual patients. A young age is advantageous. Treatment options are limited and the survival rate has not changed much over the years, when compared to other cancer types. A cure has not been found for glioblastoma, but trough research and clinical

trials, the understanding of the disease progression has been found: molecular alterations in signalling pathways and small improvements in patient responses to treatment, is a step in the right detection. [60, 63, 64]

1.5.2 Fibroblast

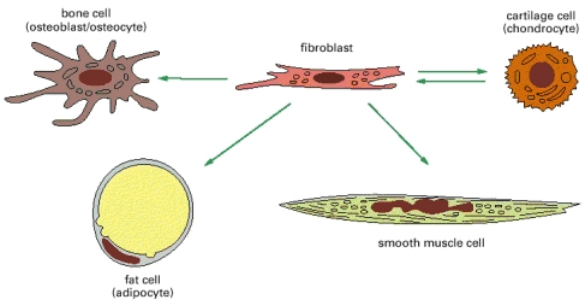

FIGURE 1.13: *The connective-tissue cell family. The arrows indicate the interconversions within the family. Fibroblast is shown as single cell. Taken from Alberts et al. [65]*

Fibroblast is a part of a bigger group of cells, the family of connective-tissue cells. The connective-tissue cells are any variation of cells found in the connective-tissue, such as fibroblast cells, fat cells, bone cells, cartilage cells and smooth muscle cells. The connective-tissue is the structural framework of the body, where it accompanies and supports all other tissue. The connective-tissue itself is formed by fibroblasts spread out by the collagenous extracellular matrix (ECM), which is a complex network of polysaccharides and fibrous proteins secreted by cells. These networks are only secreted by the fibroblast, bone and cartilage cells. Fibroblast cells are a central part of the ECM structure; it produces the structural proteins, adhesive proteins and amorphous gel-like substances that make up the cell. Additionally they play other roles beyond structural their purposes. It is responsible for the ECM's maintenance and reabsorption, inflammation, angiogenesis, cancer progression and wound healing. When an injury occurs on the skin or in tissue, the fibroblast cells closest by start multiplying and migrating into the wound and create countless of collagenous matrices. These will isolate and reconstruct the damaged skin or tissue.[65, 66]

The family of connective-tissue cells is a fundamental part of the support and reparation of tissues and organs, and their ability to redefine or rebuild themselves depending on the circumstances is of great importance. This allows the cells to undergo change and respond to many types of damage. This ability to advance in the face of changes and their confined lifestyle, is a good explanation as to why the cells are easy to grow in a culture. [65]

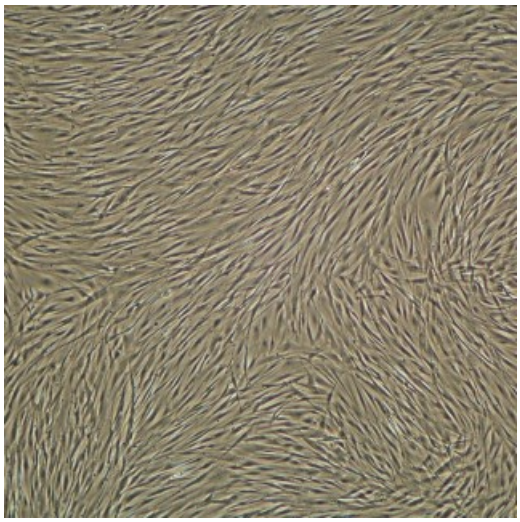

FIGURE 1.14: *An light micrograph of confluent primary human fibroblast cells grown in CnT-05 medium. Taken from CellnTec [67]*

The fibroblasts display the ability to transform into other family members, but despite this there are there some uncertainties about this interconversion. Evidence indicates that fibroblast cells are essentially different in various areas in the body, and may be different for each region in the body. The maturity of the fibroblast cell has an influence on their transformation ability. A mature fibroblast cell is

less capable of transforming, and exists alongside immature fibroblast cells, which can develop into an assortment of mature cells. [65]

2. Material and Methods

2.1 Material

TABLE 2.1: *An overview of all chemicals, equipment and software used in this project. All solutions were prepared with mili-Q water produced at the laboratory using a Silhorko water treatment plant.*

Name	Manufacturer	Description
0.22μm Sterile Filter	Jet Biofil	PES membrane, 250 mL
4 well chambered slides	Thermo Fischer Scientific	Borosilicate
Cellstar Multiwell culture plate	Sigma Aldrich	96 well, F-bottom, with lid
Culture flask	Thermo Fisher Scientfic	T25, T75, T125
Round-bottom polystyrene tubes	Thermo Fisher Scientific	5 mL
(3-Aminopropyl) trimethoxysilane (APTMS)	Sigma Aldrich	$>$ 97%
Acetone	Sigma Aldrich	$>$ 99.5%
Chloroform	Sigma Aldrich	$\geq$99.9%
Curcumin	Sigma Aldrich	Powder, stored at -20°C, from Curcuma longa (Turmeric)
CytoTox-ONE	Promega	CytoTox-ONE Assay kit
DMEM (1x)	Gibco, Thermo Fisher Scientific	Glutamax
Dynasore hydrate	Sigma Aldrich	Blocks dynamin-dependent endocytosis, stored at -20°C, protected from light
Ethanol (EtOH)	Kemetyl	96%
Ethylenediaminetetraacetic acid (EDTA)	Bie & Berntsen	0.02% in PBS, stored at -20°C
Fibroblast (CRL 2429), Homo sapiens, from skin tissue		Courtesy of the stem cell group at Aalborg University
Foetal Bovine Serum(FBS)	Invitrogen/VWR	Stored at -20°C
Formaldehyde	Sigma Aldrich	Formalin solution
Glioblasstoma (U87), Homo Spaiens, from brain tissue		Courtesy of the stem cell group at Aalborg University
Hoechst 33342	Invitrogen	A nucleic acid stain, emits blue fluorescence
Horse Serum	Invitrogen/Fisher Scientific	Stored at -20°C
Pernicillin/Streptomycin (P/S)	Invitrogen/VWR	Stored at -20°C

Continues on next page

Table 2.2: *An overview of all chemicals and equipment used in this project. All solutions were prepared with mili-Q water produced at the laboratory using a Silhorko water treatment plant.*

Phosphate-buffered saline(PBS) X10	Thermo Fisher Scientific	pH 7.4, without calcium and magnesium
Polyvinylpyrrolidone(PVP)		Countesy of Prof. M. Shtilman " Biomaterials" center, Mendeleyev University. [68]
Sodium azide	Merck Millipore	Very toxic, stored at room temperature
Toluene	Sigma Aldrich	≥99.5%, ACS reagent
Tryple	Thermo Fisher Scientific	Replacement for trypsin, gentle towards cells, stored at room temperature
Trypsin (T)	Invitrogen/VWR	Stored at -20°C
Wortmannin	Sigma Aldrich	Penicillium funiculosum, ≥98%, (PI3-K) inhibitor
Equipment	**Manufacturer**	**Description**
NanoSight LM10	Malvern	Sample chamber, microscope and camera
NanoSight NTA 2.1	Malvern	Software
Steri-Cycle CO_2 incubator	Thermo	Temperature at 37°C and 5% CO_2
PixeLink Digital camera	PixeLink	For light micrograph
PixeLink Capture OEM	PixeLink	Program
Olympus CKX41	Olympus	Microscope
Axio Observer.Z1	Carl Zeiss	Inverted fluorescent microscope
AxioCam MRm	Carl Zeiss	Digital Camera
Zen 2012	Carl Zeiss	Software
Vibra Cell	Sonics	Sonication Probe
Ultrasound Bath	VWR	Branson Ultrasonics 2510
Centrifuge	Eppendorf	5804R
CHRIST Alpha 1-4 LD plus freeze dryer	Sciquip Ltd.	
Multimode Atomic Force Microscope (AFM)	Bruker	Tapping mode
WSxM	WSxM solutions	Software for AFM images
Multimode Plate reader	Perkin Elmer	EnSpire
CytoFlEX S Flow cytometer	Beckman Coulter	4 Laser(30mW, 638nm 50mW and 405nm 80mW) 13 Fluorescent Detectors
CytoExpert	Beckman Coulter	Software
Matlab	MathWorks	Software

2.2 Methods

The chemical structure of the PVP polymer used throughout this project, can be observed in figure 2.1. The polymer is available with different unit mass at 1 and 6 kDa.

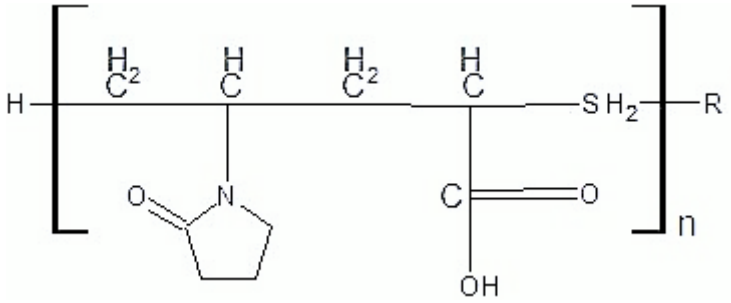

FIGURE 2.1: *The chemical structure of the polymer used throughout this project: PVP-COOH, where* $R{=}C_{18}H_{37}$.

2.2.1 Synthesis of loaded micelles

In this project micelles with different loaded hydrophobic materials, such as curcumin and chloroform, was explored. The micelles formed with chloroform are considered empty micelles. The approach for synthesis of the different micelles differs, depending on the solvents applied.

2.2.1.1 Micelles loaded with curcumin

50 mg of PVP polymer was dissolved in 8 mL milli-Q water, while 5 mg curcumin (Sigma Aldrich) was dissolved in 1 mL acetone (Sigma Aldrich) simultaneously. The two solutions were then mixed in a Greiner centrifugation tube and sonicated using a sonication probe (Sonics) for 10 minutes (pulse, 1 s on, 2 s off, Amplitude 40%) The Greiner tube was stored in ice to prevent overheating. After the sonication, the solution was frozen in liquid nitrogen and lyophilised in the vacuum freeze dryer (Sciquip Ltd.). The dehydrated powder is then stored at room temperature, wrapped in aluminium foil to protect it from light.

2.2.1.2 Empty micelles

50 mg of PVP polymer was dissolved in 8 mL milli-Q water. 1 mL chloroform (Sigma Aldrich) was added to the polymer solution and then sonicated in a sonication probe (Sonics) for 10 minutes. (Pulse 1 s on, 2 s off, Amplitude 40%) The Greiner tube was placed in ice to prevent overheating. The sonicated solution was frozen in liquid nitrogen and lyophilised in the vacuum freeze dryer (Sciquip Ltd.). The dehydrated powder is then stored at room temperature.

2.2.2 Nanoparticle tracking analysis

Size distribution was determined using Nanoparticle Tracking Analysis, through their properties of light scattering and Brownian motions in a liquid suspension. Suspended micelles were injected into the sample chamber, where a laser beam was passed through, scattering the light, and making the micelles easily visible in the microscope. The NanoSight microscope (Malvern) was equipped with a video camera, that records a video file of the Brownian motions of the micelles. The Nanoparticle Tracking Analysis (NTA) software (Malvern) used the video to track individual micelles, and used different equations to determine their diameter.[69]

2.2.2.1 Preparation of untreated sample

The intended amount of lyophilised micelles was weighed and dissolved in the equivalent amount of mili-Q water in order to reach a concentration of 1 mg/mL. The suspended micelles was sonicated in an ultrasound bath (VWR) for 60 min and centrifuged (Eppendorf) for 10 min at 10000 rpm, 21°C. A 1 mL luer syringe was used to transfer the prepared micelle solution to the NanoSight (Malvern) sample chamber. Through the microscope a position, where a significant amount of moving micelles (ca. 10 or more) can be observed, was found by adjusting focus and moving the sample. Then a 160 sec video file of the micelles was record with the NTA software (Malvern). Parameters were adjusted (detection threshold, blur and screen grain), so each observed micelle was marked with one cross and the processing was started. The obtained data are then processed in MatLab (MathWorks).

2.2.2.2 Preparation of ultrasonically dispersed samples

The lyophilised micelles was weighed and dissolved in the milli-Q water, to create a 1 mg/mL solution. A 1 mL luer syringe is used to transfer the prepared micelle solution to the NanoSight (Malvern) sample chamber. Through the microscope a position, where a significant amount (ca. 10 or more) of moving micelles can be observed, was found, by adjusting focus and moving the sample. Then a 160 sec video file of the micelles were record with the NTA software (Malvern). Parameters were adjusted (detection threshold, blur and screen gain), so each observed micelle was marked with one cross and the processing was started. The obtained data are then processed in MatLab (MathWorks).

2.2.3 AFM imaging

The AFM imaging was performed using a Bruker Multimode AFM Nanoscope IIIa in tapping mode. The tapping mode is especially well adapted to soft samples, because of its complete reduction of the lateral force on the sample [70]. An Olympus 24OTS silicon-based cantilever, with a resonance frequency of 68 kHz and a force constant of 1.43 - 2.47 N/m, was used for imaging of the polymeric micelles. Alternatively, a Scan Sens HA-NC silicon-based cantilever with a resonance frequency 140 kHz and a force constant of 3.5 N/m was used. An either freshly cleaved or chemically modified mica surface were used as a substrate for depositing micelles.[71]

2.2.3.1 Sample preparation for AFM observations

Two preparation methods were applied for the AFM observation; drop deposition directly on the mica surface (negatively charged surface) and drop deposition on an APTMS modified mica surface (positively charged surface).

Freshly cleaved mica surface A solution of 1 mg/mL lyophilised micelles in milli-Q water was prepared. The suspended micelles was sonicated in an ultrasound bath (VWR) for 60 min and centrifuged (Eppendorf) for 10 min at 10000 rpm, 21°C. 10 μL of prepared micelle solution was deposited on the freshly cleaved mica surface by pipetting. The sample are left for 10 minutes, and then dried by blowing on the sample with N_2.

APTMS modified mica surface The freshly cleaved mica surface was incubated in a vacuum chamber with a mixture of 250 μL APTMS (Sigma Aldrich) and 500 μL toluene (Sigma Aldrich) for 30 min. Simultaneously the micelle solution is prepared. Prior to the modification, the chamber was flushed and filled with argon to eliminate water vapour. The 1 mg/mL lyophilised

micelles in milli-Q water solution was then prepared and sonicated in an ultrasound bath (VWR) for 60 min , followed by centrifuging (Eppendorf) for 10 min at 10000 rpm, 21°C. 20 - 30 μL of prepared micelles solution was then deposited on the APTMS modified surface through pipetting. The sample was left for 5 - 10 minutes and then dried with N_2.

2.2.4 Cell culturing

In this project two cell lines have been used for experiment: Glioblastoma (U87) and Fibroblast (CRL 2429). All the experiments were performed in a sterile environment (Fume hood), there have been cleaned with 70% EtOH (Kemetryl). The following protocols are identical for both cell lines.

2.2.4.1 Preparation of DMEM 10% FBS 1% P/S growth medium

1 mL of P/S solution (VWR) and 10 mL of FBS solution (VWR) were added to 500 mL DMEM growth medium (Gibco). The medium was then filtered through a 0.22 μm sterile filter (Jet Biofil) by vacuum pump, in to a sterile container. The DMEM 10% FBS 1% P/S growth medium are stored at 4°C.

2.2.4.2 Preparation of 2 % Horse Serum DMEM 1% P/S growth medium

1 mL P/S solution (VWR) and 2 mL Horse Serum (Invitrogen) were added to 100 mL DMEM growth medium (Gibco). The solution was then filtered through a 0.22 μm sterile filter (Jet Biofil) by vacuum pump into a sterile container. The 2% Horse Serum DMEM 1% P/S growth medium are stored at 4°C.

2.2.4.3 Preparation of T/E solution

T/E solution was prepared by first diluting trypsin (VWR) 1:10 in PBS, and then filter it through a 0.22 μm filter (Jet Biofil) by vacuum pump. Then EDTA (Bie & Berntsen) was dissolved to 0.002% solution and filtered through a 0.22 μm filter as well. The two solutions were mixed 1:1, resulting in a 0.125% /0.01% T/E solution.

2.2.4.4 Preparation of PBS solution

PBS 10x solution (Thermo Fisher) was diluted 1:10, with mili-Q water and filtered through a 0.22 μm filter by vacuum pump, into a sterile container. The PBS solution are stored at room temperature.

2.2.4.5 Starting cell culture

A cell culture was started by preparing 14 mL DMEM 10% FBS 1% P/S growth medium. The medium was transferred to a T75 cell culture flask and incubated at 37°C for approximately 20 minutes. A 1 mL vial containing approximately 1 million cells suspended in DMSO was thawed, and immediately after transferred to the headed growth medium. The cells and medium were mixed by pipetting. The cells are incubated overnight at 37°C and the growth medium was then changed. Subsequently the growth medium was change every two or three days, until the cells have reached 80 - 100% confluent.

2.2.4.6 Passing or splitting cells

For splitting and passing the cells when they have reached 80 - 100% confluent, the growth are removed from the T75 cell culture flask. The cells were washed with filtered PBS and trypsinated by adding 1.5 mL of T/E to cover the bottom of the culture flask. The amount of T/E solution required depends on the size of the culture flask. The cells are incubated at 37°C for 5 - 10 min, until the cells are lifted from the surface. 5 mL of growth medium was added to the culture flask to stop the trypsination, which is toxic to the cells if they are exposed to it for too long. The desired amount (1/5 or 1/10) of cell solution was transferred to a centrifuge tube and centrifuged (Eppendorf) for 5 minutes at 1000 rpm, 21°C. The growth medium was removed from the centrifuged tube and 5 mL of fresh growth medium was added. The cells and the medium were mixed by pipetting. The re-suspended cells were transferred to a new T75 cell culture flask, which has been prepared with 10 mL heated medium; if needed, they can alternatively be prepared for counting. For counting the cells, 10 μL of the re-suspended cells were transported to a counting chamber where they can be counted, and cell solutions with specific cell concentration can be obtained. The T75 cell culture flask was incubated at 37 °C. The growth medium has to be changed every two or three days, until the cells have reached 80 - 100% confluent.

2.2.4.7 Transfer of cells to multiwell-plates

For transferring cells to multiwell-plates (Sigma Aldrich), the cells was first prepared by passing, as described in section 2.2.4.6. Instead of transferring the cell solution to a culture flask, they were counted to obtain a desired cell concentration. 50% of the multiwell-plate well volume was filed with growth medium. The cell solution obtained from the passing was diluted to a suitable volume and cell concentration, for the required amount and size of wells. 50% well volume of the diluted cell solution was added to each well. The multiwell-plate were incubated at 37 °C and grow until the cells was suitable for experimentation. The growth medium has to be changed every two or three days.

2.2.5 Cytotoxicity assay

The CytoTox-ONE^{TM} Homogeneous Membrane Integrity Assay kit (Promega) was used to estimate the % of damaged cells in a multiwell-plate. The specific method used can be seen in section 1.5.

Reagent preparation

1. Thaw and equilibrate Substrate Mix and Assay Buffer to room temperature (22 °C).
2. The CytoTox-ONE Reagent was prepared by adding 11 mL Assay Buffer to a vial of Substrate Mix.
3. Gently mixed to dissolve the substrate mix.

Protocol

- Set up a multiwell-plate (Sigma Aldrich) containing cells in growth medium (Cell seeding concentration depends on plate size).
- Incubate the multiwell-plate until the cells have reached 80% confluence.

  - Each well was photographed for documentation of confluence and amount of cells.
  - Discard the growth medium.
  - Wash once with PBS (Thermo Fisher).

- Add the micelle solutions, which have been dissolved in 2% *Horse Serum supplemented medium* (see method 2.2.4.2), to the appropriate wells.
- After 24 hours of incubation at 37°C were the multiwell-plate removed and equilibrated to 22°C (approximately 20 - 30 minutes).
  - Each well was photographed again.
  - To generate a positive control, the maximum LDH release has to be detected; for this a lysis solution was used. Add 2 μL of lysis solution per 100 μL original volume, to the positive wells. Incubate for 5 min at 37°C. Before the multiwell-plate was equilibrated to 22°C.
- Transfer 100 μL of medium to a grey multiwell-plate.
- Add 100 μL of CytoTox-ONE Reagent to each well and mix or shake for 30 sec.
- Incubate at 22 °C for 10 minutes, making sure that the sample is not exposed to light.
- Add 50 μL of Stop solution to each well, in the same order of addition that was used for adding the CytoTox-ONE Reagent.
- Shake plate for 10 seconds.
- The fluorescence was record with an excitation wavelength of 560 nm and an emission wavelength of 590 nm in the multi-plate reader (Perkin Elmer).

2.2.6 Fluorescence microscopy of drug uptake in *vitro*

The following preparations were carried out in 4 well borosilicate chambered slides (Thermo Fischer), with a total volume of 1 mL. The chamber slide was later examined in the fluorescence microscope (Carl Zeiss), where they were exposed to different filter channels. The channels depend on the dye or fluorophore used to stain the cells: DAPI have an excitation wavelength at 353 nm and emission wavelength at 465 nm, which were channelled through a 335 - 383 nm excitation filter and a 420 - 470 nm emission filter. FITC have an excitation wavelength at 495 nm and emission wavelength at 519 nm, which were channelled through a 450 - 490 nm excitation filter and a 500 - 550 nm emission filter. DsRed have an excitation wavelength at 545 nm and emission wavelength at 572 nm, which were channelled through a 538 - 562 nm excitation filter and a 570 - 640 nm emission filter. The DAPI was used to channel out Hoechst dye, which is a blue fluorescent that stains the nucleus of eukaryotic cells. The FITC and DsRed channels out fluorescence of curcumin.

Solution preparation

- Dynasore hydrate (Sigma Aldrich): 50 μL per. 4 mL growth medium.
- Worthmaninn (Sigma Aldrich): 0.43 μL per. 4 mL growth medium.
- Hoechst Dye (Invitrogen): Dilute 1:1000 in PBS (Thermo Fischer).

Exposing cells to endocytosis inhibitors, by incubation The growth medium was removed from the cells and 50% well volume of dynasore hydrate or worthmaninn were added to the respective marked wells. The 4 well chambered slides were incubated for 30 min at 37°C.

Exposing cells to micelles and free curcumin A micelle solution was prepared by dissolving lyophilised micelles in the equivalent amount of growth medium, to reach a concentration of 1 mg/mL. The micelle solution was centrifuged (Eppendorf) for 5 min at 1000 rpm, 21°C. 50% well volume of the prepared micelle solution were added to the 4 well chambered slides, and was incubated for 30 min at 37 °C. Subsequently, the wells were washed carefully with PBS (Thermo Fischer), until the colour from curcumin was no longer seen. 100% well volume were filled with 4% formalin solution (Sigma Aldrich) and was then incubated at 37°C for 5 - 15 min. Preceding preservation, all the wells were washed twice with PBS and stored in PBS at 4°C. The wells are then ready for further experimentation.

Cells exposed to Hoechst dye To expose the cells to Hoechst dye, the wells were emptied of growth medium or PBS (Thermo Fischer) and 100% well volume of Hoechst solution was added to the wells. Subsequently the wells were incubated for 15 - 20 minutes at 37°C. All the wells were then washed twice with the solvent the cells originally were stored in; PBS or growth medium. The wells were stored in the solvent used for washing at 4°C.

2.2.7 Flow cytometric analysis

To investigate the cells endocytosis mechanism for uptake of the synthesised 6 kDa curcumin micelles (CM), flow cytometry was applied. Flow cytometry measures and analyses the various physical characteristics of the cells, as they stream through a beam of light in suspended form. Some of the characteristics measured are internal complexity, relative fluorescence intensity and the cells relative size. In this case, fluorescent intensity will be directly linked to the amount of curcumin that has been taken up by the cells. All the properties are determined by applying an optical-to-electronic coupling system, which registers how the cells scatter, when deviating incident laser light, and emit fluorescence at range of wavelengths. The setup consists of three main systems: fluidics, optics and electronics.[72]

1. The fluidics system transport the suspended cells to the laser, through a stream for examination.

2. The optics system includes lasers, which illuminate the cells in the sample stream and the optical filters, which directs the light signals to the relevant detectors.

3. The electronics system detects the light signals from the optics systems and convert it into electronic signals that can be handled by a computer.

When the light is passing through the stream, it is refracted and deflected by the cells, which produces scattered light. Any fluorescent molecules present will fluoresce and the emitted light will be collected together with the scattered light by positioned lenses. A combination of filters and beam splitters steers the collected light to the defined detectors, which produces electronic signals proportional to the optical signals. In this case, the scattered light will be collected by the forward scatter (FSC) and the side scatter (SSC) photodiodes. The combination of FSC and SSC signals can be used to evaluate the cells relative size and the internal complexity.[72]

In order to elucidate the mechanisms of endocytosis, different inhibitors capable of blocking endocytic pathways of the cells, were used in combination with 6 kDa CM. To inhibit some endocytosis mechanisms, dynasore hydrate and sodium azide were used. Dynasore hydrate inhibits dynamin GTPase activity, together with dynamin dependent endocytosis.[73] Almost all endocytosis mechanisms are dependent on energy processes; these mechanisms can be inhibited by lowering the temperature and sodium azide at the same time.[74]

A CytoFlEX S Flow cytometer from Beckman Coulter was used for the study. It is equipped with 4 lasers and 13 fluorescent detectors. To determine the presence of curcumin in the cells the channel PerCP was used, with laser excitation at 488 nm and fluorescent emission 650 - 690 nm. The number of event measured for all the samples was 20000, whit a flow rate of 30 μL/min for the CRL 2429 samples and 60 μL/min for the U87 samples. The collected data were further examined in the software CytoExpert (Beckman Coulter).

Solution preparation

- A Stock solution of 10% sodium Azide (Merck Milipore) was prepared by dissolving the sodium azide in PBS (Thermo Fischer). From the stock solution, a 0,01% solution of sodium azide dissolved in growth medium was produced.
- Dynasore hydrate (Sigma Aldrich): 50 μL per. 4 mL growth medium.

Protocol

- Cells were seeded, with a cell concentration of 40000 cells/mL in T25 culture flasks with a capacity of 6 mL. The seeding process for the culture flasks are similar to transferring to a multiwell-plate (see section 2.2.4.7).
- Incubate the T25 culture flasks at 37°C until the cells have reached 100% confluence.
- The culture flasks were emptied of growth medium and washed twice with PBS (Thermo Fischer).
- Add 3 mL of inhibitor solution dynasore or 0.01% sodium azide to the culture flasks. Culture flasks without inhibitors was incubated with 3 mL growth medium and control culture flasks (containing only cells) was incubated with 6 mL of growth medium.
- Incubate for 30 min at 37°C or 4°C, depending on the inhibitor.
    - For this experiment sodium azide was incubated at both 4 and 37 °C.
- Add 3 mL of 6 kDa CM to culture flasks with and without inhibitors and incubated for another 30 min, at their respective temperature.
- The culture flasks were emptied and washed once with PBS (Thermo Fischer).
- The cells were trypsinated by adding 3 mL of Tryple (Thermo Fischer), until the cells were lifted from the surface.
- The cells solution was then transferred to centrifuge tubes and centrifuged (Eppendorf) for 5 min at 1000 rpm.

- Empty the centrifuge tubes for tryple and re-suspended the cells in 3 mL PBS (Thermo Fischer) and transfer the cell solution to 5 mL round-bottom polystyrene tubes (Thermo Fischer).
- The cellular uptake was then measured and analysed with a CytoFLEX S Flow cytometer (Beckman Coulter) with a 448 nm laser.

3. Results and Discussion

3.1 Production of micelles

Various micelles were synthesised using two PVP polymers of different sizes (1 and 6 kDa), as well as curcumin and chloroform. Curcumin is used as a hydrophobic model drug, to give an indication of the cellular uptake of the micelles. In itself it is considered effective towards cancer and many other diseases, and its ability to act as a fluorescent dye, makes it a favourable model drug. Furthermore curcumin helps to stabilise the micelles, by creating a hydrophobic core together with the octadecane in the polymer. Chloroform helps to temporally stabilise the micelles, in order to synthesis possible empty micelles. Both curcumin and chloroform are strong hydrophobes, and are small with molecular weights of 368.37 g/mole and 119.38 g/mole respectively; that property gives them the possibility of forming small stable micelles. They will create tension in the hydrophobic region of the polymer molecules when incorporated into the core.

The procedure used to synthesise the curcumin and chloroform loaded micelles, as described in section 2.2.1, is an oil-in-water method; this means that an aqueous solution of the polymer is prepared, and a solution of curcumin in an organic solvent is added to from an oil-in-water emulsion. The encapsulation of curcumin happens when the organic solvent evaporates in the freeze dryer. Chloroform is an organic solvent, and will evaporate in the freeze dryer, theoretically leaving the micelles empty. The lyophilised micelle powder synthesised in this project is shown in the pictures in figure 3.1. These are only some of the many batches synthesised and applied in this project.

(a) (b) (c)

FIGURE 3.1: *Photographs of the different synthesised lyophilised micelle powders in greiner tubes. (a) is 1 kDa lyophilised micelle powder. (b) is 6 kDa lyophilised micelle powder and (c) is 6 kDa lyophilised empty micelle powder.*

The appearance of the lyophilised powders differs when comparing the two PVP polymer sizes. The 1 kDa lyophilised powder appears to have a more flaky texture in its powder structure and a bright yellow colour, whereas the texture of the 6 kDa lyophilised powder is smoother and uniformly structured and has a slightly darker yellow colouring. These differences in colour and

texture can be a result of the size difference, or a result of the freezing with liquid nitrogen, where parts of the solution may have adhered to the tube sites, resulting in a flaky texture.

3.1.1 Size distribution

The polymer size, together with the solvents curcumin and chloroform has been shown to have an influence of the size distribution of the various micelles. In the following graphs showing the size distributions of the various synthesised micelles have been provided. The lyophilised powder has been prepared by dissolving a given amount of it in an equivalent amount of milli-Q water, to reach a concentration of 1 mg/mL. Afterwards some solutions are treated with ultrasound treatment and analysed with the NanoSight. The two preparation methods can be seen in sections 2.2.2.1 and 2.2.2.2. The data was collected from the NTA software and processed with Matlab. During the processing, the data were limited to 0 - 400 nm, instead of 2000 nm. The data above 400 nm showed nothing specific, and was as such deemed unimportant.

3.1.1.1 Curcumin loaded micelles

The graphs observed in figure 3.2 illustrate the size distribution of a 1 kDa CM sample with and without ultrasonic treatment. The graph in panel (a) is the 1 kDa CM sample which has been treated with ultrasound treatment, as described in section 2.2.2.1. The size distribution range from 34 - 370 nm. This graph show a broad spectrum of sizes, with four peaks at 82, 112, 154 and 200 nm. The highest concentration of micelles is seen at 82 nm.

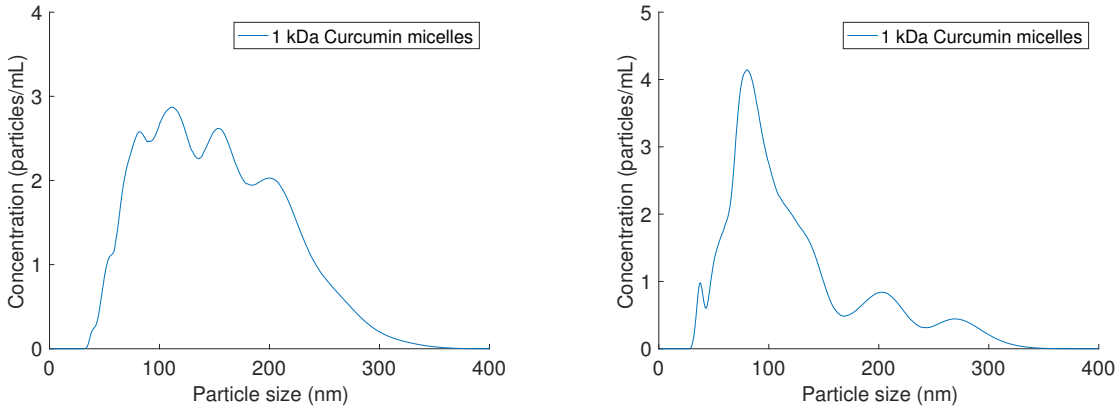

(a) (b)

Figure 3.2: *1 kDa CM synthesised using the procedure in section 2.2.1.1 to produce micelles loaded with curcumin. Panel (a) shows the size distribution graph obtained from the NanoSight analysis for the 1 kDa CM sample with ultrasound treatment (section 2.2.2.1). Panel (b) shows the size distribution graph obtained from the NanoSight analysis for the 1 kDa CM sample without ultrasound treatment (section 2.2.2.2).*

The graph in panel (b) illustrates the size distribution graph for the 1 kDa CM sample, without ultrasound treatment. The graph shows a high concentration of micelles at 80 nm and some lower peaks at 38, 202 and 271 nm respectively, with a size distribution ranging from 28 - 342 nm.

On figure 3.3 two size distribution graphs for 6 kDa CM are illustrated, with and without ultrasound treatment. The graph in panel (a) shows the 6 kDa CM solution treated with ultrasound treatment. The size distribution ranges from 25 - 400 nm, with one clear peak observed at 142 nm.

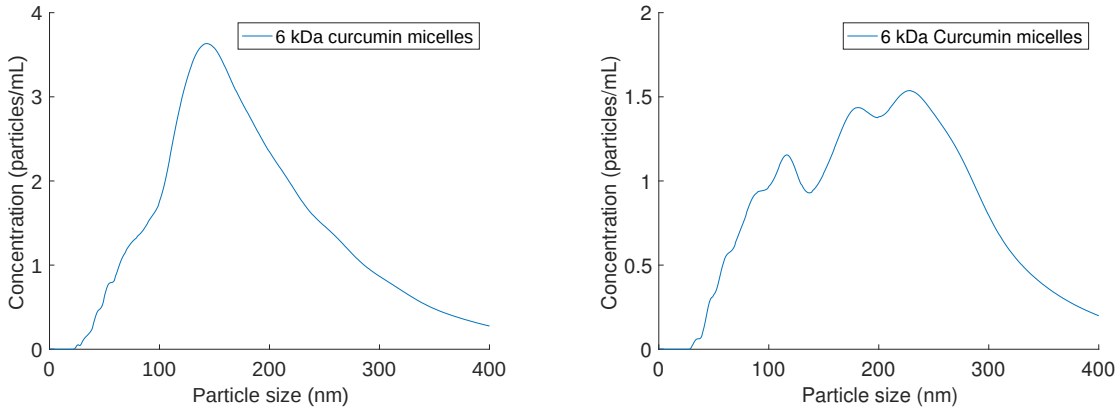

(a) (b)

FIGURE 3.3: *6 kDa CM synthesised using the procedure micelles loaded with curcumin section 2.2.1.1. Panel (a) shows the size distribution graph obtained from the NanoSight analysis for the 6 kDa CM sample with ultrasound treatment (section 2.2.2.1). Panel (b) shows the size distribution graph obtained from the NanoSight analysis for the 6 kDa CM sample without ultrasound treatment (section 2.2.2.2).*

The graph in panel (b) on figure 3.3 shows the 6 kDa CM solution without ultrasound treatment. Here is a broad size distribution ranging from 20 - 400 nm shown, with some indications of individual peaks at 116, 180 and 227 nm. The highest concentration of micelles is seen at 227 nm.

Since the micelles are stored as a lyophilised powder after being synthesised, they still contain some remnants of free polymer chains and an excess of curcumin. Theses residues can be form through by-products like micro-aggregates, which is seen in the NanoSight as broad size distribution spectra, together with badly dissolved micelles. The ultrasound treatment is therefore necessary to properly dissolve the lyophilised powder; additionally the solution is centrifuged, to force precipitation of the residues. Another possibility is to change the synthesising method to include rotary evaporation in vacuum, in order to eliminate the solvent, but re-suspending it after this can prove difficult if the lyophilised powder cannot be easily dissolved. It is inadvisable to centrifuge the micelle solution after sonication, since it contains an organic solvent; it is not safe and could result in the removal some of the curcumin from the micelle core.

When comparing the size distribution of 1 and 6 kDa CM, it becomes clear that the polymer size has an influence on the result. The 1 kDa CM has a diameter of 80 nm, while 6 kDa CM have a diameter of 142 nm. 1 kDa CM are smaller and have a narrow size distribution, and results in a higher concentration of micelles in the analysed solution. The 6 kDa CM are almost twice as big as the 1 kDa CM and their size distribution are broader. This indicates that the synthesis with 6 kDa polymer produces fewer and larger micelles, together with more free polymer chains, whereas 1 kDa polymer produces a large amount of small micelles, with free polymer chains. However during the experiments it was observed that 1 kDa CM was more difficult to dissolve than 6 kDa CM, which can be a result of the flaky powder texture of 1 kDa CM. Nonetheless when comparing the graphs for 1 kDa CM in figure 3.2, it can be seen that the sample that was treated with ultrasound and centrifuged, is the sample with the broadest size distribution and gives the most imprecise indication of the micelles size. This is in contrast to the sample without ultrasound treatment, which has a narrow size distribution and a clear particle size at 80 nm. This may possibly indicate that the flaky structures in the 1 kDa CM texture are PVP polymer

residues and a small excess of curcumin, there have not produced micelles, which where dissolve by the ultrasound treatment. 1 and 6 kDa CM have been synthesis with the same proportions of PVP polymer and curcumin, which may not have been ideal. From the size distribution, it is seen that a 6 kDa CM solution contains large and few micelles, while a 1 kDa CM solution contains small and numerous micelle along with polymer residue. This might imply that 1 kDa polymer require a more curcumin, when synthesising 1 kDa CM. Thereby producing a 1 kDa CM solution containing a higher amount of small micelles and less polymer residue.

In studies by Yang et al. [46] and Liu et al. [55], the synthesised micelles are much smaller, as compared to the ones synthesised in this project. The molecule mass of the polymer in these article are not presented, making it problematic to fully compare them to our results. In addition a different method of synthesizing the micelles is applied, which also can have an influence on the different observed results.

3.1.1.2 Empty micelles

On figure 3.4 two size distribution graphs for empty micelles are shown, with and without ultrasound treatment. The graph in panel (a) illustrates the ultrasound treated empty micelle solution. It is seen that the size distributions are very broad, ranging from around 10 nm to above 400 nm. The highest concentration of micelles is seen at 40 nm in diameter. Other individual peaks are seen at 27, 61, 111, 139, 246 and 365 nm. The concentration of these micelles is not as high as observed at 40 nm. On the graph in panel (b), the empty micelles solution treated

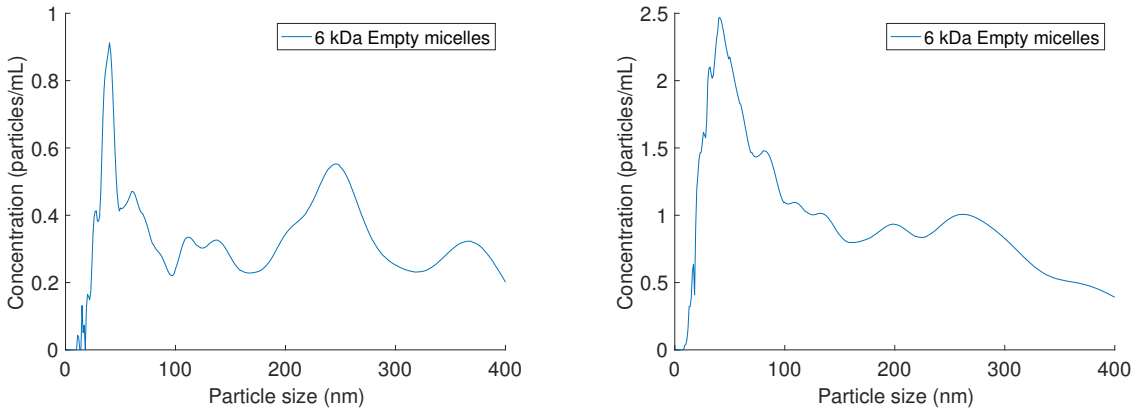

Figure 3.4: *Empty micelles synthesised using the procedure from section 2.2.1.2 to produce micelles loaded with chloroform. Panel (a) shows the size distribution graph obtained from the NanoSight analysis for the empty micelle sample with ultrasound treatment (section 2.2.2.1). Panel (b) shows the size distribution graph obtained from the NanoSight analysis for the empty micelles sample without ultrasound treatment (section 2.2.2.2).*

without ultrasound treatment is seen. The graph shows a high concentration of micelles at 41 nm, as well as a broad size distribution from 10 - 400 nm. There are indications of other peaks along the distribution around 31, 82, 110, 135, 199 and 263 nm, with lower concentration of micelles than at 41 nm.

The very broad size distribution graphs seen in figure 3.4 for both empty micelles solutions indicate, that there is a high concentration of PVP polymer residues in the solutions. The empty micelle solution treated with ultrasound treatment is smother, and gives a small clear peak at 40 nm, where a large concentration of undissolved micelles and residues have been

removed from the solution. It still shows a broad size distribution, which can be a result of aggregated micelles or polymer chains still residing in the solution. However, when comparing the empty micelles size with those of 1 and 6 kDa CM, they are very small and very few in the solution, which can be a result of the high concentration of polymer aggregates and residues. The empty micelles have a size of 40 nm, which is twice the size of 1 kDa CM and almost four times the size of 6 kDa CM. The empty micelles small size, high concentration of polymer aggregates and residues, can be directly linked to the use of chloroform. Chloroform helps to temperately stabilize the hydrophobic core, but evaporates when lyophilised, which resulted in less stable empty micelles. Where the curcumin loaded micelles still remains stable after lyophilised, because of the curcumin in their core. The stability of the empty micelles is not very high, which can result in the concentration of monomers become lower when dissolving the micelles for experimentation. The are no hydrophobic interactions to hold the monomers in place in the micelles, making them loss and leaves a high concentration of monomers in the micelle solution. This can be observed in the NanoSight results, panel (a) and (b) figure 3.4 both shows broad size distribution, there are, as mentioned, a resulted of polymer chains and aggregates residing in the solutions.

All the small individual peaks seen in some of the size distribution graphs such as in figure 3.2 and panel (b) in figure 3.3 can be the results of large micelles or aggregates being over represented in the NTA software. The large micelles or aggregates migrate slowly across the screen, because of their large size, which makes them over represented in the NTA softwares statistics. Some micelles might not have been marked in the NTA software resulting in incomplete statistics.

3.1.2 AFM imaging of micelles

The synthesised micelles were observed with a Bruker Multimode AFM Nanoscope IIIa operating in tapping mode on mica. In the following figures the obtained images and height profiles from cross-sections of the various synthesised micelles are shown. The lyophilised powder was weighed and dissolved in an equivalent amount of milli-Q water, to reach a concentration of 1 mg/mL. Afterwards the solutions were treated with ultrasound and drop deposited on either APTMS modified mica or freshly cleaved mica. The two methods are described in section 2.2.3.1. The images where processed in the WSxM software.

3.1.2.1 Empty micelles

Figure 3.5 shows two AFM images of synthesised empty micelles, that have been treated with ultrasound before being drop deposited on an APTMS modified mica substrate or a freshly cleaved mica substrate, as well as two height profiles. Panel (a) in figure 3.5 shows the APTMS modified mica substrate and two small deposited micelles. The blue line across the micelles represents their cross-sections. The cross-section profiles from panel (a) can be seen on panel (b). The profiles show structures with heights ranging from 5 - 7 nm and 60 nm across.

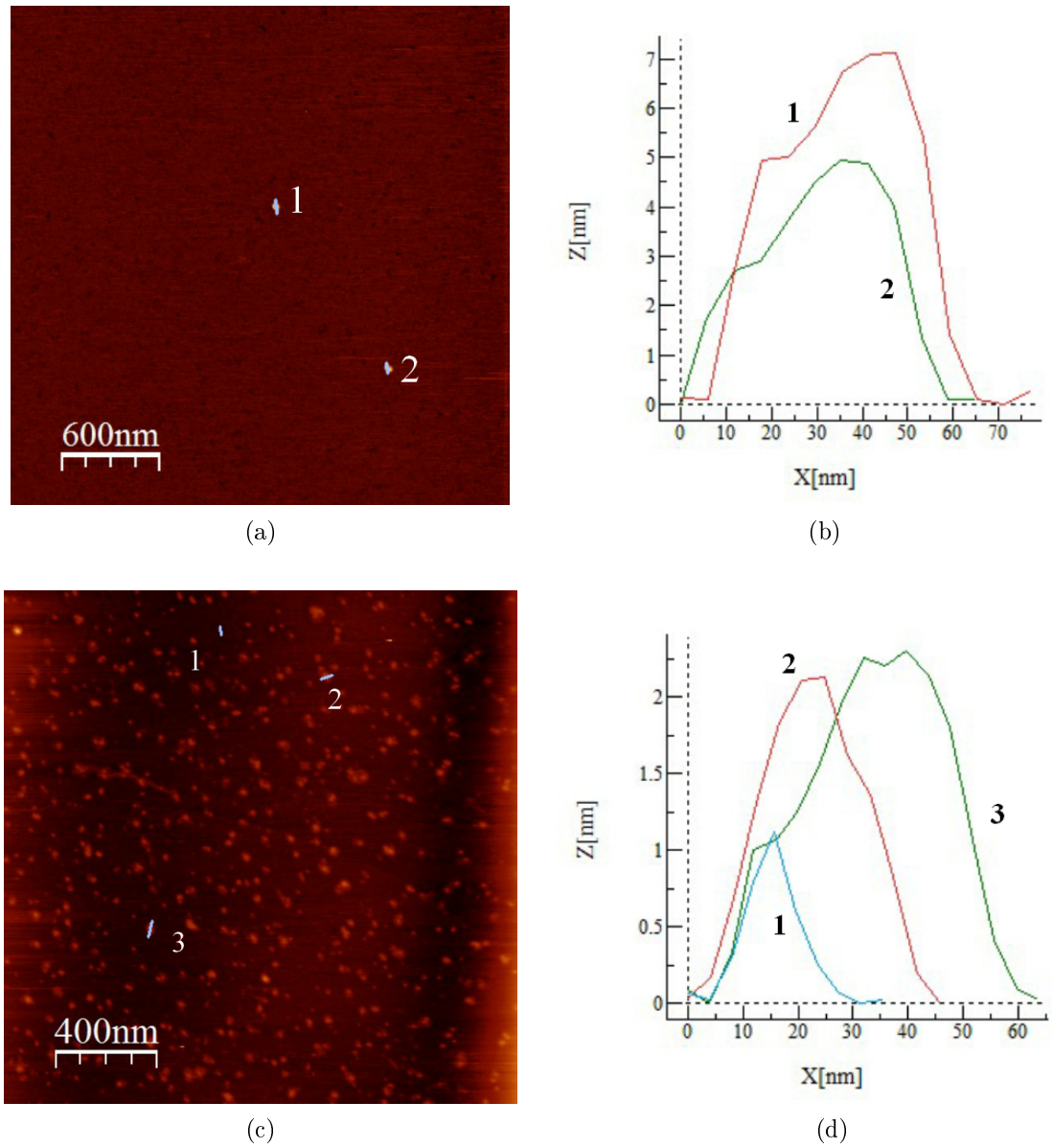

Figure 3.5: *AFM images of empty micelles, produced by loading micelles with chloroform as described in section 2.2.1.2, and their height analysis. Numbers decide the respective cross-sections. Panel (a) and (c) represents AFM images of empty micelles treated with ultrasound treatment and drop deposited on a APTMS modified mica substrate or a freshly cleaved mica substrate, see section 2.2.3.1. Panel (b) and (d) represents the cross-section profiles of the blue lines in panel (a) and (c).*

Panel (c) shows the freshly cleaved mica substrate and the deposited micelles. The deposition pattern is random across the mica substrate and some of the presumed micelles look to be aggregates of multiple micelles, with a variety of sizes. The blue lines represent cross-sections of some of the randomly deposited micelles. The graph in panel (d) shows the cross-section profiles, which illustrates the structures height and width. The three cross-sections show a height ranges from 1 - 2.5 nm and a width length of 25, 40 and 55 nm.

When comparing the two AFM images in figure 3.5 panel (a) and (c), there is an obvious difference in concentration of deposited micelles between the two. On the APTMS modified mica substrate only two empty micelles are seen, whereas on the freshly cleaved mica substrate large amount of presumably empty micelles are observed. This gives an indication of the empty

micelles surface charge, since the APTMS modified mica is positively charged and the freshly cleaved mica is negatively charged, it results in positively charged empty micelles. The height profiles also implies that the micelles seen in panel (a) of figure 3.5 are less collapsed than the micelles observed in panel (c), where there is a height difference around 2 - 3 nm. The height profile in panel (b) appears more uneven across its structure, where two peaks can be seen, which may result in a broader width. It can also be a result of a collapsed core, but the graph does not show a significant decrease in the curve, which would be expected for a collapsed core. The height profiles in panel (d) shows a more well defined and broad peak for its cross-sections, resulting in a more reliable presentation of the micelle width. The micelles on the negatively charged surface (panel (c)) are more collapsed on the surface, resulting in broad widths and a small height profiles.

Comparing the empty micelles size obtained from the NanoSight to those obtained with the cross-section profiles, a difference is seen. One of the cross-sections profiles in panel (d) in figure 3.5 shows a width of 40 nm, which corresponds to the size seen in panel (a) in figure 3.4. However, when the micelles are deposited on the mica surfaces, they collapse on the oppositely charged surface, due to the interaction forces, between the positively charged micelles and the negatively charged mica surface. This results in broader micelles than observed in the size distribution analysis.

3.1.2.2 Curcumin loaded micelles

Figure 3.6 shows two AFM images of synthesised 1 kDa CM, that have been treated with ultrasound before being drop deposited on a APTMS modified mica substrate or a freshly cleaved mica substrate, as well as two height profiles. Panel (a) in figure 3.6 shows the AFM image of the freshly cleaved mica substrate and the deposited 1 kDa CM. The blue lines represent cross-sections, which correspond to profiles seen in the graph in panel (b). A large variety of randomly distributed micelles across the mica substrate are observed on panel (a), where some looks collapsed and others appears to be deposited on top of each another. The profiles show structures with heights ranging from 1 - 3.5 nm and very broad widths of 100, 225, 425 and 625 nm.

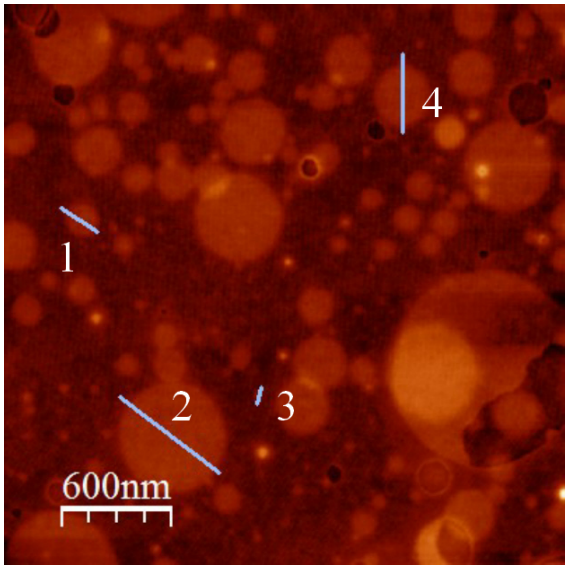

(a)

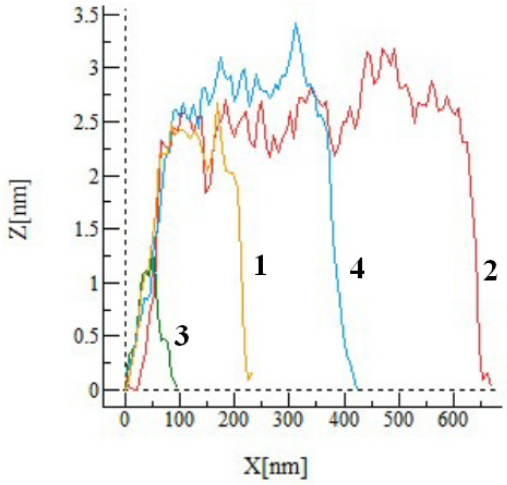

(b)

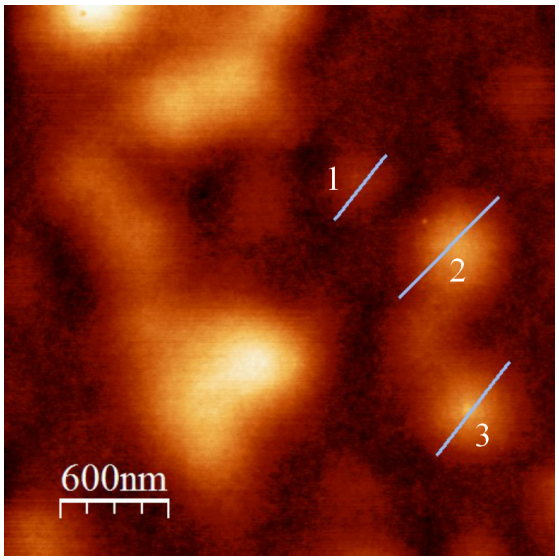

(c)

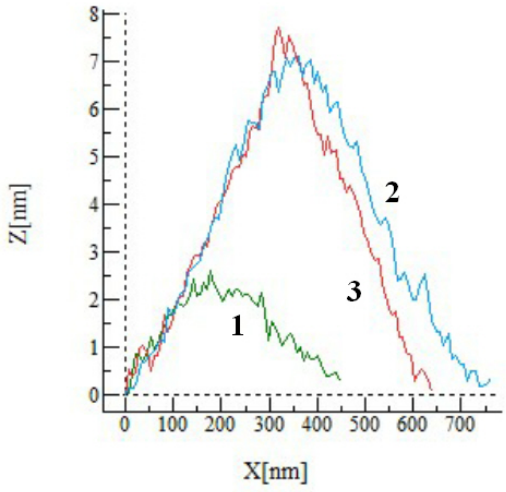

(d)

Figure 3.6: *AFM images of 1 kDa CM produced by loading micelles with curcumin as described in section 2.2.1.1 and their height analysis. Numbers decide the respective cross-sections. Panels (a) and (c) represents AFM images of 1 kDa CM treated with ultrasound treatment and drop deposited on a freshly cleaved mica substrate or a APTMS modified mica substrate respectively (see section 2.2.3.1). Panels (b) and (d) represent the cross-section profiles of the blue lines in panel (a) and (c).*

Panel (c) shows the AFM image of 1 kDa CM deposited on APTMS modified mica substrate, where the blue lines represent cross-sections. The cross-section profiles, seen in graph in panel (d) shows the structures heights, which range from 2.5 - 8 nm and a width of 450, 650 and 750 nm.

Figure 3.7 represents two AFM images of synthesised 6 kDa CM, that have been treated with ultrasound before being drop deposited on a APTMS modified mica substrate or a freshly cleaved mica substrate, as well as two height profiles. Panel (a) shows the AFM image of 6 kDa CM deposited on freshly cleaved mica substrate, with blue lines representing cross-sections. On the AFM image only three micelles are observed, which have a random distribution pattern. In contrast to the AFM image in panel (c), the scale for this image is smaller, which results in

smaller micelles in comparisons. The cross-section profiles can be seen in the graph in panel (b), showing the height and width of the structures. A height range from 1 - 6 nm is shown together with a width of 15, 95 and 120 nm. Some substrate irregularities from 0.5 - 1 nm can be observed as well.

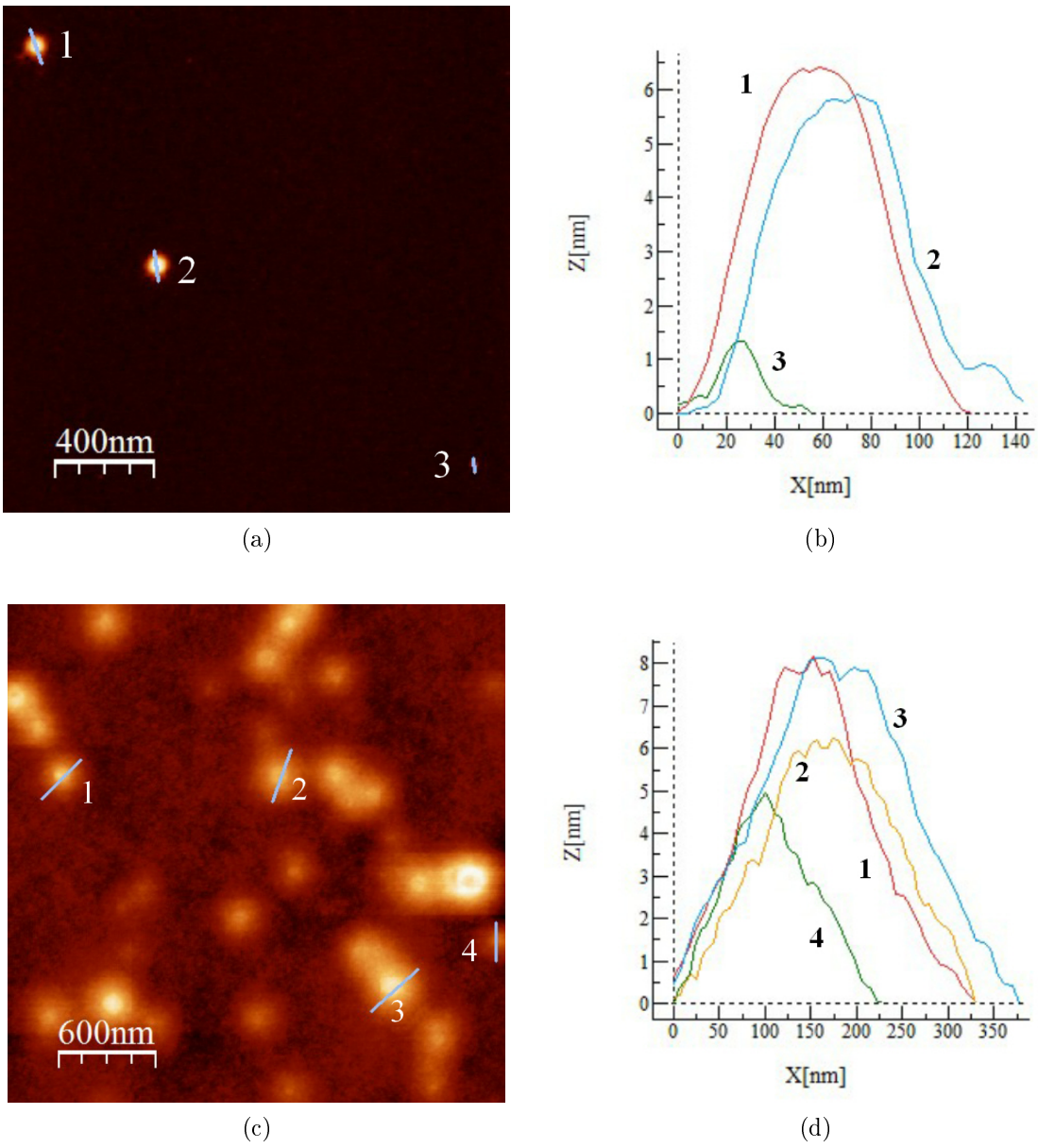

FIGURE 3.7: *AFM images of 6 kDa CM produced by loading micelles with curcumin as described in section 2.2.1.1 and their height analysis. Numbers decide the respective cross-sections. Panels (a) and (c) represent AFM images of 6 kDa CM treated with ultrasound treatment and drop deposited on a freshly cleaved mica substrate or a APTMS modified mica substrate respectively, see section 2.2.3.1. Panels (b) and (d) represent the cross-section profiles of the blue lines in panel (a) and (c).*

Panel (c) illustrates the APTMS modified mica surface, with deposited 6 kDa CM. More structures are observed in this AFM images, compared to the previously ATPMS modified mica samples, with empty micelles (see panel (a) in figure 3.5) and 1 kDa CM (see panel (c) in figure 3.6). The blue lines in panel (a) represents the cross-sections profiles in the graph in panel (d). The cross-section profiles show the structures heights, which range from 5 - 8 nm and width lengths of 225, 325 and 375 nm.

The difference observed between the 1 and 6 kDa CM deposited on APTMS modified mica substrate and freshly cleaved mica substrate, is that the micelles vary in size, amount and appearance. The AFM images of 1 and 6 kDa CM deposited on freshly cleaved mica substrate, seen in panel (a) in figures 3.6 and 3.7 show a great difference in concentration and size of micelles. Only three micelles are observed for 6 kDa CM, whereas a great variety of randomly distributed structures are observed for 1 kDa CM. The cross-section profiles for the 1 kDa CM (panel (b) in figure 3.6), imply that the observed structures are collapsed, with an uneven surface. The structures observed might not be curcumin loaded micelles, but PVP polymer chains there have produced tightly packed micelles, with a small hydrophobic core. These tightly packed micelles are a possible consequence of not sufficient curcumin in the synthesis process, leaving the polymer chains to reach stability by tight packing. The cross-section performed on the tightly packed micelles is very broad and have an uneven surface. Thereby indicating that the micelles are was collapsed on the surface, with maximum height of 3 nm. When comparing these cross-section profiles with those observed for 6 kDa CM (seen in panel (b) in figure 3.7), more well defined and broad peaks are seen, which give a more reliable representation of micelles.

The AFM image in panel (a) figure 3.6 for 1 kDa CM show few indications of little bright dots, with surrounding coronas, which are presumed to be 1 kDa micelles loaded with curcumin. The cross-section profile for C in panel (a) figure 3.6 are a representative of one, which give a more defined and narrow peak compared to the observations of the tightly packed micelles. From the NanoSight experiment it was observed that a 1 kDa CM solution treated with ultrasound resulted in a broad size distribution, which implies polymer residues and micro-aggregates. This corresponds well with the observations for the AFM image in panel (a). The AFM image might have look different, if the 1 kDa CM solution had not reserved ultrasound treatment, that may have resulted in less tightly packed micelles and several curcumin loaded micelles instead. Furthermore, the observations for 1 and 6 kDa CM deposited on freshly cleaved mica substrate contradicts the observations done for empty micelles, which imply that the micelle surfaces were positively charged and would be more attracted to the negatively charged surface. The few micelles observed for 6 kDa CM and the observations done for 1 kDa CM indicates that the curcumin micelles might not be positively charged.

When comparing the AFM images of 1 and 6 kDa CM deposited on a APTMS modified mica substrate seen in panel (c) in figures 3.6 and 3.7, a difference in size is most clear. Both AFM images show a corona formed around the hydrophobic cores and a blurry appearance. The arrangement of the micelles implies that they may be deposited on top of each other or have aggregated into larger structures; this is most obvious for 1 kDa CM. The 1 kDa CM looks to have gathered in clots and what might be tightly packed micelles can also be observed. The cross-section profile for A in panel (c) figure 3.6 is representing a micelle, that do not have a bright dot in the middle and the profile shows a 2 nm height and very broad micelle. This corresponds approximately to the observation done in panel (a) and (b). The cross-section profiles for the two other observed 1 kDa CM are very broad and edgy, in comparison to the observation for 6 kDa CM. The average height is the same for both, but the width of the cross-sections are almost doubled for 1 kDa CM. The micelles are bound to collapse when deposited on an attractive surface, but compared to the size observed in the NanoSight for 1 and 6 kDa CM, the 6 kDa CM should be wider than 1 kDa CM, due to their size difference. However, if the possibility of aggregation and the arrangement are taken into consideration, the width may be explained. The cross-section line may also be longer than the observed structure, resulting in a broader recorded width.

As mentioned, the observations for 1 and 6 kDa CM contradict the observation done for empty micelles. From the AFM images and height profiles for empty micelles (see figure 3.4), it was implied that the empty micelles had a positively charged surface, and was attracted to the freshly cleaved mica substrate, because of its negative charge. For the curcumin loaded micelles, the AFM images imply that the micelles have a negatively charges and are more attractive to the APTMS modified surface. In order to specify the exact surface charge of the individual synthesised micelles, their zeta-potentials should have been measured. In the studies by Yang et al. [46] and Liu et al. [55] they produced curcumin loaded micelles with zeta potential of 0.11 $\pm$ 0.34 mV and - 0.41 $\pm$ 0.25 mV, respectively.

3.1.3 AFM images of APTMS modified mica substrates with untreated micelles solution

The 6 kDa CM, synthesised as described in curcumin loaded micelles in section 2.2.1.1, are deposited on an APTMS modified mica substrate by the method described in section 2.2.3.1. The 6 kDa CM solution applied to the shown AFM images in panel (a) on the figures 3.8 and 3.9 have not been treated with ultrasound as described in section 2.2.3.1. The figures 3.8 and 3.9 show the untreated 6 kDa CM solution AFM images, with their height analysis from the cross-sections profiles.

On figure 3.8 are a representation of the AFM image of as produced 6 kDa CM solution, deposited on APTMS modified mica for 10 min, along with the respective height analysis. Panel (a) shows the APTMS modified mica substrate and the deposited 6 kDa CM, with blue lines representing cross-sections. The profiles for the cross-section can be seen on the graph in panel (b). The profiles show the height and width of the structures. A height range of 7 - 22 nm and a width length of 120, 135, 220 and 225 nm. On panel (a) numerous structures are observed at different sizes, covering the entire APTMS modified mica substrate, which contains the highest amount of observed structures on one sample.

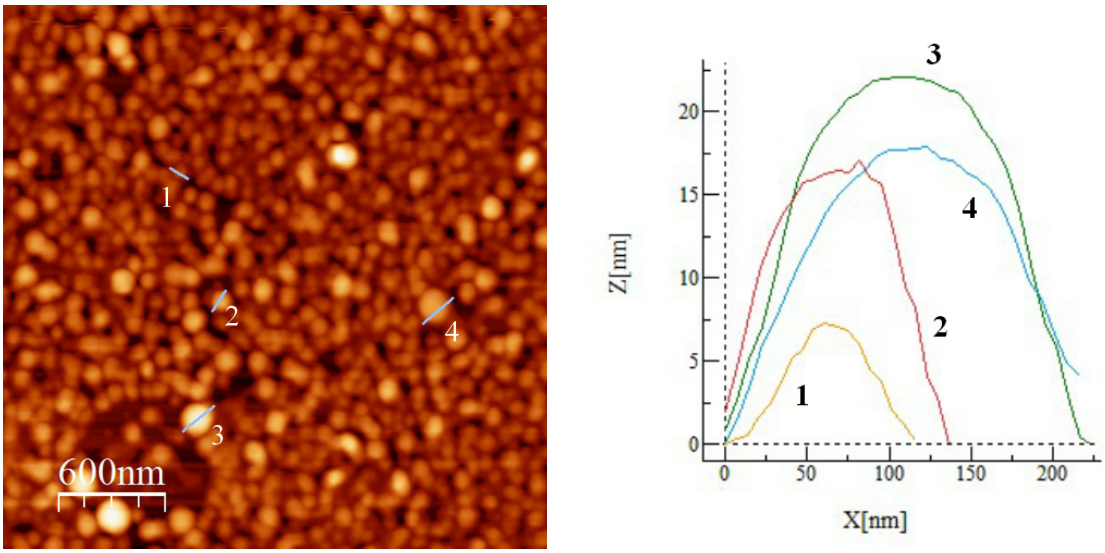

(a) (b)

Figure 3.8: *AFM image of 6 kDa CM produced by loading micelles with curcumin as described in section 2.2.1.1 along with their height analysis. Numbers decide the respective cross-sections. Panel (a) represents the AFM image of 6 kDa CM without ultrasound treatment and drop deposition on APTMS modified mica substrate for 10 min. Procedure can be found in section 2.2.3.1. Panel (b) represents the cross-section profiles of the blue lines in panel (a).*

Figure 3.9 shows the AFM image of untreated 6 kDa CM solution deposited on an APTMS modified mica substrate for 5 min, along with the respective height analysis. On panel (a) the APTMS modified mica substrate and the deposited 6 kDa CM are seen, along with blue lines indicating cross-sections. The cross-section profiles are seen on the graph in panel (b), which shows the structures height and width. The profiles show the cross-sections height range from 7 - 25 nm and a width range of 120 - 160 nm.

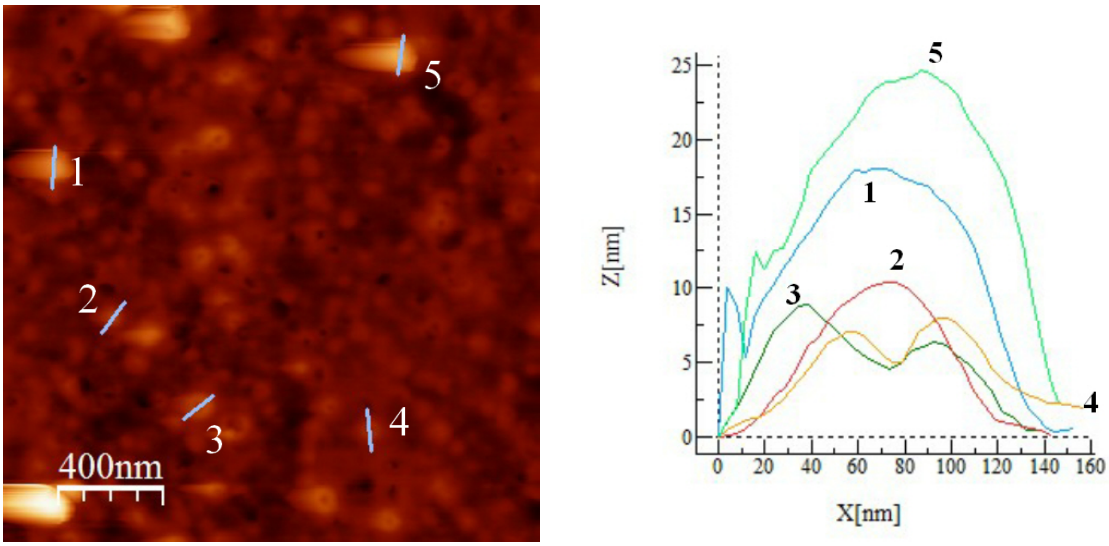

(a) (b)

FIGURE 3.9: *AFM image of 6 kDa CM produced by loading micelles white curcumin as described in section 2.2.1.1 along with their height analysis. Numbers decide the respective cross-sections. Panel (a) represents the AFM image of 6 kDa CM without ultrasound treatment and drop deposited on APTMS modified mica substrate for 10 min. Procedure is described in section 2.2.3.1. Panel (b) represents the cross-section profiles of the blue lines in panel (a).*

Two of the cross-section profiles in panel (b) figure 3.9 show a decrease in height, indicating a hole in the middle of the structures surface; this can be observed on panel (a). The decrease in height can be observed as a black dot in the middle of a spherical orange structure.

The difference in deposition time before drying was investigated, by leaving the deposited 6 kDa CM solution not treated with ultrasound on APTMS modified mica substrates for 5 and 10 min. From the AFM images seen in panel (a) in figure 3.8 and 3.9 great difference in concentration of micelles are observed. The AFM image of 6 kDa CM, with a depositing time of 10 min (see panel (a) in figure 3.8), shows an arrangement of close arranged micelles with different sizes. Numerous micelles of identical sizes are observed, which corresponds well with the size distribution analysis of 6 kDa CM not treated with ultrasound (see panel (b) in figure3.3). The height and width of some of the differently sized micelles are seen in the cross-section profiles, where the width gives a clear contrast to the size distribution. The AFM image of 6 kDa CM with a deposition time of 5 min (see panel (a) in figure 3.9), shows less micelles in comparison to a sample with 10 min deposition time. The micelle structures also appear to be larger, which is a result of the differing scale bar in each image. The scale bar for the two AFM images, the 10 min depositing time in panel (a) figure 3.8 each have a scale bar of 600 nm, while the AFM image for the 5 min depositing time in panel (a) figure 3.9 has a scale bar of 400 nm. Looking at the height profile for in panel (b) figure 3.9, micelles with a collapsed core are observed. The graph shows a decrease in the height profile for two micelle structures. This is further supported by the AFM image, where little bright dots with black dots in the middle are observed. From the observation, the AFM images imply that the 10 min deposition time yields large amounts of non-collapsed micelle structures, while 5 min deposition time results in fewer micelle structures that collapse.

3.1.4 AFM height distribution analysis

The following histograms in the figures 3.11 and 3.12 are graphic illustrations of the probability distribution of the height and radius of micelles from 10 AFM images. The AFM images are of 6 kDa CM, produced by loading micelles with curcumin, as described in section 2.2.1.1, and depositing them on a freshly cleaved mica substrate, as described in section 2.2.3.1. The images are processed by the WSxM software. Essentially, the images have their background subtracted and then a flooding function is used to estimate the average height and area of the micelles. In panel (a) of figure 3.10 one of the AFM images is seen, with its background subtracted and in panel (b) the flooding function estimation of visible structures is shown, which yields the average height and area of the visible structures.

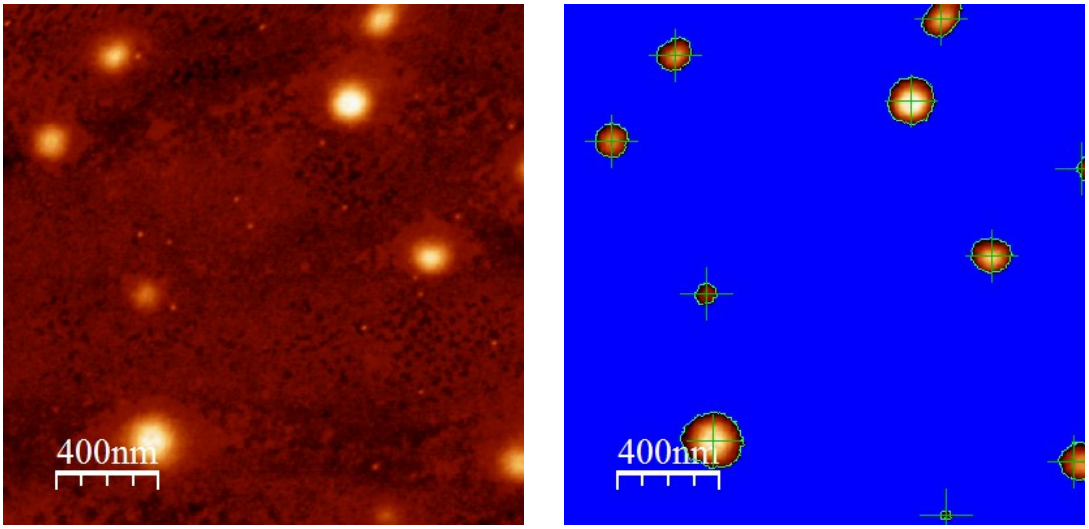

(a) (b)

Figure 3.10: *AFM image of 6 kDa CM produced by loading micelles with curcumin as described in section 2.2.1.1. Panel (a) represents the AFM image of 6 kDa CM treated with ultrasound, and drop deposited on a freshly cleaved mica substrate, see section 2.2.3.1. Panel (b) represents a WSxM produced image with micelles identified.*

The flooding function presents the height and area in histograms, which can be extracted for each AFM image and combined in the graphic illustrations seen in figures 3.11 and 3.12. The AFM images used for the distribution analysis can be seen in Appendix A

The histogram seen in figure 3.11 represent the height distribution for the 10 AFM images of 6 kDa CM deposited on freshly cleaved mica substrates. The histogram shows that most of the detected micelles have an average height of 2.5 - 3 nm. Most of their heights lie between 1 - 3 nm and very few have a height from 3 nm and up.

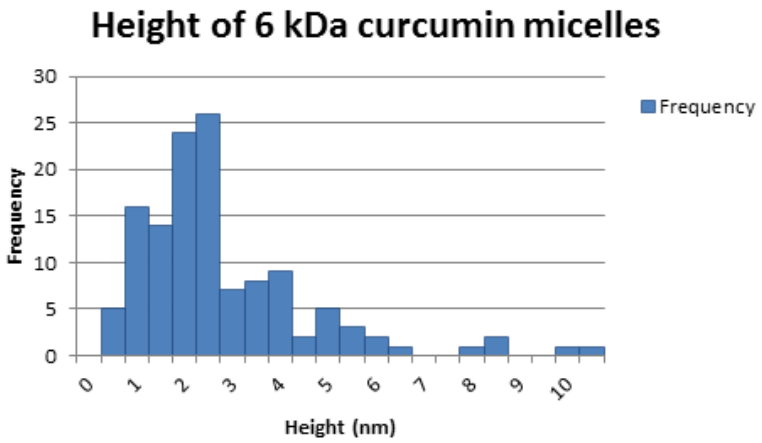

FIGURE 3.11: *The histogram represents the average height distribution of 6 kDa CM deposited on freshly cleaved mica substrates. Data obtained form 10 AFM images.*

By assuming that all the observed structures are spherical, the radius was acquired from the area estimation of the flooding function and the area equation for a sphere. The histogram seen in figure 3.12 represents the radius distribution analysis for all 10 AFM images of 6 kDa CM deposited on freshly cleaved mica substrates. The histogram shows that a high amount of the detected micelles have a radius of 50 - 60 nm.

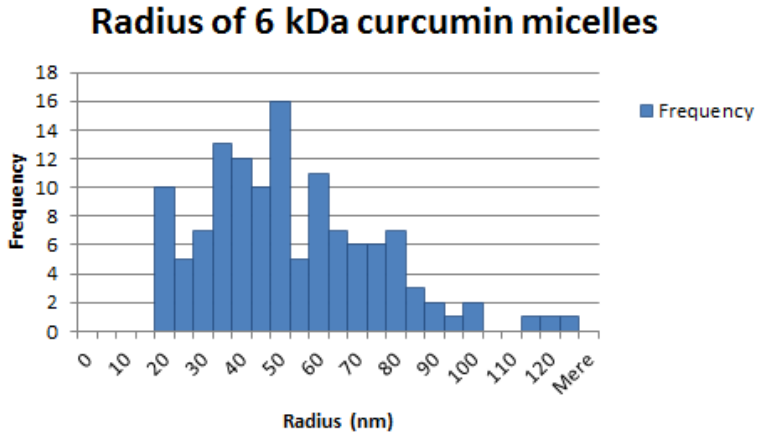

FIGURE 3.12: *The histogram represents the average radius distribution of 6 kDa CM deposited on freshly cleaved mica substrates. Data obtained form 10 AFM images.*

The height and radius distribution analysis, does not correspond to the size distribution seen for 6 kDa CM in the NanoSight (see figure 3.3). Here the micelles have a maximum size of 142 nm and when comparing this to the radius distribution analysis, the micelle diameters mostly lie in range of 50 - 60 nm, indicating that the micelles are smaller than estimated from the NanoSights size distribution. Nonetheless, it is important to consider the amount of micelles used for the analysis on both accounts. For the Nanosight analysis a larger concentration of micelles is applied, while for the AFM images only a small portion of the deposited micelles were analysed. For a more precise analysis, AFM images for the entire surface could be obtained. The height distribution gives indications of the frequency of micelles on the substrate.

3.2 Optical fluorescence microscopy

Optical fluorescence microscopy was conducted in 4 well borosilicate chambered slides. The samples were produced by incubating cells with micelles and Hoechst dye as described in section 2.2.6. For the following images in figures 3.13, 3.14, 3.15, 3.16, 3.17 and 3.19 endocytosis inhibitors are not used. Each image has a scale bar of 50 μm, unless any other condition is shown or mentioned.

Figure 3.13 represent images from the optical fluorescence microscope, where cell line CRL 2429 has been incubated with 1 kDa CM for 30 min. The images in panel (a) and (b) show a single channel obtained with filters: panel (a) represent the DAPI channel, where the cells nucleus is observed. Panel (b) represent the FITC channel, where the curcumin in the sample is observed. Panel (c) shows both channels.

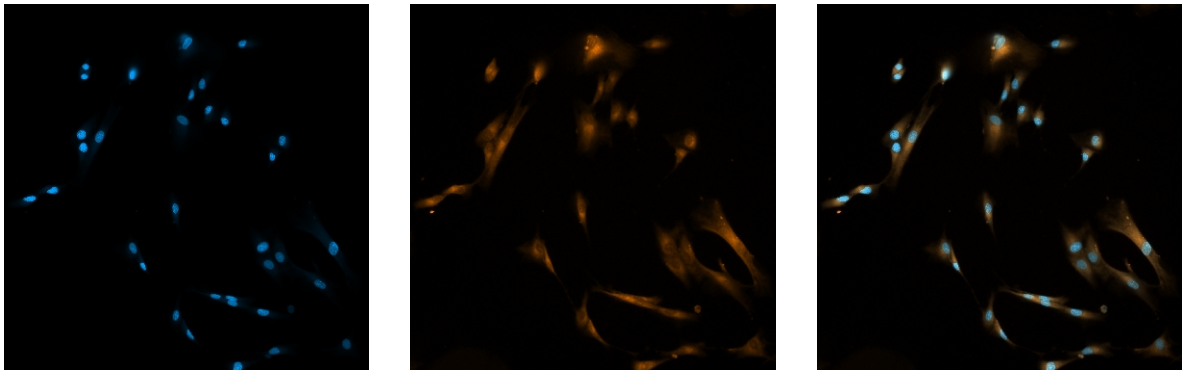

(a) (b) (c)

Figure 3.13: *Fluorescence microscope images of CRL 2429 cells incubated with a 1 mg/mL 1 kDa CM solution for 30 min. Panel (a) represent the DAPI channel with an exposure time of 100 ms. Panel (b) FITC channel with an exposure time of 200 ms and panel (c) shows both channels, with the same exposure time as before.*

The images show the CRL 2429 cells uptake of 1 kDa CM into the cells membrane. From the single channel images, it is seen how curcumin is residing in all of the cell membrane interiors, as well as where the cells nucleus is found. By combining the channels in panel (c), it can be observed how the curcumin surrounds the nucleus, from the higher fluorescence intensity of curcumin. The FITC channel in panel (b) shows that curcumin covers the entirety of the cell, including where the nucleus are seen in panel (c), with no changes in intensity. This may imply that the inner membrane does not hinder the uptake of curcumin to the nucleus. Or it could be the membrane behind the cell nucleus, since the FITC channel does not recognise the Hoescth dye and neglects it. A 3D representation of a cell would estimate if the curcumin is residing in the nucleus more clearly.

On figure 3.14 the images obtained from the optical fluorescence microscope, for cell line U87 incubated with 1 kDa CM for 30 min are shown. The images in panels (a) and (b) indicate which filter channel has been used; panel (a) represents the DAPI channel, thereby showing the cells nucleus, where panel (b) illustrates curcumin in the sample with the FITC channel. Image (c) illustrates both channels, to show the cells uptake of micelles.

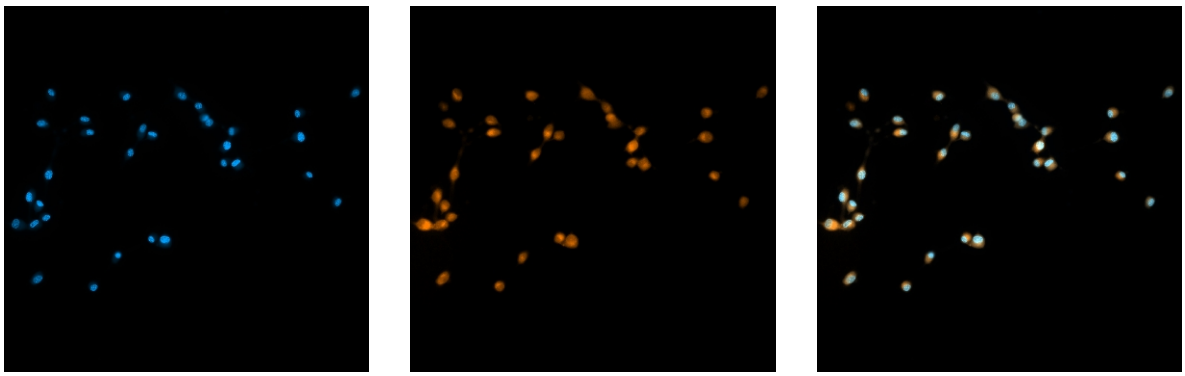

(a) (b) (c)

FIGURE 3.14: *Fluorescence microscope images of U87 cells incubated with 1 mg/mL 1 kDa CM solution for 30 min. Panel (a) represent the DAPI channel with an exposure time of 100 ms. Panel (b) FITC channel with an exposure time of 200 ms and panel (c) shows both channels, with the same exposure time as before.*

The images show the U87 cells uptake of 1 kDa CM into the cells membrane. The single channel image seen in panel (b) shows the fluorescence intensity of curcumin and at the same time gives an indication of the U87 cells size. U87 cells do not adhere sufficient to the glass surface of the slides, making them more likely to jump off the surface when washed. Therefore the cells appear very small, compared to the standard observations of the star-shaped glioblastoma cells (see section 1.5.1). The fluorescence intensity also appears more enhanced than that of the CRL 2429 cells, but their membranes are more visible and have the same enhanced intensity around the nucleus, which implies that there is no apparent difference in intensity. This is further illustrated in panel (c), where the channels are combined; it can be observed how the curcumin surrounds the nucleus, again indicating that the inner membrane does not hinder the uptake of curcumin in the nucleus.

Figure 3.15 illustrates the images obtained from the optical fluorescence microscope of cell line CRL 2429 incubated with 6 kDa CM for 30 min. The images in panels (a) and (b) show the use of one filters channel: panel (a) shows the DAPI channel, panel (b) shows the FITC channel and panel (c) shows a combination of the two channels.

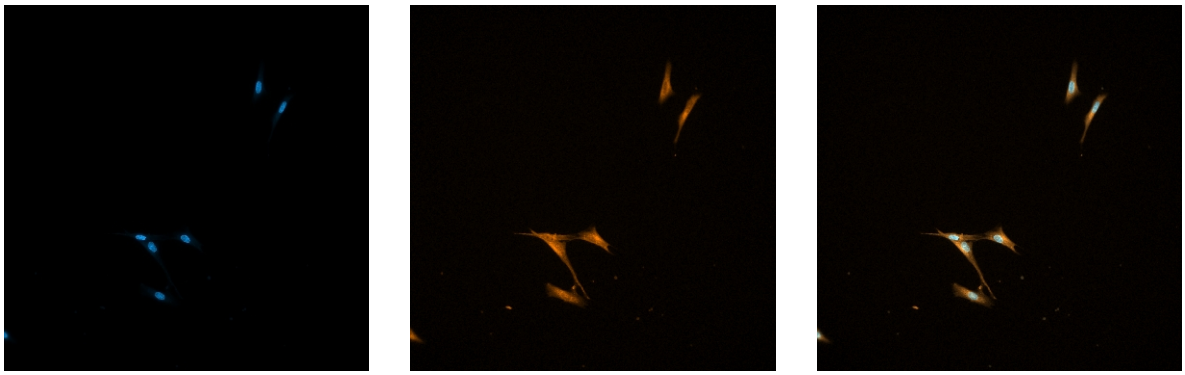

(a) (b) (c)

FIGURE 3.15: *Fluorescence microscope images of CRL 2429 cells incubated with 1 mg/mL 6 kDa CM solution for 30 min. Panel (a) represents the DAPI channel with an exposure time of 100 ms. Panel (b) shows the FITC channel with an exposure time of 200 ms and panel (c) shows both channels, with the same exposure time as before.*

On figure 3.16 three fluorescence images of the cell line U87 incubated with 6 kDa CM for 30 min are shown. The images are obtained from the optical fluorescence microscope, where panels (a) and (b) have been obtained from a single filter channel: DAPI and FICT respectively. Panel (a) illustrates the DAPI channel, where the cells nucleus can be seen and panel (b) shows the FITC channel, where the cells uptake of curcumin is seen. Panel (c) shows both channels together.

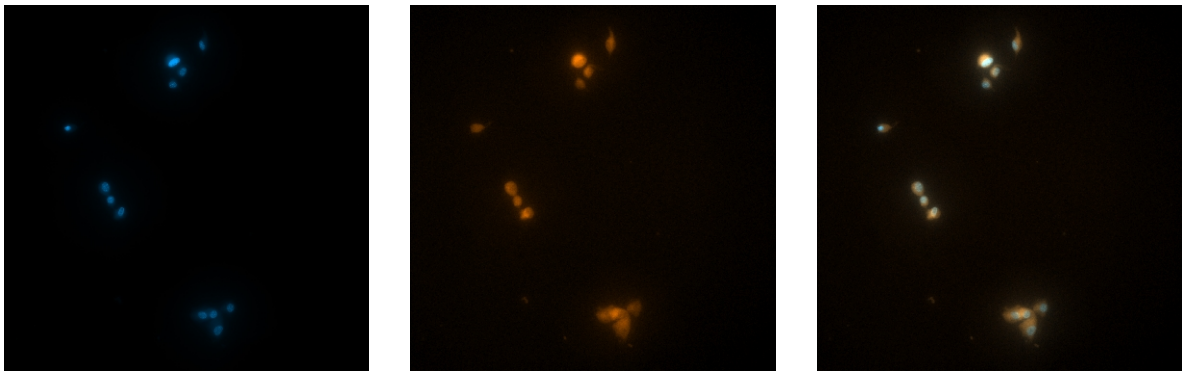

(a) (b) (c)

Figure 3.16: *Fluorescence microscope images of U87 cells incubated with 1 mg/mL 6 kDa CM solution for 30 min. Panel (a) represent the DAPI channel with an exposure time of 100 ms. Panel (b) FITC channel with an exposure time of 200 ms and panel (c) shows both channels, with the same exposure time as before.*

The fluorescence images for both CRL 2429 and U87 cells incubated with 6 kDa CM, show similar observations as for the cells incubated with 1 kDa CM (see figure 3.13 and 3.14). Curcumin shows a high fluorescence intensity around the cells nucleus, implying that the curcumin is being circulated towards the nucleus through the inner membrane, which does not hinderer its path. Few cells are observed in the images compared to those seen for 1 kDa CM, which depends on the region where the images are taken. The fluorescent intensity shows no significant difference between 1 and 6 kDa CM; both micelles types seems to have a high cellular uptake of curcumin.

Figure 3.17 represents the fluorescent microscope images of cell line CRL 2429 incubated with a free curcumin solution, with a concentration of 1 mg/mL for 30 min. The images in panels (a) and (b) show a single channel obtained with filters: panel (a) represent the DAPI channel, where the cells nucleus is observed. Panel (b) represent the FITC channel, where the curcumin in the sample is observed. Panel (c) shows both channels.

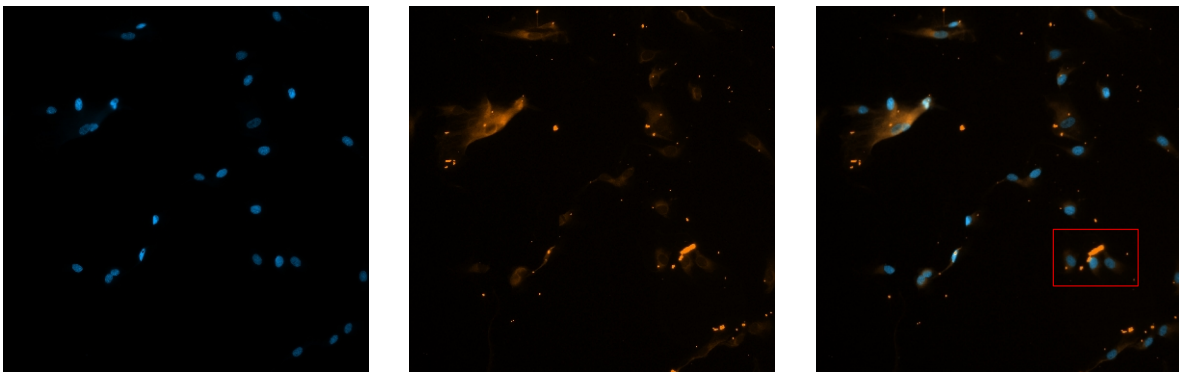

(a) (b) (c)

FIGURE 3.17: *Fluorescence microscope images of CRL 2429 cells incubated with 1 mg/mL free curcumin solution for 30 min. Panel (a) represent the DAPI channel with an exposure time of 100 ms. Panel (b) FITC channel with an exposure time of 200 ms and panel (c) shows both channels with the same exposure time as before.*

The image shows the uptake of free curcumin by the CRL 2429 cells. From the single channel images it is seen how a minimal concentration of curcumin is residing in all of the cell membrane interiors, together with a representation of the cells nucleus. The channels are combined in panel (c), where small curcumin aggregates become clearer, since they are positioned away from the cells. The fluorescent intensity of the curcumin aggregates are higher than the intensity of the curcumin residing in the cells membrane.

Figure 3.18 represent an enlarged image of figure 3.17 with a scale bar of 20 μm, showing a more precise illustration of the curcumin aggregates and the difference in fluorescent intensity. The images in panel (a) shows the FITC channel, where the curcumin is observed. From this image it is possible to observe a lower fluorescent intensity where the nuclei are placed, when comparing to panel (b) where the DAPI and FITC channels are shown. This implies the possibility that free curcumin, in comparison to curcumin micelles, may not penetrate the inner membrane of CRL 2429 cells.

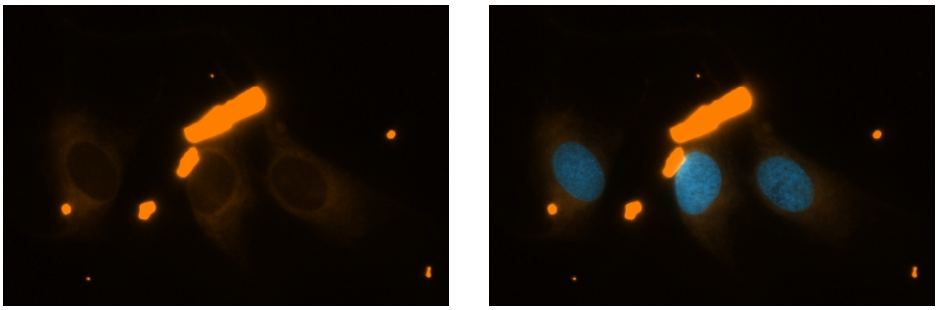

(a) (b)

FIGURE 3.18: *Zoomed fluorescent image of figure 3.17, indicated by the red square. Panel (a) shows the FITC channel with an exposure time of 200 ms and panel (b) shows both channels, with the same exposure time as before.*

On figure 3.19 are the three fluorescence microscope images of the cell line U87 incubated with a 1 mg/mL free curcumin solution for 30 min. The images seen in panels (a) and (b) show a single channel obtained with filters: panel (a) shows the application of the DAPI channel, while panel (b) shows the FITC channel. A combination of the two channels is seen in panel (c).

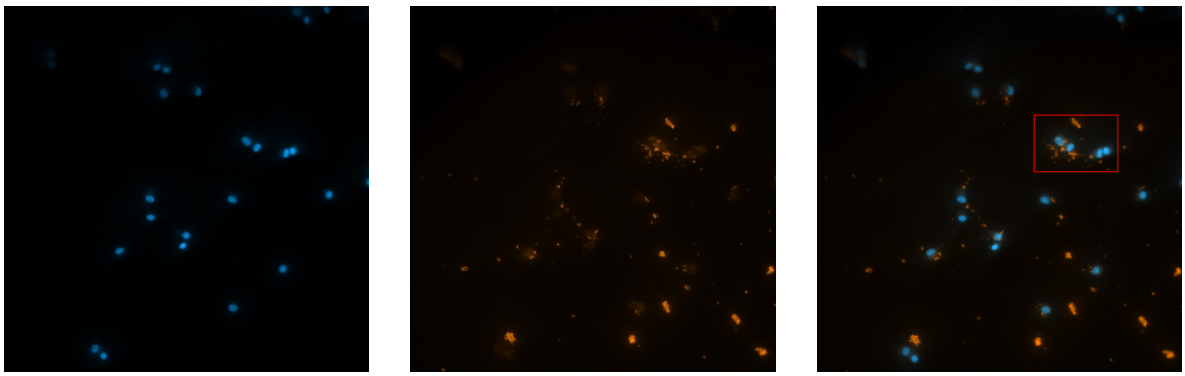

(a) (b) (c)

Figure 3.19: *Fluorescence microscope images of U87 cells incubated with 1 mg/mL 6 kDa CM solution for 30 min. Panel (a) represent the DAPI channel with an exposure time of 100 ms. Panel (b) shows the FITC channel with an exposure time of 200 ms and panel (c) shows both channels, with the same exposure time as before.*

The images show the U87 cells uptake of free curcumin. From the single channel images, it is shown that a very low concentration of curcumin resides in all of the cell membrane interiors, together with a representation of the cells nucleus. The U87 cells small size, caused by their tendency to jump off the surface when washed, makes their membrane very small. However, by observation of panel (b), the low concentration becomes more apparent. Similar to CRL 2429 cells incubated with free curcumin, small curcumin aggregates are observed in panel (c), with the combined channels. The fluorescent intensity of the curcumin aggregates are higher than the intensity of the curcumin residing in the cells membrane.

Figure 3.20 represent an enhanced imaged of figure 3.19, with a scale bar of 10 μm, showing a more precise illustration of the curcumin aggregates and the difference in fluorescent intensity. The images in panel (a) shows the FITC channel, where the curcumin is observed. The images illustrate different sizes of curcumin aggregates, in combination with the low concentration of curcumin uptake by the U87 cells. In panel (b) the DAPI channel is shown together with the FITC channel, showing the location of the nucleus among the curcumin aggregates. In comparison to figure 3.18 it appears that U87 inner membrane has been penetrated by the free curcumin.

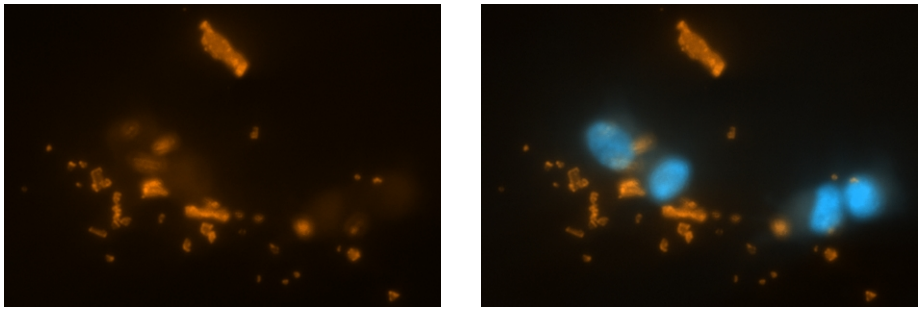

(a) (b)

Figure 3.20: *Zoomed fluorescent image of figure 3.19, indicated by the red square. Panel (a) shows the FITC channel with an exposure time of 200 ms and panel (b) shows both channels, with the same exposure time as before.*

The overall observation from the fluorescent microscope images is that the polymeric micelles enhance the cellular uptake of curcumin, compared to free curcumin. The poor solubility of free curcumin is clearly observed in the images, in the form of curcumin aggregates. No curcumin

aggregates were observed for polymeric micelles. This all helps support the application of micelles as a drug delivery system.

3.2.1 Cross sections

The following 3D fluorescence microscope images in figures 3.21 and 3.22 are each a construction of 40 z-stacked layers obtained with the DAPI, FITC and DsRed filter channels, with different exposure times. The scale bars for each image are 20 μm. The samples are produced by incubating cells with micelles and Hoechst dye as described in section 2.2.6, without incubation with endocytosis inhibitors.

The 3D images presented in figure 3.21 show the 1 kDa CM solution incubated with CRL 2429 and U87 for 30 min. Panel (a) shows the CRL 2429 cells with the DAPI and FITC channels. In addition three blue arrows can be seen. These arrows all point to the same micelle, seen from different angles.

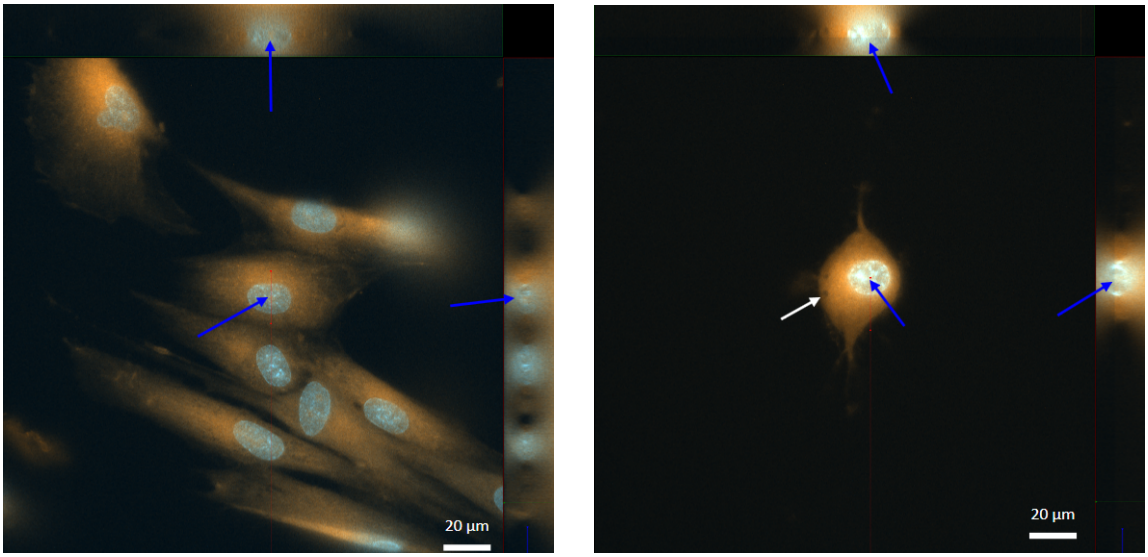

(a) (b)

FIGURE 3.21: *3D fluorescent microscope images, consisting of 40 z-stacked layers, showing CRL 2429 and U87 cells incubated with a 1 mg/mL 1 kDa CM solution for 30 min. The images are obtained by using the DAPI and FITC channels, and the exposure time is different for each image. Panel (a) show the 3D representation of CRL 2429 cells, with an exposure time of 6 ms and 600 ms. Panel (b) show the 3D representation of U87 cells, with an exposure time of 6 ms and 850 ms. The blue arrows points to the cross section of the image, while the white arrows points to a vesicle in the cells interior.*

In panel (b) cell line U87 incubated with 1 kDa CM is seen with the DAPI and FITC channels. Furthermore, three blue and one white arrow are shown on the image, to highlight the cross-section point and a vesicle in the cells interior, respectively.

The 3D images presented in figure 3.21 shows the 6 kDa CM solution incubated with CRL 2429 and U87 for 30 min. Panel (a) shows the CRL 2429 cells with the DAPI and DsRed channels. In addition three blue and one white arrow have been inserted. The blue arrows indicate the point of cross-section of the image, while the white arrow illustrates a vesicle with curcumin in the cells interior.

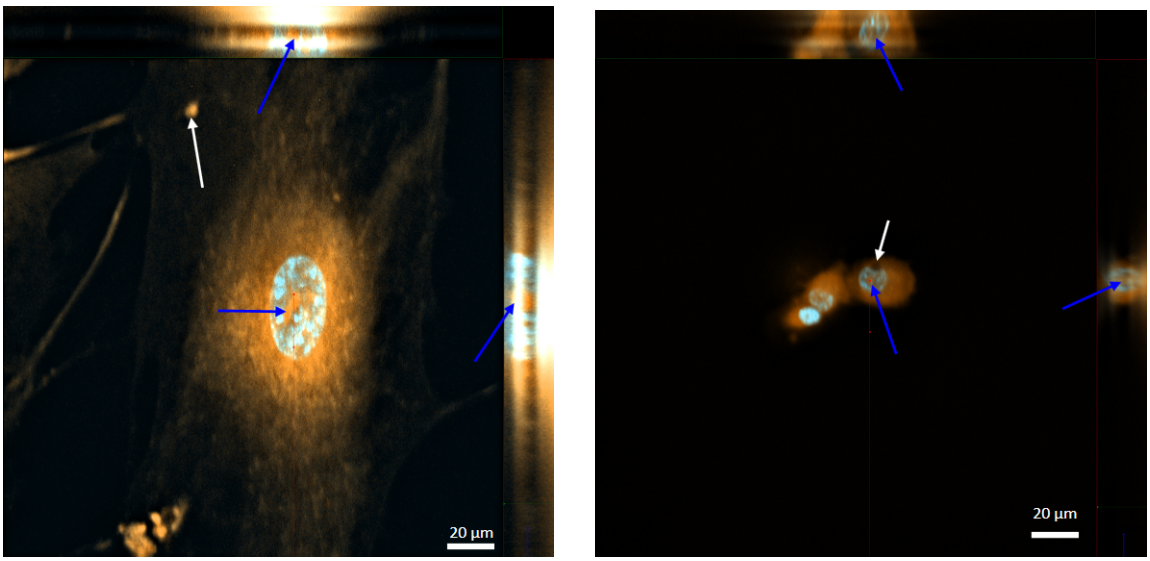

(a) (b)

Figure 3.22: *3D fluorescent microscope images, consisting of 40 z-stacked layers, showing CRL 2429 and U87 cells incubated with a 1 mg/mL 1 kDa CM solution for 30 min. The images are obtained by using the DAPI and DsRed channels, with exposure times of 100 ms and 700 ms. Panel (a) show the 3D representation of CRL 2429 cells. Panel (b) show the 3D representation of U87 cells. The blue arrows points to the cross section of the image, while the white arrow points to a vesicle in the cells interior.*

In panel (b) cell line U87 incubated with 6 kDa CM is observed with the DAPI and DsRed channels. In addition three blue and one white arrow are shown on the image, to highlight the cross-section point and a vesicle at the border to the cells nucleus, respectively.

The U87 images are not optimal, because of their small size and quality, but they efficiently show the effect of the curcumin cellular uptake. Each image shows that the curcumin has been distributed uniformly throughout the cell membranes, while the cross-section point indicates that some of the curcumin has reached the nucleus. In panel (a) figure 3.22, what looks to be a curcumin vesicle in the CRL 2429 cell nucleus is observed at the cross-section point. Panel (a) in figure 3.21 shows no signs of curcumin in its nucleus, which is also observed for U87 cells incubated with 1 kDa curcumin. Panel (b) in figure 3.22 may illustrate a vesicle in the nucleus, but the quality of the images makes it difficult to determine. If this observation is true, it implies that 6 kDa CM have the ability to transport curcumin to the cell nucleus. Further studies of this observation is needed, to make a more definite determination, such as more optimal and additionally images of this observation. There is the possibility, that the curcumin vesicle observed is a reflection. In the cell membrane on figure 3.22 panel (a), a spherical aggregate is observed, which may be a vesicle containing curcumin, thereby showing the endocytosis process of the CRL 2429 cell. The U87 cells in both figures show, what is thought to be an empty vesicle in their membrane and close to their nucleus, because of the non-exciting fluorescent intensity. It can be a result of the image quality or molecules in the PBS medium, which reside above the cells and interfere with the images.

3.2.2 Endocytosis routes

In order to investigate the endocytosis routes for the micelles, experiments have been conducted with various endocytosis inhibitors, dynasore hydrate and worthmaninn, to hinder some pathways into the cells. In the following images comparisons between cells incubated with and without endocytosis inhibitors are shown for both cell lines. The samples are produced by incubating cells with micelles and Hoechst dye as described in section 2.2.6.

3.2.2.1 Cell line U87 with and without endocytosis inhibitors

On figure 3.23 three fluorescent microscope images of U87 are shown, incubated with 1 kDa CM, worthmaninn and dynasore for 30 min. Panel (a) shows the sample incubated only with 1 kDa CM, with the DAPI and FITC channels. In panel (b) the sample pre-incubated with dynasore is seen, also with the DAPI and FITC channels.

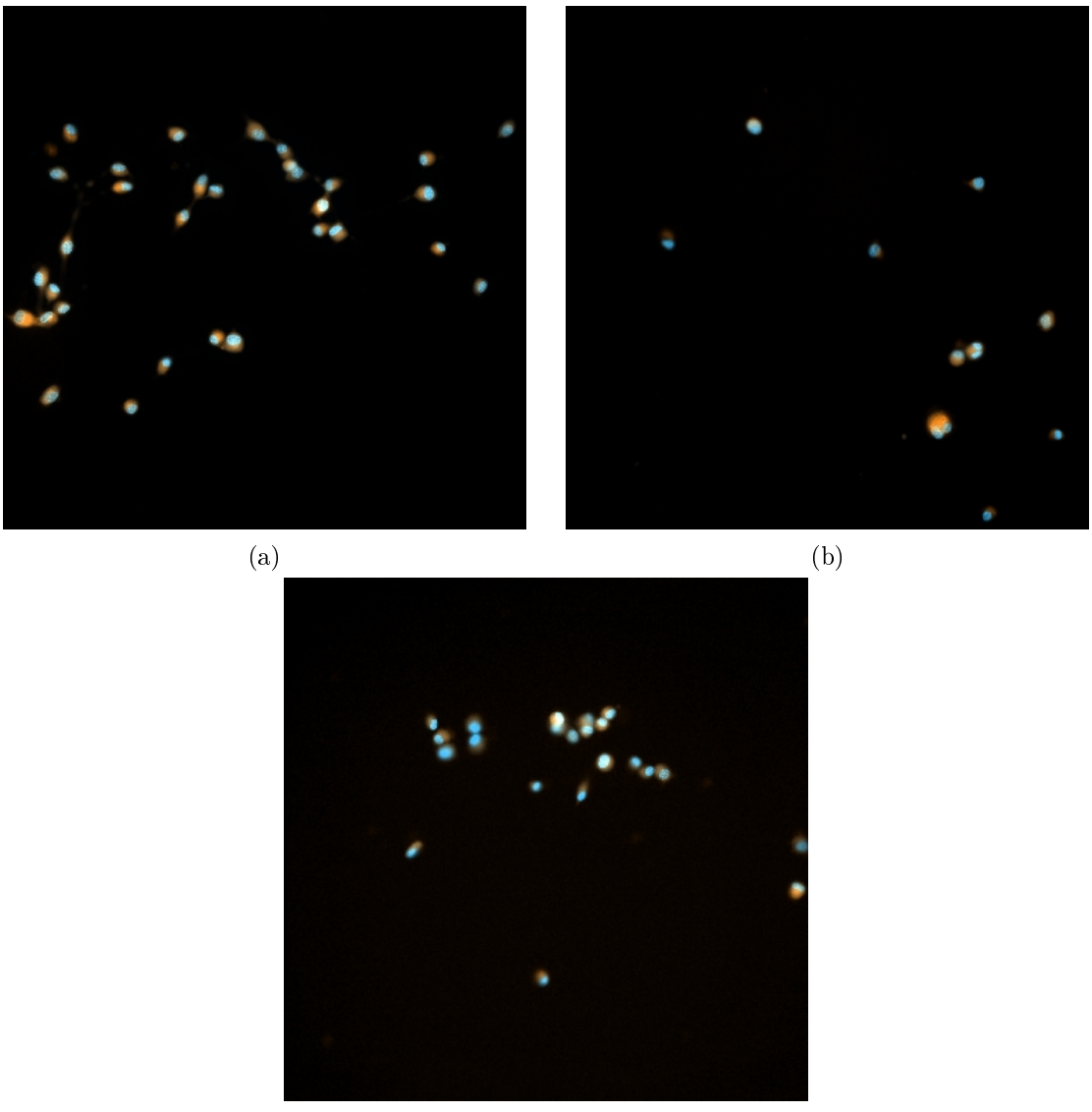

(a) (b)

(c)

FIGURE 3.23: *Fluorescence microscope images of U87 cells incubated with 1 mg/mL 1 kDa CM solution, worthmaninn and dynasore for 30 min. Panel (a) shows the sample without any inhibitors, panel (b) shows the sample pre-incubated with dynasore and panel (c) the sample pre-incubated with worthmaninn. The images are obtained with DAPI and FITC channels, with the exposure times of 100 and 200 ms.*

On the last panel (c) the sample pre-incubated with 1 kDa CM and worthmaninn is illustrated. Here are the DAPI and FITC channels used. As mentioned previously, U87 cells do not adhere sufficiently to the glass surface of the slides, making them more likely to jump off the surface when washed, explaining the few and small cells observed in the images. Additionally, the cells exhibit no difference in cellular uptake of curcumin, when pre-incubated with the endocytic inhibitor dynasore and receptor mediated endocytosis inhibitor Worthmaninn. The fluorescence intensity is similar for all the images.

Figure 3.24 represents three fluorescence microscope images of cell line U87 incubated with a 6 kDa CM solution, with and without the inhibitors dynasore and worthmaninn. Panel (a) shows the incubated cell without inhibitors and panel (b) shows the cells pre-incubated with dynasore and 6 kDa CM. Both images are obtained with the DAPI and DsRed channels in the optical fluorescence microscope.

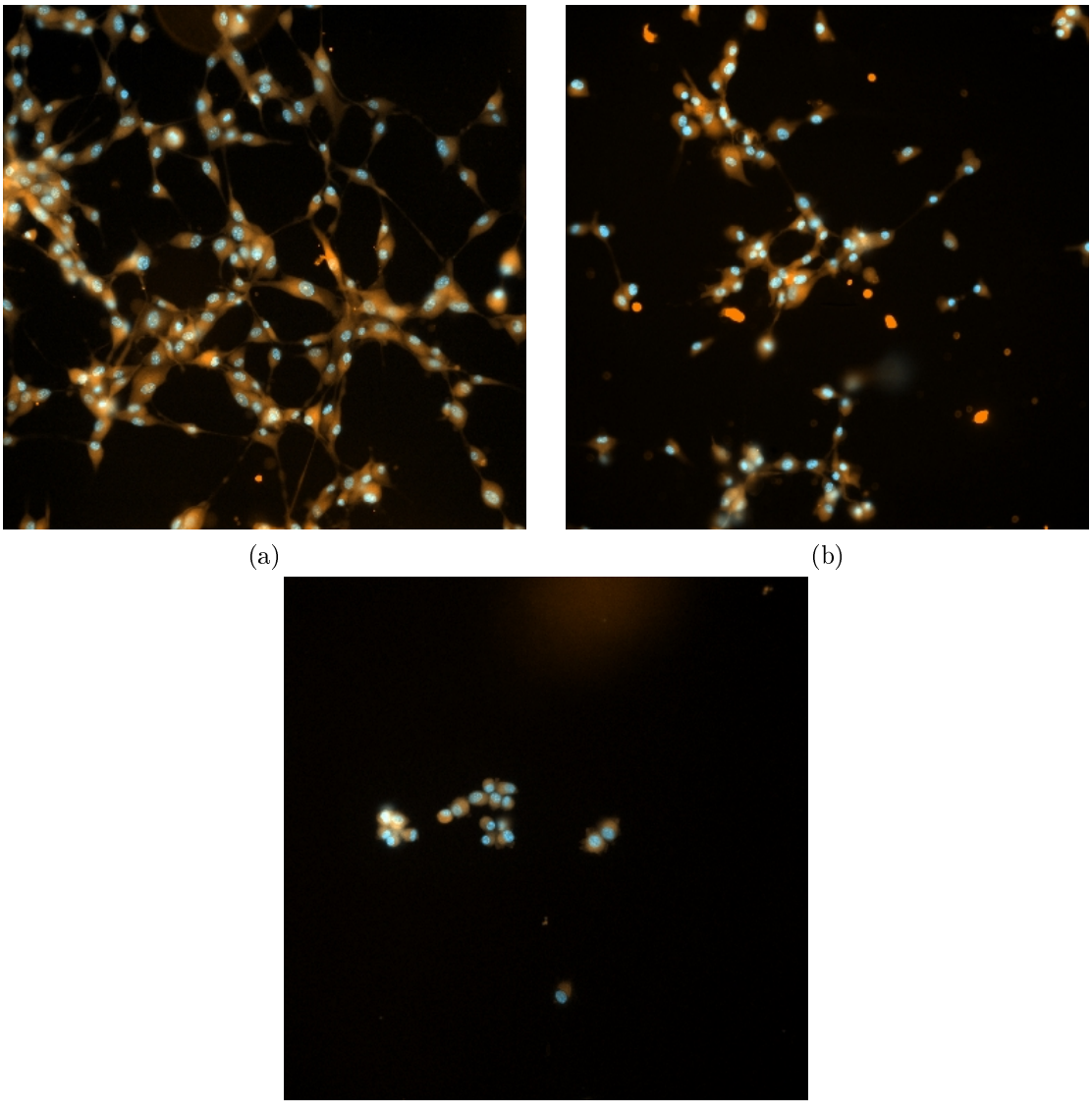

(a) (b)

(c)

Figure 3.24: *Fluorescence microscope images of U87 cells incubated with 1 mg/mL 6 kDa CM solution, worthmaninn and dynasore for 30 min. Panel (a) shows the sample without any inhibitors, panel (b) show the sample pre-incubated with dynasore and panel (c) the sample pre-incubated with worthmaninn. The images are obtained with the DAPI and DsRed channels, with an exposure times of 15 and 950 ms for (a) and (b), while (c) is obtained with the DAPI and FITC channels, with the exposure times 100 and 200 ms.*

In panel (c) the cells pre-incubated with worthmaninn are seen; the image was obtained with the DAPI and FITC channels. The amount of cells seen in each image differs for each sample. In panels (a) and (b) the U87 cells have their characteristic star-shape, showing that the cells are still adhering to the slides surface. This results in more cells, since they are not washed away during the sample production. In the panels, there are areas with high concentrations of curcumin, which can be representative of a micelle core or curcumin residue from the 6 kDa CM solution, even though it has been centrifuged. The curcumin structures resemble the curcumin aggregate seen in figure 3.19, where the cells were incubated with free curcumin. Furthermore what appeasers to be reflections are observed in all the images, which can be from the attached chambers, where the light is reflected back on the slides surface. Nevertheless, the cells exhibit no difference in cellular uptake of curcumin when pre-incubated with the endocytic inhibitor dynasore and receptor mediated endocytosis inhibitor Worthmaninn, matching the result obtained from 1 kDa CM.

3.2.2.2 Cell line CRL 2429 with and without endocytosis inhibitors

On figure 3.25 three fluorescent microscope images of cell line CRL 2429, incubated with a 1 kDa CM solution with and without the endocytosis inhibitors dynasore and worthmaninn, are illustrated. Panel (a) represents the cells only incubated with 6 kDa CM, with the DAPI and FITC channels. In panel (b) the cells which have been pre-incubated with dynasore can be seen, with the DAPI and FITC channels.

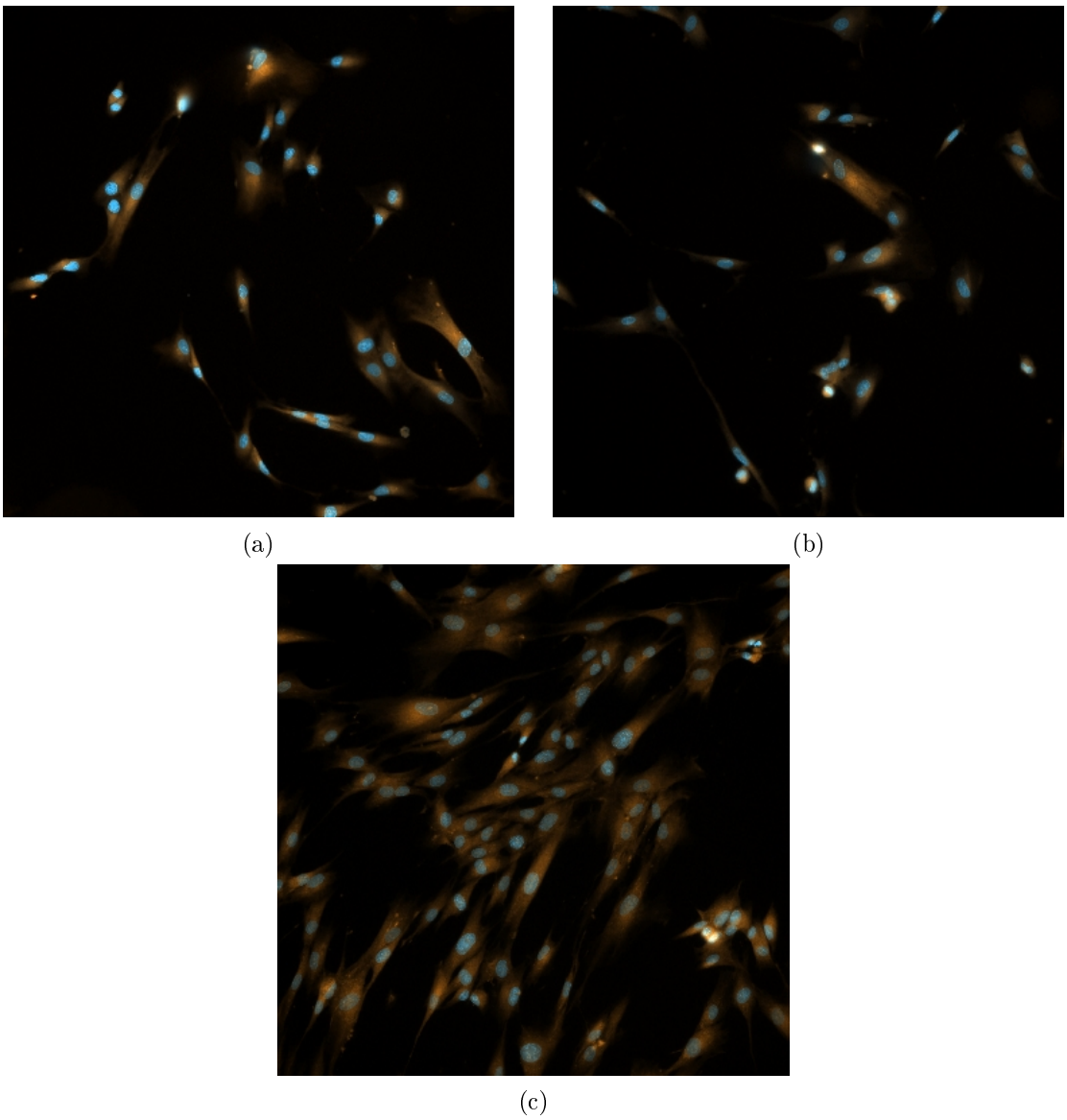

(a) (b)

(c)

Figure 3.25: *Fluorescence microscope images of CRL 2429 cells incubated with a 1 mg/mL 1 kDa CM solution, containing worthmaninn and dynasore for 30 min. Panel (a) shows the sample without any inhibitors, panel (b) shows the sample pre-incubated with dynasore and panel (c) the sample pre-incubated with worthmaninn. The images are obtained with DAPI and FITC channels, with the exposure times of 100 and 200 ms for (a) and (b), while (c) is obtained with the DAPI and DsRed channels, with the exposure time 100 ms and 1 s.*

Panel (c) shows the cells pre-incubated with the inhibitor worthmaninn, with the DAPI and DsRed channels. A large difference in the amount of cells can be seen between image (a) and (b), as compared to image (c). The difference in cell concentration can be the cause of different obtained confluence for each sample, or the image region of the sample. Comparable to the U87 cells, the CRL 2429 cells do not exhibit difference in cellular uptake of curcumin when pre-incubated with inhibitors. The images do show many presumed curcumin vesicles in the cells membrane in all the samples. Additionally, there is a high difference in exposure time for the FITC and DsRed channels, which is provoked by the sample curcumins fluorescent intensity which diminishes over time. Exposure to light will also influence the intensity of the fluorescent dyes.

Figure 3.26 represents three fluorescence microscope images of CRL 2429 cells incubated with a 6 kDa CM solution, with and without the endocytosis inhibitors dynasore and worthmaninn.

In panel (a) the cells incubated only with 6 kDa CM are seen, while panel (b) shows the cells pre-incubated with dynasore and 6 kDa CM. Both images are obtained with the DAPI and DsRed channels.

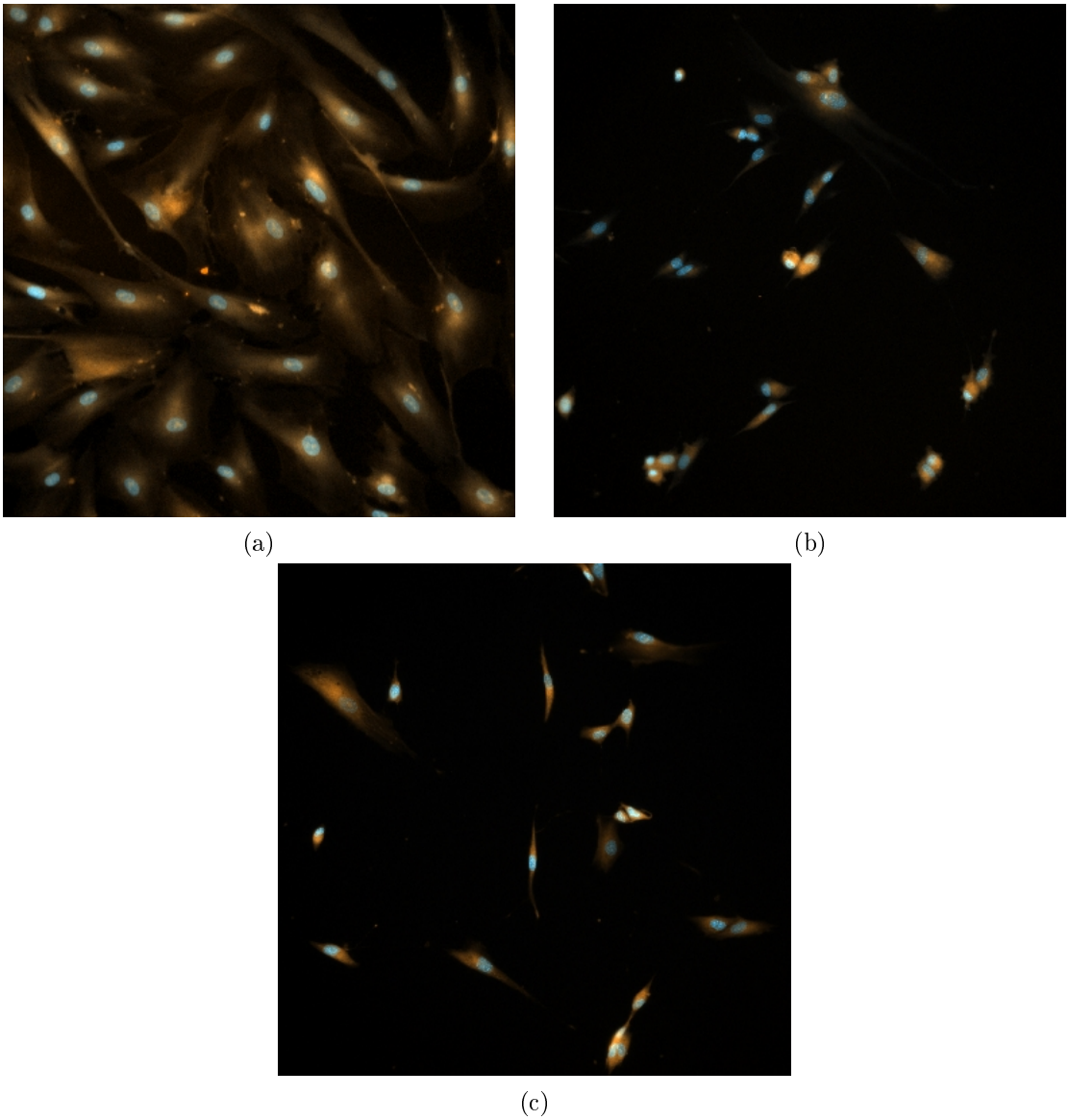

FIGURE 3.26: *Fluorescence microscope images of CRL 2429 cells incubated with a 1 mg/mL 6 kDa CM solution, worthmaninn and dynasore for 30 min. Panel (a) shows the sample without any inhibitors, panel (b) shows the sample pre-incubated with dynasore and panel (c) the sample pre-incubated with worthmaninn. The images are obtained with DAPI and DsRed channels, with the exposure times of 100 and 700 ms for panel (a) and with a exposure times of 100 ms and 1 s for panel (b) and (c).*

In panel (c) the cells pre-incubated with worthmaninn are shown. The image has, like the others, been obtained with the DAPI and DsRed channels. A small difference in the amount of CRL 2429 cells is seen between each image. Again the cells exhibited no difference in their cellular uptake of curcumin when pre-incubated with the endocytosis inhibitors. Dynasore has been shown to inhibit the cellular uptake, depending on dynamic functions such as Clathrin-dependent and Cavolin-dependent pinocytosis. [73] Fluorescent microscopy is not the most optimal way to estimate inhibited cellular uptake of cells; therefore further investigation is necessary to determine dynasore inhibiting ability towards the synthesised micelles.

3.3 Cytotoxicity assay

The inter-cellular drug delivery release of curcumin and empty micelles is investigated using a multi-mode plate reader and a CytoTox-ONE^{TM} assay kit, as described in section 2.2.5. Light micro-graphs from before and after the 24 h incubation period, with different micelles types and concentrations, can be seen in Appendix B. The multi-mode plate reader measures the release of LDH from cells with a damaged membrane, using an excitation wavelength of 560 nm and an emission wavelength of 590 nm. The standard deviation values are based on 9 data points for 1 kDa and 6 kDa CM as well as for the empty micelles, whereas it is based on 3 - 4 points for free curcumin.

3.3.1 Curcumin loaded micelles

3.3.1.1 Cell line CRL 2429

Figure 3.27 shows the results from the cytotoxicity assay using CRL 2429 and 1 kDa and 6 kDa CM at concentrations of 1, 0.1, 0.01 and 0.001 mg/mL, as well as free curcumin with a concentration of 1 mg/mL. On the graph three data sets can be seen, where the cells have been incubated with free curcumin, 1 kDa CM and 6 kDa CM respectively, for 24 hours. The 6 kDa CM curve starts at ∼5% mortality and decreases slightly to ∼2%, after which it continues to increase from ∼9% to ∼60% mortality.

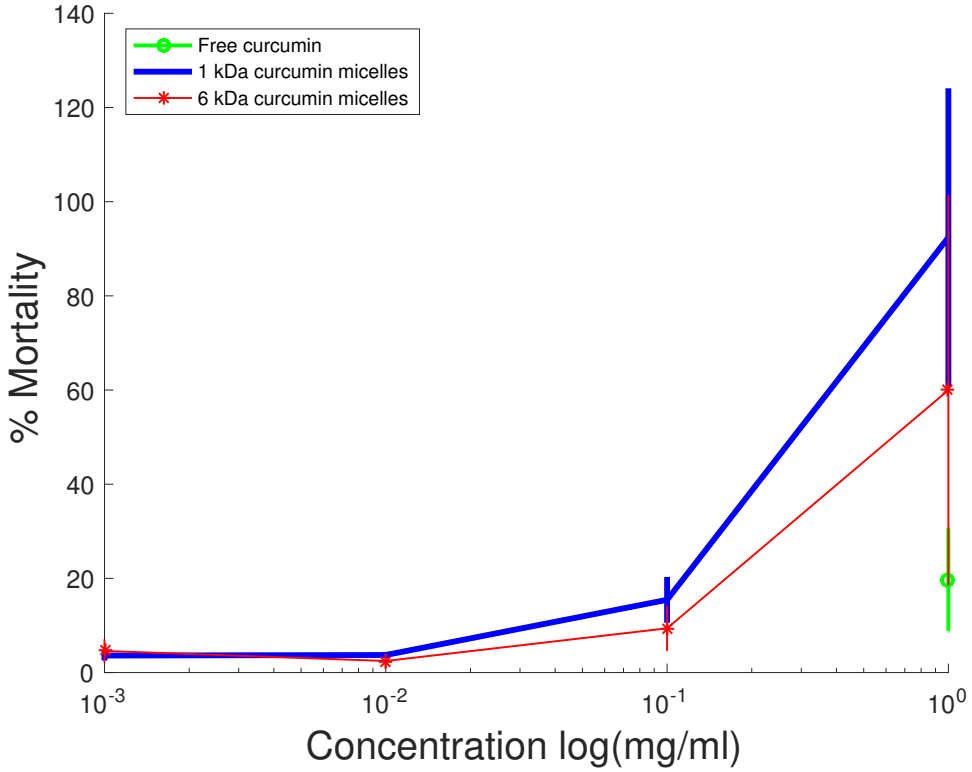

Figure 3.27: *The graph represents the mortality % for CRL 2429 cells after 24 hours incubation with different concentrations of 1 and 6 kDa CM, as well as free curcumin with a concentration of 1 mg/mL. Each data point is an average of 9 measurements for 1 kDa and 6 kDa CM, while it is an average of 3 measurements for free curcumin. The same goes for the standard deviation values.*

The 1 kDa CM curve starts at ∼3% mortality and remains there until the concentration reaches 0.01 mg/mL. Afterwards the mortality increases to ∼15% and continues up to ∼92%. The standard deviation values increase with the concentration of 1 and 6 kDa CM. For free curcumin the mortality % is at ∼20% for a solution of 1 mg/mL.

Both 1 kDa and 6 kDa CM show an exponential curve, where 1 kDa remains higher in mortality % than 6 kDa CM. CRL 2429 are skin cells, making them a part of the human body frame structure, placing them in the healthy cell category. The high mortality of ∼92% for 1 kDa CM are therefore far from an ideal result, which also can be stated for 6 kDa CM mortality of ∼60%. Both mortality % are obtained at a concentration of 1 mg/mL, indicating that the concentration has to be reduced. A general overview of the graph shows that the cytotoxic activity increases with an increase in concentration, and that curcumin loaded in 1 and 6 kDa PVP polymers enhances the cytotoxic activity of curcumin, as compared to the free curcumin solution at 1 mg/mL.

In figure 3.28 a concentration deduction of the cytotoxicity assay results for cell line CRL 2429 is shown, with 1 and 6 kDa CM and free curcumin at concentrations of 0.2, 0.4, 0.6 and 0.8 mg/mL. On the graph three data sets can be seen, where the cells have been incubated with free curcumin, 1 kDa CM and 6 kDa CM, respectively for 24 hours. The curve for 6 kDa CM shows an adequate linear increase in mortality %, with an increase from ∼7% to ∼36%. Free curcumin shows a more exponential increase from ∼2% to ∼16% mortality. Standard deviation values for free curcumin increase with the increase in concentration.

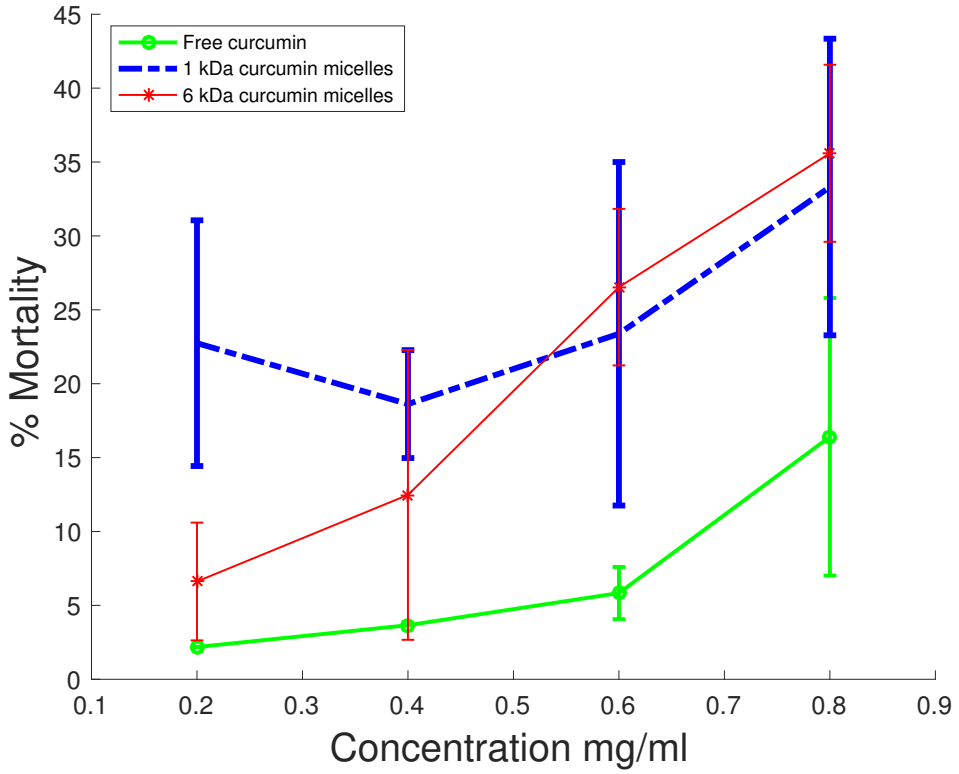

FIGURE 3.28: *The graph represent the mortality % of CRL 2429 cells after 24 hours of incubation with different concentrations; 0.2, 0.4, 0.6 and 0.8 mg/mL of free curcumin, 1 kDa and 6 kDa CM. Each data point is an average of 9 measurements for 1 and 6 kDa CM, while it is an average of 3 measurements for free curcumin.*

For 1 kDa CM, a curved line is seen, with a starting point at ∼23% mortality, followed by a decrease to ∼ 19%. The curve then increases slightly to ∼23% and ends at ∼33%. Both 1 and 6 kDa CM standard deviation values differ for each point.

The mortality for both 1 and 6 kDa has decreased to below 50% for the highest concentration at 0.8 mg/mL, when compared to figure 3.27. A full curve is seen for free curcumin and its cytotoxic activity also rises with an increase in concentration. The 6 kDa CM curve is shown to fit well with the curve seen in figure 3.27, whereas 1 kDa CM seems higher than previously observed. The standard deviation for 1 kDa CM is very high for the entire curve, which can be caused by its poor ability to dissolve properly. The pipetting and the amount of cells in the two individual experiments can have an effect on the observed result. The cytotoxic activity for 1 and 6 kDa CM is very dependent on concentration, but even with the high mortality %, 6 kDa CM appears to be less cytotoxic towards CRL 2429 than 1 kDa CM.

3.3.1.2 Cell line U87

Figure 3.29 shows the results for the cytotoxicity assay, with U87 cells incubated for 24 h, with 1 and 6 kDa CM at concentrations of 1, 0.1, 0.01 and 0.001 mg/mL, as well as free curcumin with a concentration of 1 mg/mL. On the graph three data set can be seen, where the cells have been incubated with either free curcumin, 1 kDa CM or 6 kDa CM. The curve for 6 kDa CM shows a small increase from ∼4% mortality to ∼7% followed by a slight decrease to ∼6% for the concentrations 0.001, 0.01 and 0.1 mg/mL. Between the concentrations of 0.1 and 1 mg/mL a rapid increase in mortality % is seen for 6 kDa CM, reaching up to ∼46%.

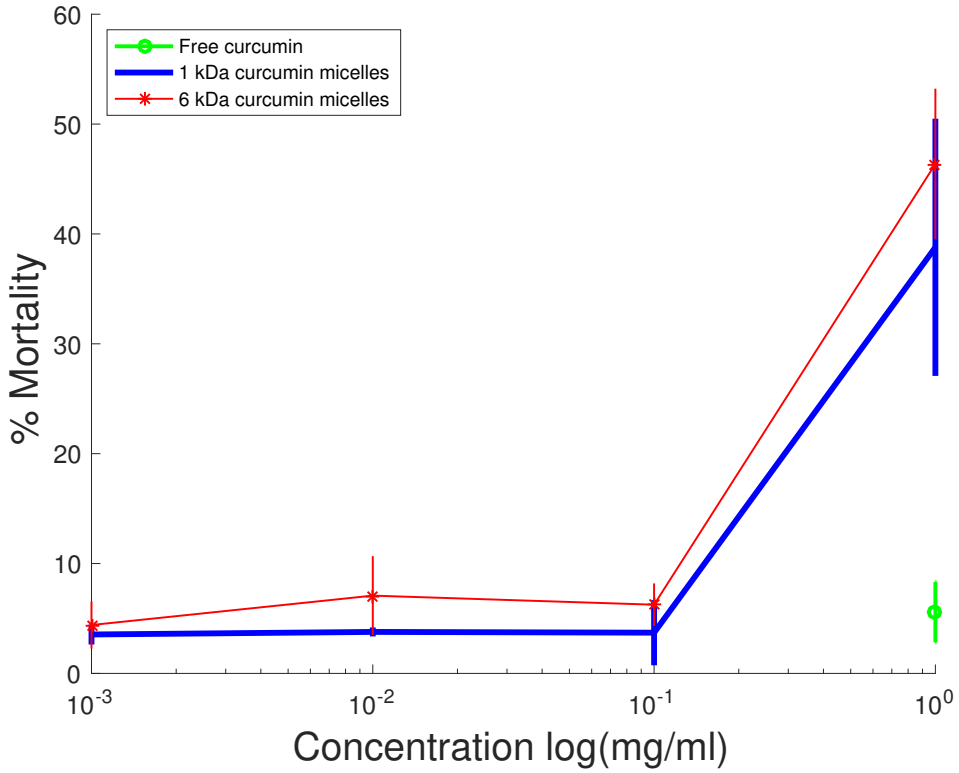

Figure 3.29: *The graph represent the mortality % of U87 cells after a 24 hour incubation with different concentrations: 0.001, 0.01, 0.1 and 1 mg/mL of 1 kDa and 6 kDa CM, as well as free curcumin with a concentration of 1 mg/mL. Each data point is an average of 9 measurement for 1 kDa and 6 kDa CM, while it is an average of 3 measurement for free curcumin.*

The curve for 1 kDa CM shows a constant mortality % of ∼4% for the lowest concentrations: 0.001, 0.01 and 0.1 mg/mL. A rapid increase is seen at 1 mg/mL, where the mortality is at ∼39%. The standard deviation values for 1 kDa CM are only seen for 0.1 and 1 mg/mL. For free curcumin, the mortality % is at ∼6% for a solution of 1 mg/mL.

Both 1 and 6 kDa CM are shown to have an almost constant cytotoxic activity at the lowest concentrations, where 6 kDa CM has a slightly higher mortality % than 1 kDa CM. Since U87 are brain tissue cells affected with glioblastoma, these are categorised as tumour cells; therefore an inhibition effect on the cells is wanted. The inhibition effect is seen from the mortality %. The high mortality of ∼46% for 6 kDa CM is therefore an adequate result. When incorporating the high mortality % for 6 kDa CM from figure 3.27, the situation becomes less favourable. This comparison shows that 1 mg/mL of 6 kDa CM may inhibit the tumour growth with 50%, but the probability of damaging or killing the surrounding cells are at 60%. For 1 kDa CM the comparison would imply an inhibition of 40% and a probability of damaging or killing the surrounding cell of 90%, thereby making 6 kDa CM the more favourable of the two synthesised micelles. This again indicates that the concentration has to be reduced. As seen in figure 3.27, the curcumin loaded 1 and 6 kDa PVP polymer enhances the activity of curcumin.

On figure 3.30 a concentration deduction for the cytotoxicity assay results for cell line U87 is shown for different concentration: 0.2, 0.4, 0.6 and 0.8 mg/mL for 1 and 6 kDa CM, and free curcumin. On the graph three data sets can be seen, where the cells have been incubated with free curcumin, 1 and 6 kDa CM respectively. The curve for free curcumin shows an almost constant mortality % of ∼2% between concentration of 0.2 - 0.4 mg/mL, followed by a slight decrease to 1% at 0.6 mg/mL. At concentrations of 0.8 mg/mL, the curve increases to its highest mortality % at ∼6%. Here the largest standard deviation is seen for free curcumin. The 1 kDa CM curve starts at its highest mortality % at ∼57% at the lowest concentration of 0.2 mg/mL, and decreases to ∼40% at a concentration of 0.4 mg/mL. The mortality increases further at higher concentrations and ends at ∼50% mortality. The standard deviation values for 1 kDa CM at the high concentrations are almost constant. The highest deviation value is seen at 0.2 mg/mL.

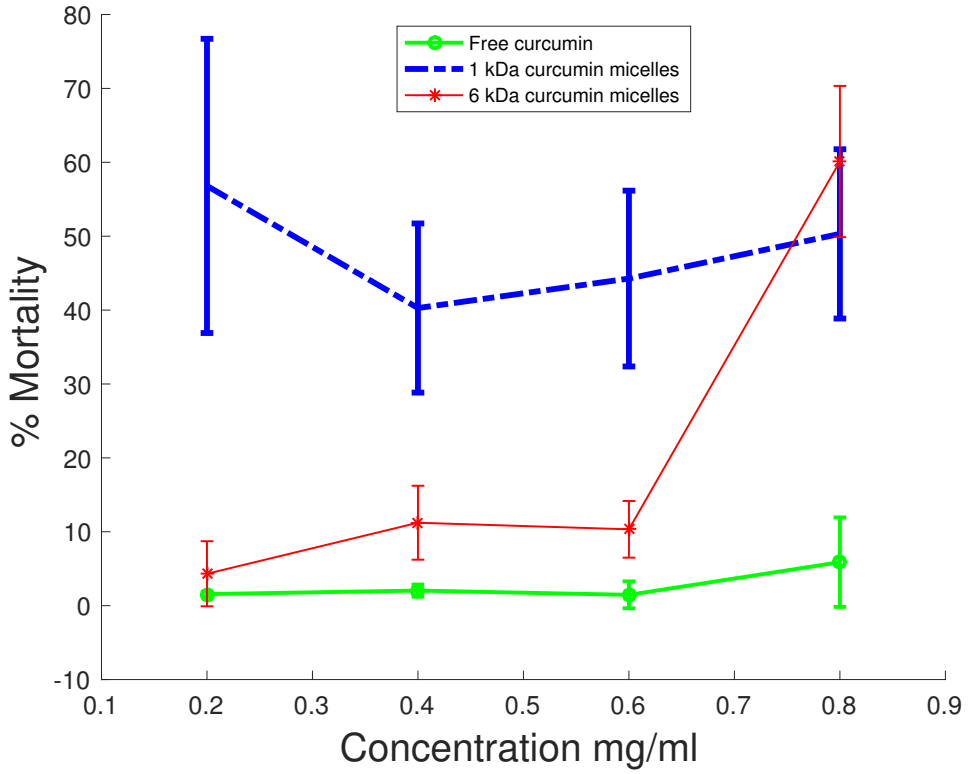

Figure 3.30: *The graph represents the mortality % of U87 cells after 24 hours incubation with different concentrations: 0.2, 0.4, 0.6 and 0.8 mg/mL of free curcumin, 1 and 6 kDa CM respectively. Each data point is an average of 9 measurement for 1 kDa and 6 kDa CM, while it is an average of 3 measurement for free curcumin.*

For 6 kDa CM, a small mortality is seen at ∼4% for a concentration of 0.2 mg/mL, which increases to ∼11%. The curve decreases a little at 0.6 mg/mL to ∼10% mortality, followed by a rapid increase to ∼60% mortality. The standard deviation values differ for each point, with the highest at 0.8 mg/mL.

In parallel to the observation from the deduction in concentration for CRL 2429 (see figure 3.28), the mortality for U87 incubated with 6 kDa CM has decreased at the lower concentrations, and increased at the high concentration of 0.8 mg/mL. At 0.8 mg/mL 6 kDa CM has reached a mortality of 60%, in comparison to the 46% in figure 3.29; the same can be seen for 1 kDa CM. This difference is caused by the individual experiments; the plating of the cells and their stage of confluence can vary, causing differences in the amount and viability of cells between experiments. In order to avoid this influence on the results, the two experiments should have been performed on the same plate. Another area that may influence the results is the pipetting. Each well is pipetted manually, which can cause a deviation, since one does not pipette the same way twice. Again a high standard deviation is observed for 1 kDa CM for the entire curve. This can be caused by the previously mentioned conditions, and its observed poor ability to dissolve. 6 kDa CM is shown to increase more slowly in cytotoxic activity for concentrations of 0.2, 0.4 and 0.6 mg/mL, where it in figure 3.28 increases linearly, making it difficult to determine an optimal concentration, that damage less healthy cells than tumour cells.

From the observations done in the above figures 3.27, 3.28, 3.29 and 3.30 it can be deduced that 6 kDa CM has a lower cytotoxic activity when incubated with CRL 2429 than 1 kDa CM, making it favourable by not damaging healthy cells and still retaining a high cytotoxicity when incubated with tumour cells. All the graphs show that curcumin loaded in PVP polymer

increase the cytotoxic activity of curcumin by more than what is observed for free curcumin. This corresponds to the observations seen in the fluorescent images, that the cellular uptake of curcumin enhances when encapsulate in PVP polymer. The same effect was seen in the study by Yang et al. [46] and Liu et al. [55].

3.3.2 Empty micelles

3.3.2.1 Cell line U87

Figure 3.31 shows the results from the cytotoxicity assay using U87 incubated with 6 kDa empty micelles and free curcumin at concentrations of 1, 0.1, 0.01 and 0.001 mg/mL. On the graph two data set can be seen, where the cell have been incubated with free curcumin and 6 kDa empty micelles. The curve for free curcumin shows a starting point of ∼7% mortality, which then increases to ∼27%. The curve then decreases to a mortality of ∼8% for concentrations 0.1 mg/mL. At a concentration of 1 mg/mL it has increased to ∼18% mortality. The standard deviation for free curcumin, which is most apparent, is located at 0.01 mg/mL.

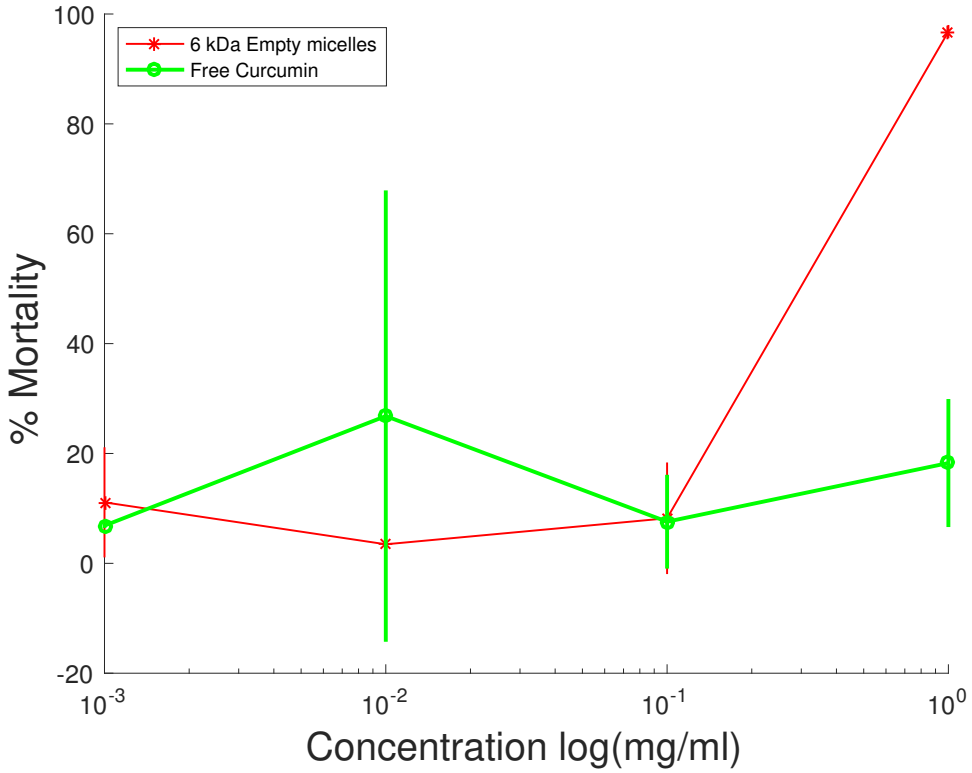

FIGURE 3.31: *The graph represent the mortality % of U87 cells after 24 hours incubation with different concentrations: 0.001, 0.01, 0.1 and 1 mg/mL of free curcumin and empty micelles. Each data point is an average of 9 measurement for empty micelles, while it is an average of 3 measurement for free curcumin.*

For 6 kDa empty micelles, the curve starts at ∼11% mortality and decreases to ∼3% for a concentration 0.01 mg/mL. At a concentration of 0.1 mg/mL an increase to ∼8% mortality is seen, after which it increases rapidly to 97% mortality. The standard deviation for 6 kDa empty micelles is only presented at 0.001 mg/mL and 0.1 mg/mL.

The empty micelles were synthesised using 6 kDa PVP polymer, because of its low cytotoxic activity towards CRL 2429, seen in the result of the cytotoxicity experiment in section 3.3.1. The empty micelles incubated with U87 cells illustrate an increase in cytotoxic activity, along with an increase in micelle concentration, comparable to the observations seen on the graphs for curcumin loaded micelles (see figure 3.29). The lower concentration maintains a molarity around 10%, corresponding to previous observations for U87 cells incubated with 6 kDa CM as seen on figure 3.29. The mortality of 97% for 1 mg/mL empty micelles incubated with U87 cells is very high, when compared to the results for 1 and 6 kDa CM observed in figure 3.29. The empty micelles have a cytotoxic activity almost twice as high. The curve for free curcumin remains at a mortality below 20%, with the exception of the sample with a concentration 0.01 of mg/mL, where the mortality is at 27%. The cause for the high mortality and standard deviation observed at 0.01 mg/mL, can be attributed to the poor solubility of curcumin in aqueous media. The DMEM 10% FBS 1% growth medium has a pH value of 7.4, making it a basic environment where curcumin is unstable and difficult to dissolve. Furthermore, a colour change in the media is an indication of chance in pH, meaning that the media has a higher pH when it appears dark red/purple and low pH at a yellow/brighter colour. The individual pipetting of the well can additionally have an influence on the high deviation observed.

The mortality for the empty micelles can be a result of their small and unstable structure. As previous discussed the empty micelles might possibly detach into monomers and aggregates when dissolved. The empty micelles, and subsequently the monomers and aggregates, can, because of their small size, easily diffuse into the cell, without being effected by the force at the nano-bio interface. The high concentration of empty micelles, might have damaged the cells membrane through numerous penetrations, resulting in a high mortality %, since the cytotoxicity assay measures LDH release from damaged cells. To investigate this implication further, other cytotoxicity assays could have been used to give a more precise estimation of all the micelles cytotoxic activity.

Figure 3.32 shows the concentration deduction results from the cytotoxicity assay using U87 cells incubated with 6 kDa empty micelles and free curcumin at different concentrations: 0.2, 0.4, 0.6 and 0.8 mg/mL. The curve for free curcumin shows an almost constant percentage of mortality. It has a constant mortality of ∼2% between concentration 0.2 - 0.4 mg/mL, after which a slight decrease to 1% at 0.6 mg/mL is seen. At concentration 0.8 mg/mL, the curve increases to its highest mortality at ∼6%. Here the largest standard deviation is seen for free curcumin.

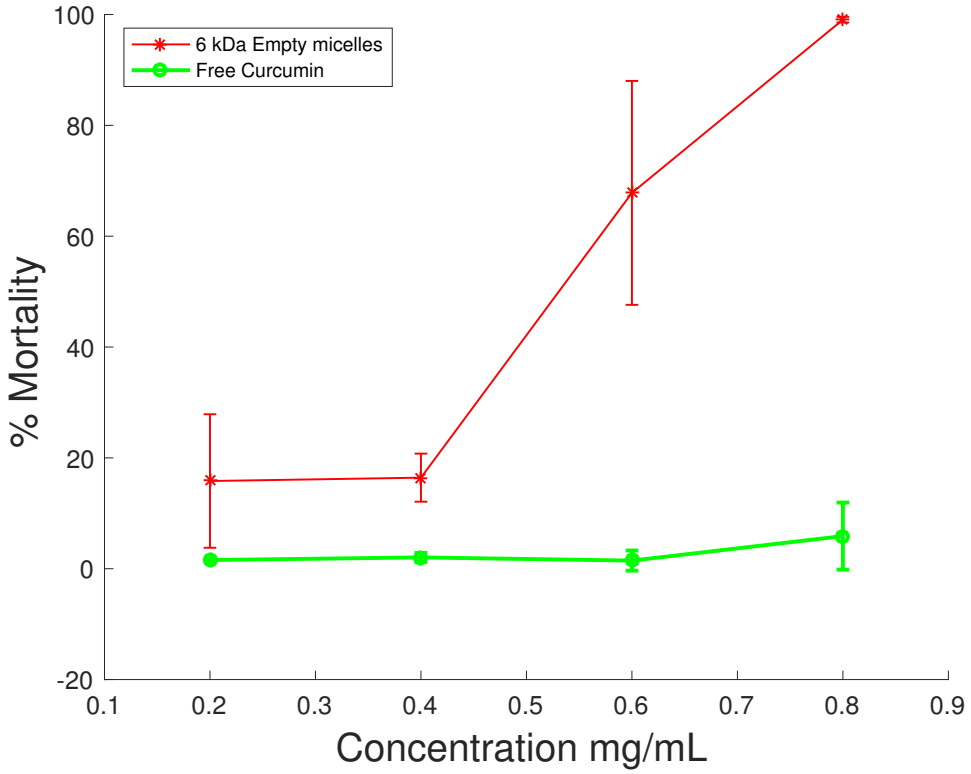

FIGURE 3.32: *The graphs represent the mortality % of U87 cells after 24 hours of incubation with different concentrations: 0.2, 0.4, 0.6 and 0.8 mg/mL of free curcumin and empty micelles. Each data point is an average of 9 measurement for empty micelles, while it is an average of 3 measurement for free curcumin.*

For 6 kDa empty micelles, a constant mortality of ∼16% is seen, between concentrations of 0.2 and 0.4 mg/mL. A rapid increase in mortality is shown at a concentration of 0.6 mg/mL, where it increases to ∼68%. The mortality continues to increase to a final value of ∼99%. The standard deviation differs for empty micelles; the largest is seen at a concentration of 0.6 mg/mL.

From the reduced concentration in figure 3.32, it is seen that the empty micelles almost linearly fit between the concentrations of 0.1 and 1 mg/mL in figure 3.31. The mortality of 99% is higher than observed in figure 3.31, possibly as a result of pipetting and dissolving the different concentrations. In contrast to the previous cytotoxicity assay experiments, figure 3.32 and figure 3.31 are performed on the same multiwell-plate, to prevent the influence of the stage of confluence between the samples. It cannot be avoided completely, only to some extent. The pipetting and the dissolving of the concentration are therefore more likely to be the cause of the observed deviations. The cytotoxic activity increases with the empty micelle concentration. The free curcumin remains at a mortality around 2%.

3.3.2.2 Cell line CRL 2429

Figure 3.33 shows the results from the cytotoxicity assay of CRL 2449 incubated with 6 kDa empty micelles and free curcumin at concentrations of 1, 0.1, 0.01 and 0.001 mg/mL. The curve for free curcumin starts with a mortality of ∼1%, followed by a slight decrease to ∼0%. At a concentration of 0.1 mg/mL, the curve increases to a mortality of ∼4% and decreases again to ∼3% at 1 mg/mL. The standard deviation values are very low for free curcumin, the highest being at 0.1 mg/mL.

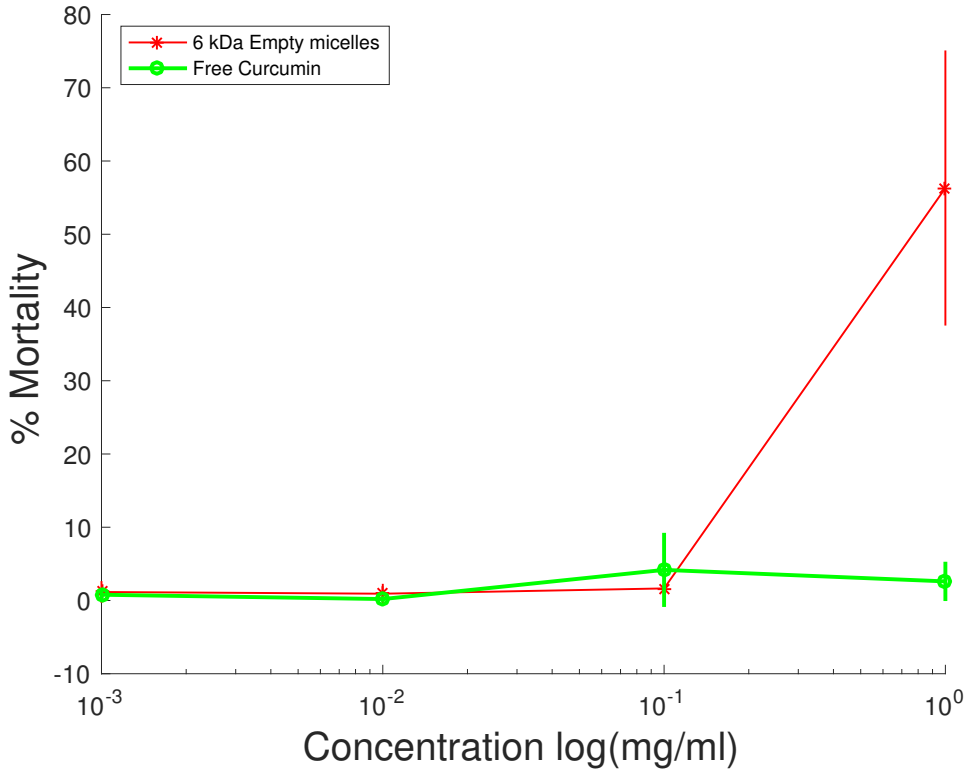

Figure 3.33: *The graph represent the mortality % of CRL 2429 cells after 24 hours incubation with different concentrations: 0.001, 0.01, 0.1 and 1 mg/mL of free curcumin and empty micelles. Each data point is an average of 9 measurement for empty micelles, while it is an average of 3 measurement for free curcumin.*

For the 6 kDa empty micelles, the curve shows an almost constant mortality percentage at ∼1% for the lowest concentrations: 0.001, 0.01 and 0.1 mg/mL. Between concentrations 0.1 and 1 mg/mL a rapid increase to ∼56% mortality is seen. The highest standard deviation seen for 6 kDa empty micelles is at 1 mg/mL.

The 6 kDa empty micelles incubated with CRL 2429 cells exhibit a constant cytotoxic activity for the low concentrations, which are low in comparison to figure 3.31 and figure 3.27. The highest mortality for the empty micelles is 56%, resulting in a lower cytotoxic activity in CRL 2429 cells, compared to U87 cells, with almost 40%. Therefore, the empty micelles have as little cytotoxic activity as a drug delivery carrier. The same was concluded in the study by Yang et al. [46], whose experiments spanned over 48 hours. Free curcumin, as previously seen, maintains its low cytotoxic activity below 10%. It can be concluded that the individual pipetting is probably the cause of the standard deviation observed.

As previously mentioned, the concentration of the micelles is investigated further, by looking at some concentrations between 0.1 and 1 mg/mL. This reduction of the concentration is seen in figure 3.34. Figure 3.34 shows the results from the cytotoxicity assay using CRL 2429 cells and 6 kDa empty micelles at concentrations of 0.2, 0.4, 0.6 and 0.8 mg/mL, as well as free curcumin. On the graph, two data set can be seen, where the cells have been incubated with free curcumin and 6 kDa empty micelles for 24 h. The 6 kDa empty micelles curve has a starting point at ∼7% mortality, followed by a somewhat linear increase. At a concentration of 0.4 mg/mL the mortality has reached ∼18%, and increases further to ∼27% at 0.6 mg/mL. The final increase leaves the mortality at ∼51%. The standard deviation is large and different for each point.

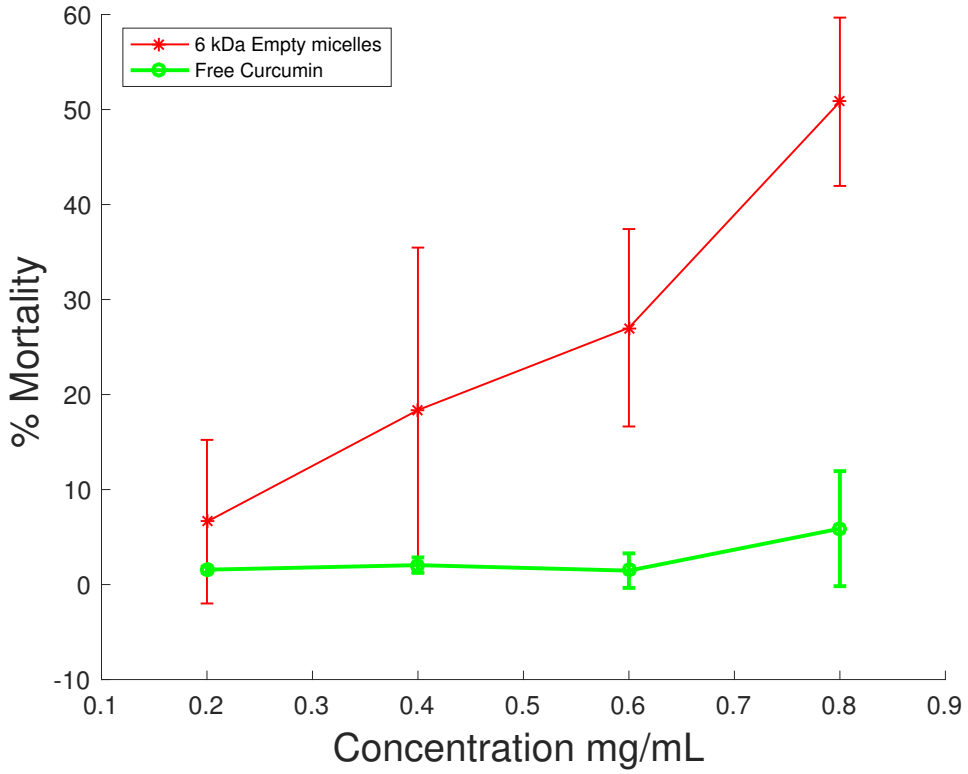

FIGURE 3.34: *The graph represent the mortality % of CRL 2429 cells after 24 hours incubation with different concentrations: 0.2, 0.4, 0.6 and 0.8 mg/mL of free curcumin and empty micelles. Each data point is an average of 9 measurement for empty micelles, while it is an average of 3 measurement for free curcumin.*

The curve for free curcumin has an exponential increase for each data point, with a start at ∼2% mortality at a concentration of 0.2 mg/mL. It then increases to ∼4% at 0.4 mg/mL and further to ∼6% at 0.6 mg/mL, before it ends at ∼16% mortality. The standard deviation increases with the increase in concentration.

The empty micelle concentrations between 0.1 and 1 mg/mL are similar to figure 3.32, with a lower cytotoxic activity. The empty micelles have a linear mortality increase, which increases with the concentration of micelles. The final mortality of the micelles in figure 3.34 is a little lower than observed for 1 mg/mL in figure 3.33 and rises slightly at 0.2 mg/mL, making the curve follow the curve for the empty micelles in figure 3.33. In contrast to the previous cytotoxicity Assay, experiments seen in figure 3.34 and figure 3.33 were performed on the same multiwell-plate, to prevent the influence of the stage of confluence. High standard deviation values are observed for all the point in the empty micelles curve, which is as previously stated most likely caused by pipetting errors and dissolving errors. The free curcumin shows a little increase in cytotoxic activity, but remains below 20%.

3.4 Flow cytometric analysis

In order to further investigate the endocytosis routes for the micelles, experiments have been conducted with a flow cytometer and two endocytosis inhibitors: dynasore hydrate and sodium azide. The seeded cells were pre-incubated with the inhibitors for a specific time, followed by incubation with 6 kDa CM for 30 min, before being trypsinated, the process of which is described in section 2.2.7. In the following figures 3.35, 3.36, 3.37 and 3.38 the data collected from the flow cytometer is presented as two-dimensional dot plots and a one-dimensional graph.

In figure 3.35 the two-dimensional dot-plot of the flow cytometer data for cell line CRL 2429 is shown. The plot represents the distribution of cells based upon their relative size and internal complexity. The relative size is represent by the axis FSC and internal complexity by the axis SSC. Figure 3.35 shows an overlay of all the samples, to identify the cells based on their morphology. An area of the cells has been outlined by the ellipses and is called P1; this area is used for further investigation. The remaining cells observed in the left corner are presumed to be cell residues, particles from the media or other residues in the samples. Each sample has its own colour to separate them.

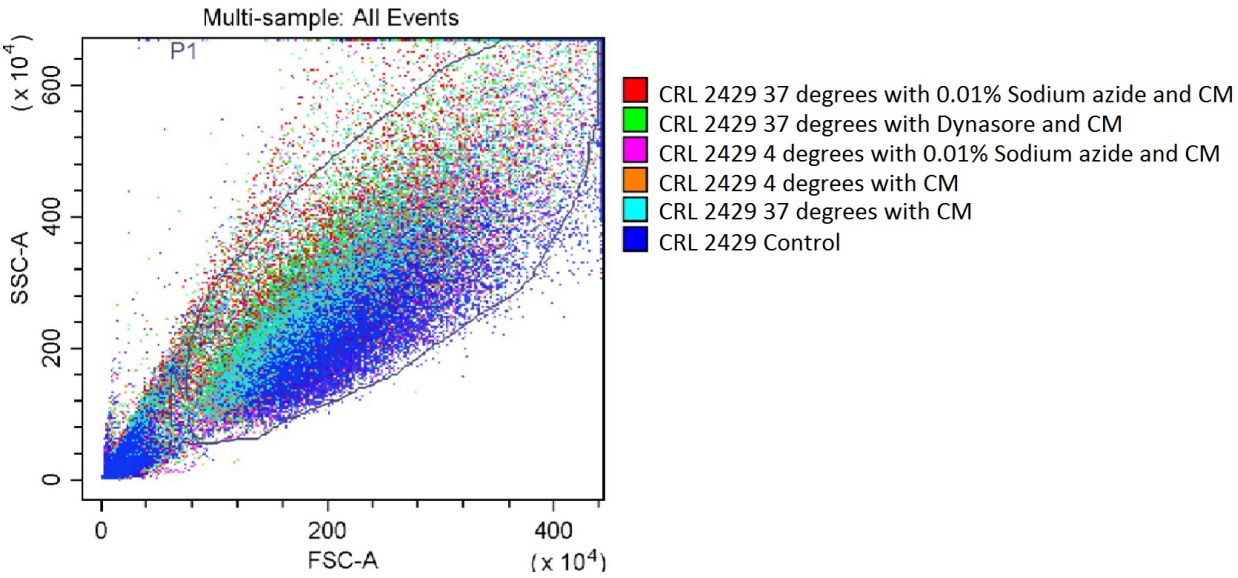

Figure 3.35: *The 2D dot-plot represents the distribution of CRL 2429 cells based upon their relative size and internal complexity. The CRL 2429 cells have been pre-incubated with the endocytosis inhibitor dynasore at 37°C and sodium azide at 4 and 37°C for 30 min. Afterwards the samples have been incubated with 1 mg/mL 6 kDa CM for 30 min (see section 2.2.7). Each sample is illustrated with their own colour. An area has been outlined and is referred to as P1, which is used for further investigation.*

In figure 3.36 the two-dimensional dot-plot for cell line U87 is observed. The plot is an overlay of all the U87 samples, used to identify cells based on their morphology. An area of interest has been outlined by the ellipses and is called P3; this area of cells will be used for further examination. The cells left out of the ellipses are considered cell residues, particles from the media or other residues in the samples. Each sample has their own colour to differentiate them.

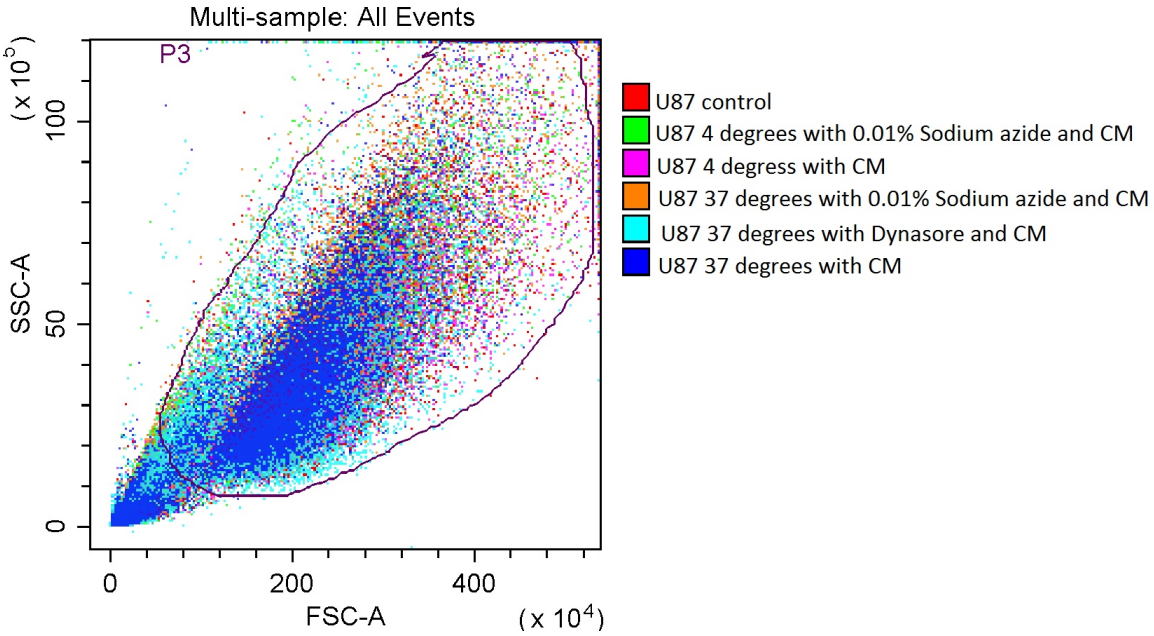

FIGURE 3.36: *The 2D dot-plot represents the distribution of U87 cells based upon their relative size and internal complexity. The U87 cells have been pre-incubated with the endocytosis inhibitor dynasore at 37°C and sodium azide at 4 and 37°C for 30 min. Afterwards have the samples been incubated with 0.5 mg/mL 6 kDa CM for 30 min (see section 2.2.7). Each sample has been illustrated with their own colour. An area has been outlined and is referred to as P3, which is used for further investigation.*

When comparing the two dot-plots, a small difference in complexity is observed between CRL 2429 and U87. The U87 cells show a higher internal complexity than CRL 2429, which is probably because of its star-shaped structure. CRL 2429 have a more elongated circular shape, which does not result in much side scattering.

From the cells in outlined areas P1 and P3 in figure 3.35 and 3.36, the presence of curcumin in the cells is determined. The presence of curcumin in the cell lines is shown from the fluorescent intensity distribution in the cells, in relation to the counted cells, which are plotted in a histogram. The histograms represent the fluorescent intensity distribution of the cells, and each histogram is an overlay of all the samples. The histogram overlays are seen in figures 3.37 and 3.38.

In figure 3.37 the fluorescent intensity of the CRL 2429 cells is illustrated, in relation to the counted cells. From figure 3.37 it is seen that the control sample has a lower intensity than the samples incubated with curcumin. The remaining sample that has been incubated at a different temperature and with different inhibitors show no significant changes in intensity. There is a small difference in the intensity between the sample incubated with only 6 kDa CM, at 4 and 37 °C.

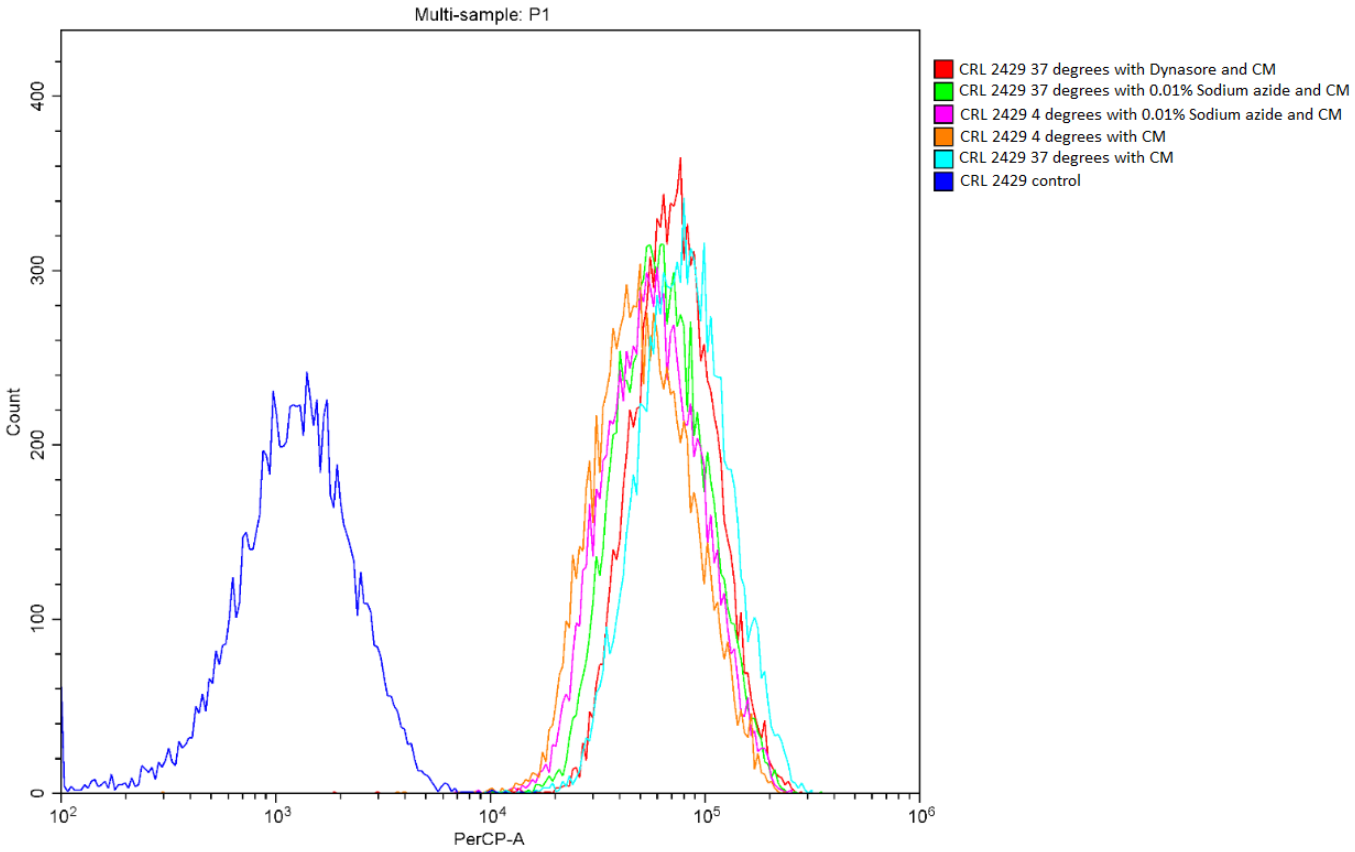

Figure 3.37: *The histogram represents the fluorescent intensity of the CRL 2429 cells pre-incubated with the endocytosis inhibitor dynasore at 37°C and sodium azide at 4 and 37°C for 30 min. The histogram is obtained from the cells seen outlined in figure 3.35. Each sample has been illustrated with its own colour.*

The results observed in figure 3.37 now show a significant difference in fluorescent intensity, which might be caused by the high concentration of 1 mg/mL of 6 kDa CM. The cells may have been saturated by the micelles, and will therefore not show any indications of hindered endocytosis. As a result of this observation, the concentration was lowered to 0.5 mg/mL for the experiments performed on the cell line U87.

In figure 3.38 the fluorescent intensity of the U87 cells is illustrated, in relation to the counted cells. From figure 3.38 a more defined difference in fluorescent intensity is seen. The cells incubated at 4°C are seen to have a lower intensity than the cells incubated at 37°C. The sodium azide does not express an influence on the cells. The cells incubated with dynasore shows the large change in intensity, and the control sample has a lower intensity than the samples incubated with curcumin.

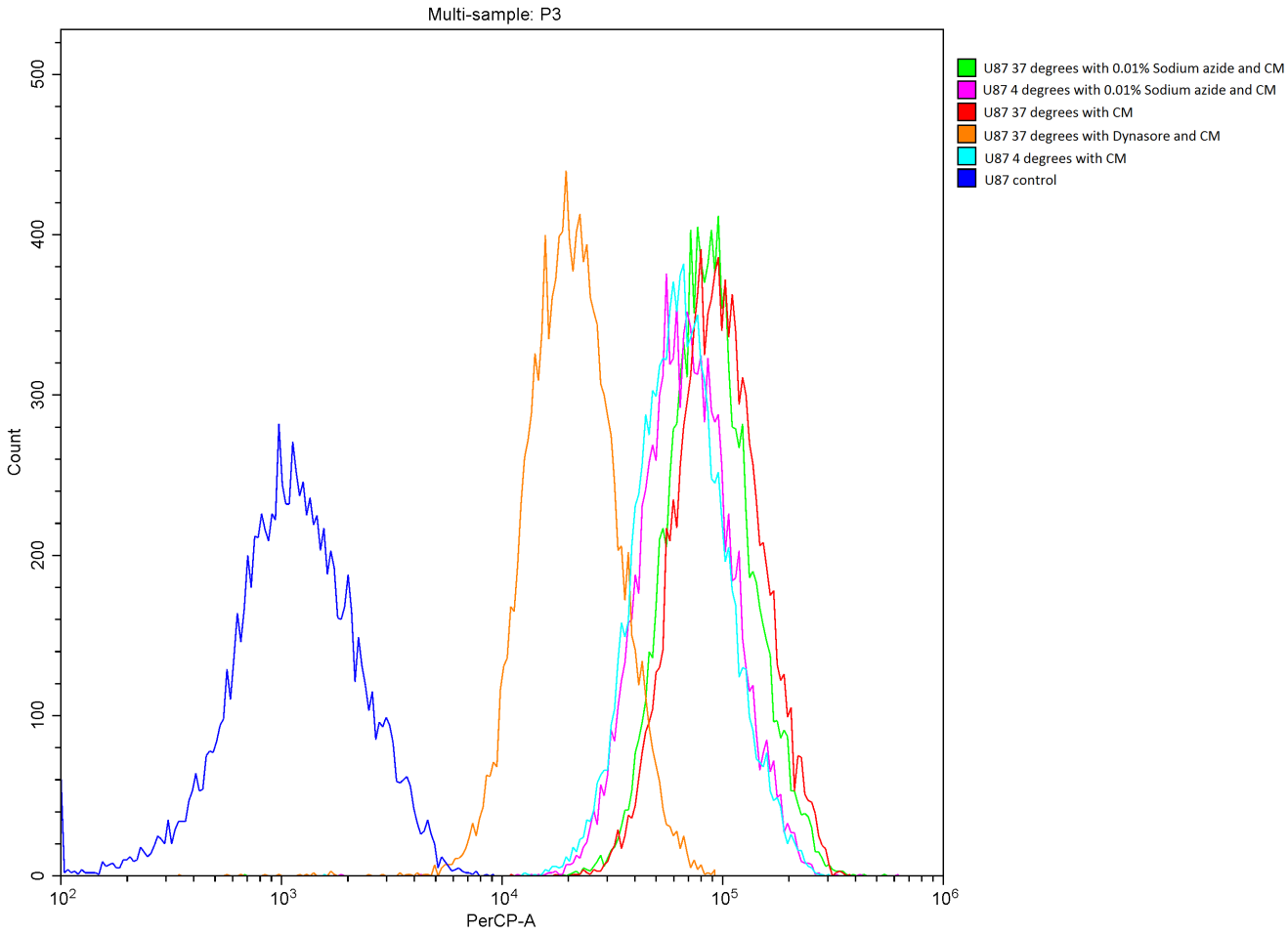

FIGURE 3.38: *The histogram represents the fluorescent intensity of the U87 cells pre-incubated with the endocytosis inhibitor dynasore at 37°C and sodium azide at 4 and 37°C for 30 min. The histogram is obtained from the cells seen outlined in figure 3.36. Each sample has been illustrated with their own colour.*

From the results seen in figure 3.38 a minimal difference in the fluorescent intensity between the samples incubated at 4 and 37°C is seen. The sodium azide shows no significantly influence on the samples, when comparing to the samples incubated only with 6 kDa CM. Theoretically, sodium azide is an inhibitor for oxidative phosphorylation - metabolic pathways to which cells use enzymes to realise energy to form ATP. By hindering oxidative phosphorylation, sodium azide is hindering the ATP syntheses in the cells and thereby inhibiting endocytosis mechanisms. Therefore, an obvious difference in fluorescent intensity was expected between the samples incubated with 6 kDa CM and the sample pre-incubated with sodium azide. The same goes for the minimal difference seen between 4 and 37 °C. By lowering the temperature, the process of oxidative phosphorylation is slowed down due to the enzymes activity, which is slower at lower temperatures, making the entire process of ATP syntheses slower, and with it the endocytosis mechanisms. A reason for the minimal change in intensity observed between 4 and 37°C, might possibly be caused by a minimal change in temperature. To obtain a temperature of 4°C the culture flask was placed in a refrigerator; after obtaining 100 % confluence, the temperature of the flask were not checked before removing the growth medium and adding 3 ml of uncooled 0.01% sodium azide solution. By replacing half of the flasks volume with uncooled solution, the temperature might not have remained at 4°C. By adding an additional 3 mL of uncooled 6 kDa CM solution after 30 min, the temperature will be changed again and might not reach a temperature of 4°C.

When comparing the difference between 4 and 37°C in figures 3.37 and 3.38, a large difference is seen between the figures. Figure 3.37 show no sign of being influence by the temperature , where a more defined difference is seen in figure 3.38; here the culture flask was placed in the refrigerator some time before adding solution, to obtain the equilibrated temperature. The intensity differences are however still lower than expected. A more precise approach is therefore needed, to maintain the temperature at 4°C in the culture flask and have the same temperature for the solutions added to the flask.

The largest difference in intensity is seen for dynasore at 37° incubated with U87 cells. This result implies that dynasore inhibits the uptake of 6 kDa CM and that the U87 cells use dynamin dependent endocytosis, which includes Clathrin-dependent endocytosis.

4. Conclusion

It has been shown to be possible to synthesise small polymeric micelles of PVP polymer. Three different variations of PVP polymeric micelles were synthesised using curcumin, chloroform and 1 and 6 kDa PVP polymers. From studies of the micelles, using NanoSight and a multimode AFM, their sizes where determined. The synthesis resulted in 1 and 6 kDa curcumin micelles, with diameters of 80 nm and 142 nm respectively and empty micelles with diameters of 41 nm. The PVP polymers size and the solvents curcumin and chloroform showed to have important influence on the micelles size. The empty micelles synthesised using chloroform and 6 kDa polymer where 4 times smaller than the 6 kDa curcumin micelles and unstable. The use of chloroform contributed to unstable empty micelles, because of the minimal hydrophobic interactions at core. Where the curcumin loaded micelles have stronger hydrophobic interactions, attributed to curcumin. The lyophilised powders texture also showed to be influenced by the polymer size. The texture of 1 kDa curcumin micelles was flakier compared to the 6 kDa micelles; they were more smooth and uniformly structured, which also showed to influence their ability to dissolve. The Nanosight results showed that proper preparations of the micelles was necessary, in order to remove remains of curcumin, polymer and micelle aggregates. From the AFM images it was concluded that the curcumin micelles and empty micelles appeared to have different surface charges. The empty micelles were positively charged and collapsed on the freshly cleaved mica substrates, while the curcumin micelles were negatively charged and collapsed on the APTMS modified mica substrate.

The drug delivery application of the micelles was studied using optical fluorescent microscopy, to determine the cellular uptake of curcumin and overcome curcumins poor solubility. The results showed that the polymeric micelles enhance the cellular uptake of curcumin, compared to free curcumin, making curcumin micelles a promising formulation of curcumin to overcome the poor solubility. Furthermore, the micelles pathways into the cells lines were studied by inhibiting the endocytosis mechanisms, by treating the cells with the endocytic inhibitor dynasore and receptor endocytosis inhibitor worthmaninn. For both cell lines, the inhibitors showed no variations in fluorescent intensity of curcumin uptake in the cells. Additionally, investigation into the endocytosis mechanisms was conducted through the use of flow cytometric analysis. The 6 kDa curcumin micelles were incubated with sodium azide at 4 and 37°C, to hinder ATP synthesis, and thereby some of the endocytosis mechanisms. The results were inconclusive; only a small variation was observed between 4 and 37°C for cell line Glioblastoma (U87).

The cytotoxicity of the micelles was studied using a cytotoxicity assay, through a mortality %. The results showed a high cytotoxic activity for both 1 and 6 kDa curcumin micelles over a range of concentrations in both cell lines, compared to free curcumin. The high cytotoxic activity for the micelles in fibroblast cells is not ideal, but 6 kDa curcumin micelles showed a lower activity than 1 kDa curcumin micelles, thereby making them more favourable, since they had the highest cytotoxic activity in glioblastoma cells, inhibiting their growth more. Empty micelles cytotoxic activity was also studied, to determine the cytotoxic activity of the PVP polymer. For glioblastoma cells, the mortality was almost 100%, whereas fibroblast cells showed mortality at 60%, indicating a little cytotoxic activity as a drug carrier.

Bibliography

[1] Peter Boyle and Bernard Levin. *World Cancer Report 2008.* International Agency for Research on Cancer (IARC), 2008.

[2] Quanyin Hu, Wujin Sun, Chao Wang, and Zhen Gu. Recent advances of cocktail chemotherapy by combination drug delivery systems. *Advanced Drug Delivery Reviews*, 2015.

[3] American Cancer Society. The history of cancer, December 2014. `http://www.cancer.org/acs/groups/cid/documents/webcontent/002048-pdf.pdf` download on 3rd of september.

[4] James P. Allen. Edwin smith papyrus, 1600 B.C. `https://ceb.nlm.nih.gov/proj/ttp/flash/smith/smith.html` read on 3rd of september case 45.

[5] American Cancer Society. The history of cancer. American Cancer Society, December 2014. `http://www.cancer.org/cancer/cancerbasics/thehistoryofcancer/`.

[6] Michael Baum, Harvey Schipper, and Eva A. Turley. A new biological framework for cancer research. *The Lancet*, October 1996.

[7] J.C. Coffey, J.H. Wang, M.J.F. Smith, D. Bouchier-Hayes, T.G. Cotter, and H.P. Redmond. Excisional surgery for cancer cure: therapy at a cost. *The Lancet - Oncology*, 4:760 – 768, December 2003.

[8] Annette Rösler, Guido W.M. Vandermeulen, and Harm-Anton Klo. Advanced drug delivery devices via self-assembly of amphiphilic block copolymers. *Advanced Drug Delivery Reviews*, 53:95–108, 2001.

[9] Marie-Christine Jones and Jean-Christophe Leroux. Polymeric micelles +/- a new generation of colloidal drug carrier. *European Journal of Pharmaceutics and Biopharmaceutics*, 48:101–111, 1999.

[10] Kewal K. Jain. *Drug Delivery Systems*, volume 437 of *Methods in Molecular Biology.* Humana Press, 2008.

[11] Bassam Abdul Rasool Hassan. Overview on drug delivery system. Pharmaceutica Analytica Acta, December 2012. `http://www.omicsonline.org/overview-on-drug-delivery-system-2153-2435.1000e137.pdf` Download on 18 Aug 2016.

[12] Pamella S. Ochoa, José A. Vega, and Paul Holder. *Concepts in Sterile Preparations and Aseptic Technique.* Jones & Bartlett learning, 2015.

[13] Neha Gulati and Himanshu Gupta. Parenteral drug delivery - a review. *Recent Patents on Drug Delivery & Formulation*, 5:133 – 145, 2011.

[14] V. P. Torchilin. Drug targeting. *Pharmaceutical Sciences*, 11:s81 – s91, 2000.

[15] Monika Schäfer-Korting, editor. *Drug Delivery - Passive and Active Drug Targeting - Drug Delivery to Tumors as an Example*, volume 197 of *Handbook of experimental pharmacology*. Springer, 2010.

[16] Cancer.net. Side- effects of chemotherapy, August 2015. `http://www.cancer.net/navigating-cancer-care/how-cancer-treated/chemotherapy/side-effects-chemotherapy` read on september 1st 2016.

[17] Xinming Li, John Tsibouklis, Tingting Weng, Buning Zhang, Guoqiang Yin, Guangzhu Feng, Yingde Cui, Irina N. Savina, Lyuba I. Mikhalovska, Susan R. Sandeman, Carol A. Howel, and Sergey V. Mikhalovsky. Nano carriers for drug transport across the blood–brain barrier. *Journal of drug targeting*, 2016.

[18] William M. Pardridge. Blood–brain barrier delivery. *Drug discovery today*, 2007.

[19] National Cancer Insitute. Targeted cancer therapies, April 2014. `https://www.cancer.gov/about-cancer/treatment/types/targeted-therapies/targeted-therapies-fact-sheet` Read December 7 2016.

[20] Vladimir Muzykantov and Vladimir P. Torchilin, editors. *Biomedical Aspects of Drug Targeting*. Springer, 2002.

[21] Aditi M. Jhaveri and Vladimir P. Torchilin. Multifunctional polymeric micelles for delivery of drugs and sirna. *Frontiers in - Pharmacology*, 5(77), April 2014.

[22] Vladimir P. Torchilin and Vladimir S. Trubetskoy. Which polymers can make nanoparticulate drug carriers long-circulating? *Advanced Drug Delivery Reviews*, 1995.

[23] Sharon Sagnella and Calum Drummond. Drug delivery - a nanomedicine approach. *Australasian Biochemist*, 2012.

[24] Vladimir P. Torchilin. Structure and design of polymeric surfactant-based drug delivery systems. *Elsevier - Journal of controlled release*, 73:137–172, 2001.

[25] Julio San Román, Alberto Gallardo, and Belén Levenfeld. Polymeric drug delivery systems. *Advanced Materials*, 7(no. 2):203 –208, 1995.

[26] Vladimir P. Torchilin. Targeted pharmaceutical nanocarriers for cancer therapy and imaging. *American Association of Pharmaceutical Scientists*, 9:E128 – E147, May 2007.

[27] John A. Pelesko. *Self Assembly - The science of things that put themselves together*. chapman & Hall/CRC - Taylor &Francis Group, 207.

[28] Hand-Jürgen Butt, Karlheinz Graf, and Michael Kappl. *Physics and Chemistry of interface*. WILEY-VCH, 2003.

[29] Carlota Oliveira Rangel-Yagui, Adalberto Pessoa Junior, and Leoberto Costa Tavares. Micellar solubilization of drugs. *J Pharm Pharmaceut Sci*, 2005.

[30] Elena V. Batrakova, Tatiana K. Bronich, Joseph A. Vetro, and Alexander V. Kabanov. Polymer micelles as drug carriers. *University of Nebraska Medical Center homepage*, 2016. `http://www.unmc.edu/pharmacy/faculty/pharmaceutical-sciences/docs/v5.pdf`.

[31] Jubo Liu, Yuehua Xiao, and Christine Allen. Polymer–drug compatibility; a guide to the development of delivery systems for the anticancer agent, ellipticine. *Journal of pharmaceutical sciences*, 2004.

[32] Masayuki Yokoyama. Clinical applications of polymeric micelle carrier systems in chemotherapy and image diagnosis of solid tumors. *Journal of Experimental & Clinical Medicine*, 4:151–158, 2011.

[33] Marina Talelli, Cristianne J.F. Rijcken, Sabrina Oliveira, Roy van der Meel, Paul M.P. van Bergen en Henegouwne, Twan Lammers, Cornelus F. van Nostrum, and Gert Stormand Wim E. Hennink. Nanobody — shell functionalized thermosensitive core-crosslinked polymeric micelles for active drug targeting. *Journal of Controlled Release*, 151:183–192, 2011.

[34] Manas Chanda. *Introduction to Polymer Science and Chemistry - A Problem-Solving Approach*. CRC Press, 2013.

[35] Lesia Whitehurst. Polytails and urban tumble weaves: The chemistry of synthetic hair fibers. Yale National Initiative, 2016. `http://teachers.yale.edu/curriculum/viewer/initiative_11.05.10_u`viewed 26/05/16.

[36] Nobuhiro Nishiyama and Hiroyasu Takemoto. *Encyclopedia of Polymeric Nanomaterials - polymeric micelles*. Springer, 2014.

[37] Andre E. Nell, Lutz Mädler, Darrell Velegol, Tian Xia, Eric M. V. Hoek, Ponisseril Somasundaran, Fred Klaessig, Vince Castranova, and Mike Thompson. Understanding biophysicochemical interactions at the nano-bio interface. *Nature Materials*, June 2009.

[38] Gaurav Sahaya, Daria Y. Alakhovaa, and Alexander V. Kabanov. Endocytosis of nanomedicines. *Journal of Controlled Release*, 145:182–195, August 2010.

[39] Talaro Chess. *Foundations in Microbiology - basic principles*. McGraw - Hill, eighth edition, 2012.

[40] Alberts B, Johnson A, Lewis J, and et al. *Molecular Biology of the Cell - Transport into the Cell from the Plasma Membrane: Endocytosis*. New York- Garland Science, 2002. Available from `http://www.ncbi.nlm.nih.gov/books/NBK26870/`.

[41] Georgi Yordanov. *Colloid and Interface Chemistry for Nanotechnology - Advanced Strategies for Drug Delivery in Nanomedicine*. CRC Press, 2014.

[42] Paolo Verderio, Svetlana Avvakumova, Giulia Alessio, Michela Bellini, Miriam Colombo, Elisabetta Galbiati, Serena Mazzucchelli, Jesus Peñaranda Avila, Benedetta Santini, and Davide Prosperi. Delivering colloidal nanoparticles to mammalian cells - a nano–bio interface perspective. *Advanced Healthcare Materials*, 3(7):957 –976, July 2014.

[43] Jr Harry W Schroeder and Lisa Cavacini. Structure and function of immunoglobulins. *Allergy and Clinical Immunology*, 125(S41 - S52), 2010.

[44] David G. Capco and Yongsheng chen, editors. *Nanomaterial - Impacts on Cell Biology and Medicine*. Springer, 2014.

[45] Ayush Verma, Oktay Uzun, Yuhua Hu, Ying Hu, Hee-Sun Han, Nicki Watson, Suelin Chen, Darrell J. Irvine, and Francesco Stellacci. Surface-structure-regulated cell-membrane penetration by monolayer-protected nanoparticles. *Nature Materials*, 2008.

[46] Xi Yang, Zhaojun Li, Ning Wang, Ling Li, Linjiang Song, Tao He, Lu Sun, Zhihan Wang, Qinjie Wu, and Na Luoand Cheng Yiand Changyang Gong. Curcumin-encapsulated polymeric micelles suppress the development of colon cancer in vitro and in vivo. *Scientific Reports*, 2015.

[47] P.N. Ravindran. *Turmeric - The genus Curcuma.* CRC Press, 2007.

[48] Preetha Anand, Ajaikumar B. Kunnumakkara, Robert A. Newman, and Bharat B. Aggarwa. Bioavailability of curcumin: Problems and promises. *Molecular Pharmaceutics*, 2007.

[49] Preetha Anand, Sherin G. Thomas, Ajaikumar B. Kunnumakkara, Chitra Sundaram, Kuzhuvelil B. Harikumar, Bokyung Sung, Sheeja T. Tharakan, Krishna Misra, Indira K. Priyadarsini, Kallikat N. Rajasekharan, and Bharat B. Aggarwal. Biological activities of curcumin and its analogues (congeners) made by man and mother nature. *Biochemical Pharmacology*, 2008.

[50] Ajay Goel, Ajaikumar B. Kunnumakkara, and Bharat B. Aggarwal. Curcumin as "curecumin": From kitchen to clinic. *Biochemical Pharmacology*, 2008.

[51] Bharat B. Aggarwal, Indra D. Bhatt, Haruyo Ichikawa, Kwang Seok Ahn, Gautam Sethi, Santosh K. Sandur, Chitra Natarajan, Navindra Seeram, and Shishir Shishodia. *Turmeric - The genus Curcuma - Chapter 10; Curcumin -Biological and Medicinal Properties.* CRC Press, 2007.

[52] Preetha Anand, Chitra Sundaram, Sonia Jhurani, Ajaikumar B. Kunnumakkara, and Bharat B. Aggarwal. Curcumin and cancer: An "old-age" disease with an "age-old" solution. *Cancer Letters*, 2008.

[53] Hiroshi Aoki, Yasunari Takada, Seiji Kondo, Raymond Sawaya, Bharat B. Aggarwal, and Yasuko Kondo. Evidence that curcumin suppresses the growth of malignant gliomas in vitro and in vivo through induction of autophagy: Role of akt and extracellular signal-regulated kinase signaling pathways. *Molecular Pharmaceutics*, 2007.

[54] Zengshuan Ma, Azita Haddadi, Ommoleila Molavi, Afsaneh Lavasanifar, Raymond Lai, and John Samuel. Micelles of poly(ethylene oxide)-b-poly(-caprolactone) as vehicles for the solubilization, stabilization, and controlled delivery of curcumin. *journal of biomedical materials research*, 2007.

[55] Lei Liu, Lu Sun, Qinjie Wu, Wenhao Guo, Ling Li, YiShan Chen, Yuchen Li, Changyang Gong, Zhiyong Qian, and Yuquan Wei. Curcumin loaded polymeric micelles inhibit breast tumor growth and spontaneous pulmonary metastasis. *International Journal of Pharmaceutics*, 2012.

[56] D. E. Pegg. Viability assays for preserved cells, tissues, and organs. *Cyrobiologi*, 1989.

[57] Martin J. Stoddart, editor. *Mammalian Cell Viability - Methods and Protocols.* Humana Press, 2011.

[58] Steven A. Altman, Lisa Randers, and Govind Rao. Comparison of trypan blue dye exclusion and fluorometric assays for mammalian cell viability determinations. *Biotecnologi*, 1993.

[59] Promega. Cytotox-one homogeneous membrane integrity assay. TECHNICAL BULLETIN, November 2009. https://dk.promega.com/~/media/files/resources/protocols/technical%20bulletins/101/cytotox-one%20homogeneous%20membrane%20integrity%20assay%20protocol.pdf.

[60] American Brain Tumor Association. Glioblastoma and malignant astrocytoma, 2016. http://www.abta.org/brain-tumor-information/types-of-tumors/glioblastoma.html.

[61] Cancer Research UK. Diagram of an astrocyte - a type of glial cell cruk, December 2015. https://commons.wikimedia.org/wiki/File:Diagram_of_an_astrocyte_-_a_type_of_glial_cell_CRUK_029.svgfilehistory.

[62] Felipe de Almeida Sassi and Algemir Lunardi Brunetto and Gilberto Schwartsmann and Rafael Roesler and Ana Lucia Abujamra. Glioma revisited: From neurogenesis and cancer stem cells to the epigenetic regulation of the niche. *Journal of Oncology*, 2012.

[63] Fonnet E. Bleeker, Remco J. Molenaar, and Sieger Leenstra. Recent advances in the molecular understanding of glioblastoma. *Journal of Neuro-Oncology*, 2012.

[64] Richard M. Young, Aria Jamshidi, Gregory Davis, and Jonathan H. Sherman. Current trends in the surgical management and treatment of adult glioblastoma. *Annals of Translational Medicine*, 2015.

[65] Bruce Alberts, Alexander Johnson, Julian Lewis, Martin Raff, Keith Roberts, and Peter Walter. *Molecular Biology of the Cell*. GS Garland Science, 2002.

[66] Ryan T. Kendall and Carol A. Feghali-Bostwick. Fibroblasts in fibrosis- novel roles and mediators. *Frontiers -In Pharmacology*, 2014.

[67] CellnTec. Primary human dermal fibroblasts. http://cellntec.com/products/skin/fibroblast-cells/ December 19 2016.

[68] Nano vision group. Prof. michael shtilman, phd. http://www.nanovisiongroup.com/people/prof-michael-shtilman-phd/?la=en.

[69] Malvern Instruments. Nanoparticle tracking analysis, 2016.

[70] K. Kjoller, V. B. Ehngs, Q. Zhong, and D. Innlss. Fractured polymer/silica fiber surface studied by tapping mode atomic force microscopy. *Surface Science Letters*, 1993.

[71] Zhiguo Liu, Zhuang Li, Hualan Zhou, Gang Wei, Yonghai Song, and Li Wang. Observation of the mica surface by atomic force microscopy. *Micron*, 2005.

[72] BD Biosciences. Introduction to flow cytometry: A learning guide, April 2000. http://medicine.yale.edu/labmed/cellsorter/start/Introduction_66019_284_10028.pdf.

[73] Tom Kirchhausen, Eric Macia, and Henry E. Pelish. Use of dynasore, the small molecule inhibitor of dynamin, in the regulation of endocytosis. *Methods Enzymol*, 2008.

[74] Longfa Koua, Jin Suna, Yinglei Zhaib, and Zhonggui Hea. The endocytosis and intracellular fate of nanomedicines: Implication for rational design. *Asian Journal of Pharmaceutical Sciences*, 2013.

A. AFM images for statistics

A representation of the 6 kDa CM AFM images used for section 3.1.4. In figure A.1 the first six AFM images are seen. All the images are from the same sample, but from different places on its surface.

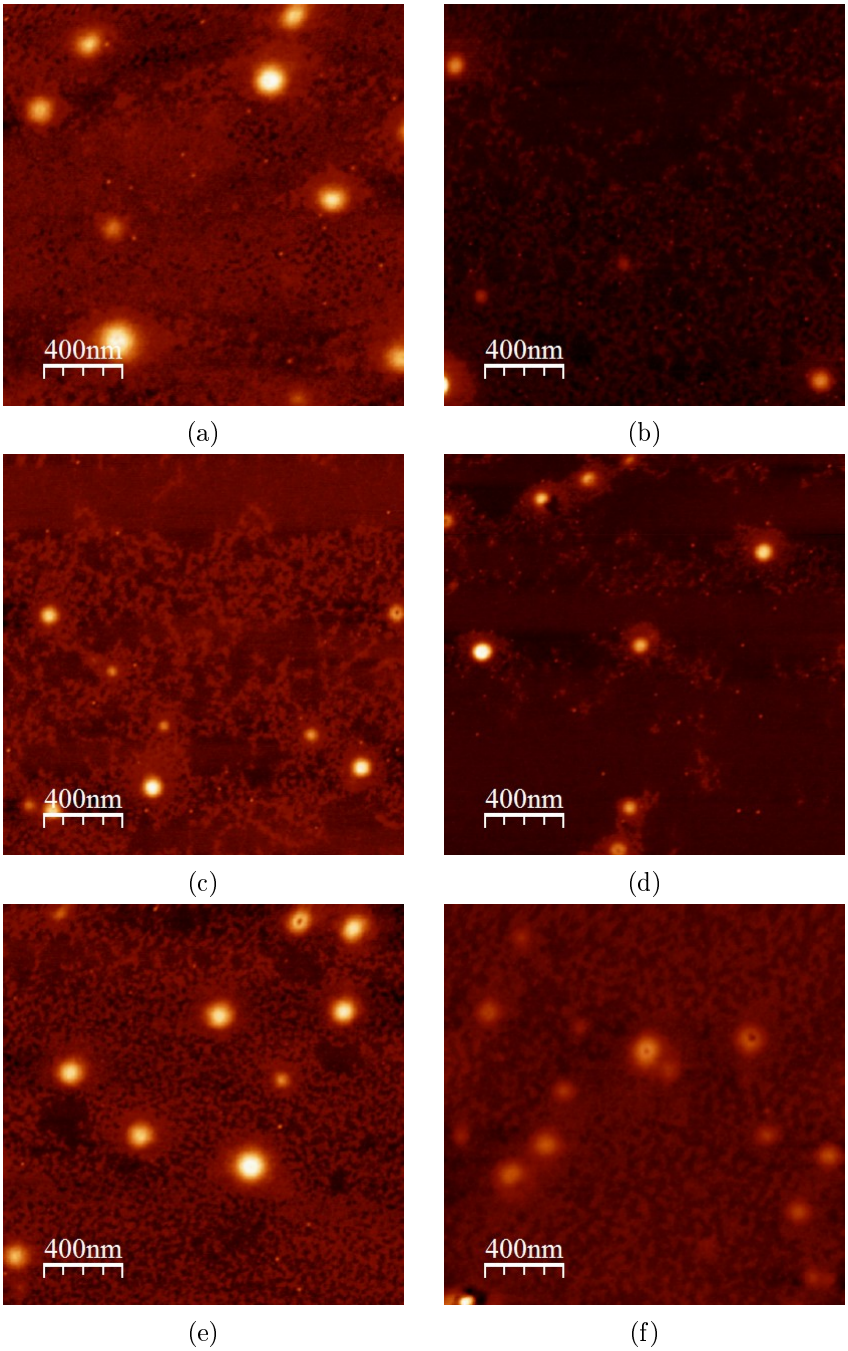

(a) (b) (c) (d) (e) (f)

FIGURE A.1: *The AFM images used for height and radius distribution analysis. The AFM images represents 6 kDa CM treated with ultrasound, which have been drop deposited on a freshly cleaved mica substrate, see section 2.2.3.1.*

In figure A.2 the last four AFM images are seen. All the images are from the same sample, but from different places on its surface.

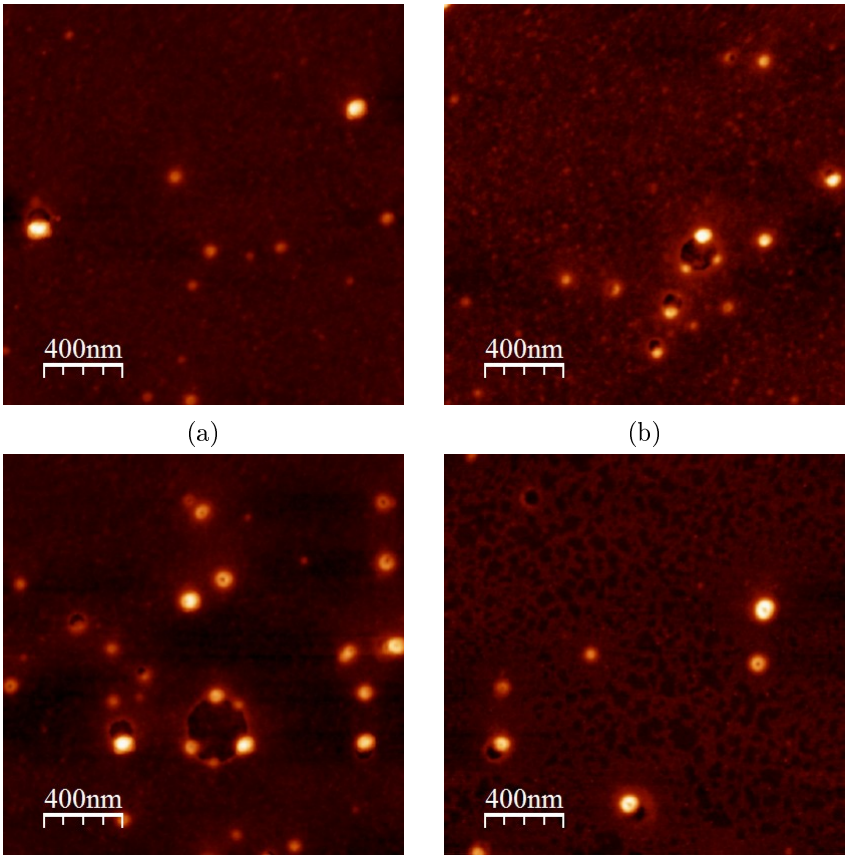

Figure A.2: *The AFM images used for height and radius distribution analysis. The AFM images represents 6 kDa CM treated with ultrasound, which have been drop deposited on a freshly cleaved mica substrate, see section 2.2.3.1.*

B. Light micro-graphs

From each cytotoxicity assay produced, have there been taking light micro-graphs from before and after 24 h incubation with 1 kDa CM, 6 kDa CM and 6 kDa empty micelles. This chapter represent some of the micro-graphs, two images for each point seen in the cytotoxicity graph 3.27 in section 3.3, one for before and after incubation. The remaining light micro-graphs can be found on the attached CD.

The micro-graph images in figure B.2 represent the points for 1 kDa CM.

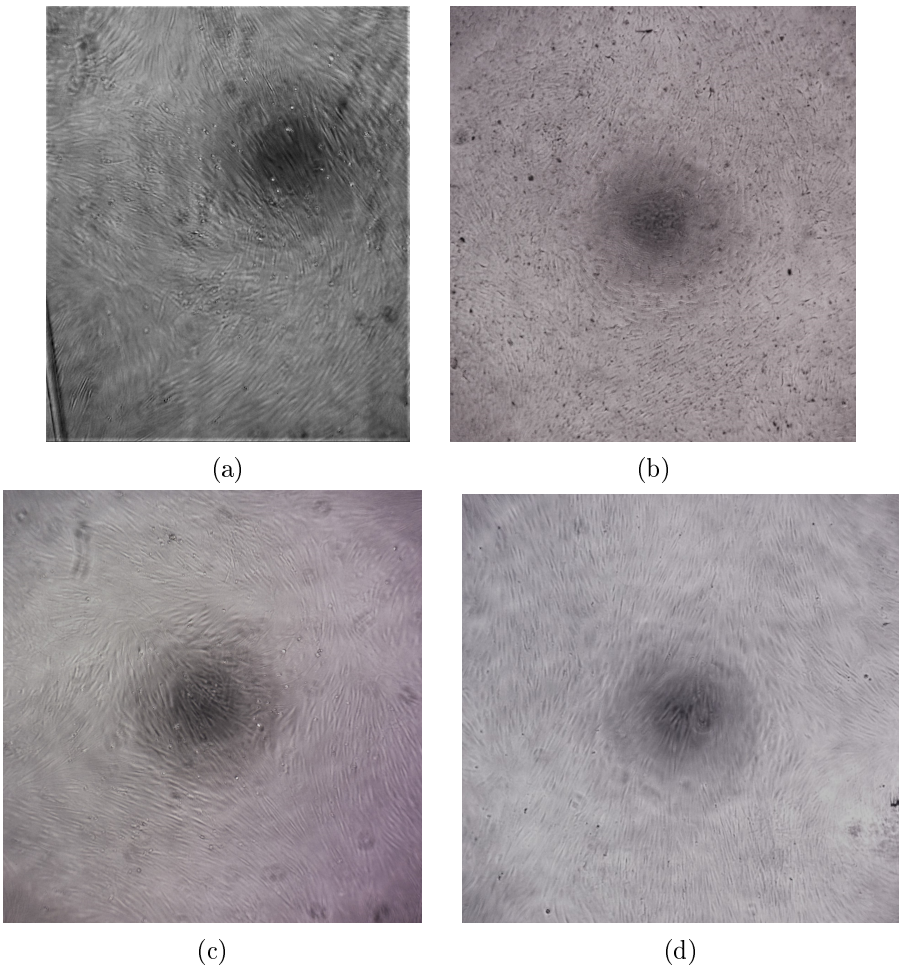

FIGURE B.1: *The 1 kDa CM curve in figure 3.27. (a) and (c) represent the light micro-graphs before incubation with 1 kDa CM, while (b) and (d)represent after.*

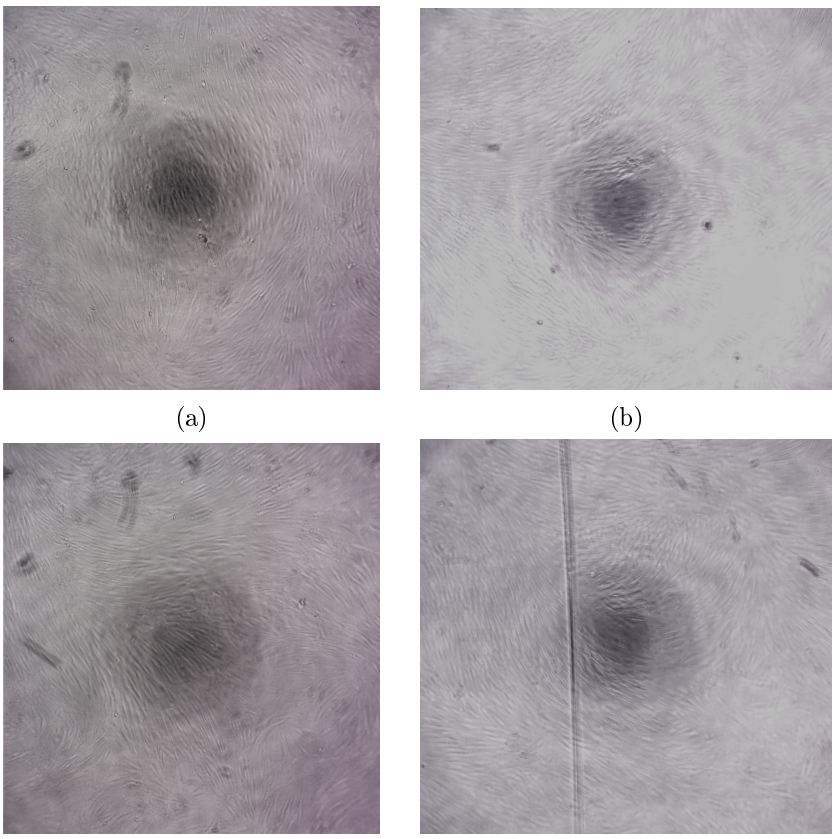

(a) (b)

(c) (d)

Figure B.2: *The 1 kDa CM curve in figure 3.27. (a) and (c) represent the light micro-graphs before incubation with 1 kDa CM, while (b) and (d)represent after.*

The micro-graph images in figure B.4 represent the points for 6 kDa CM.

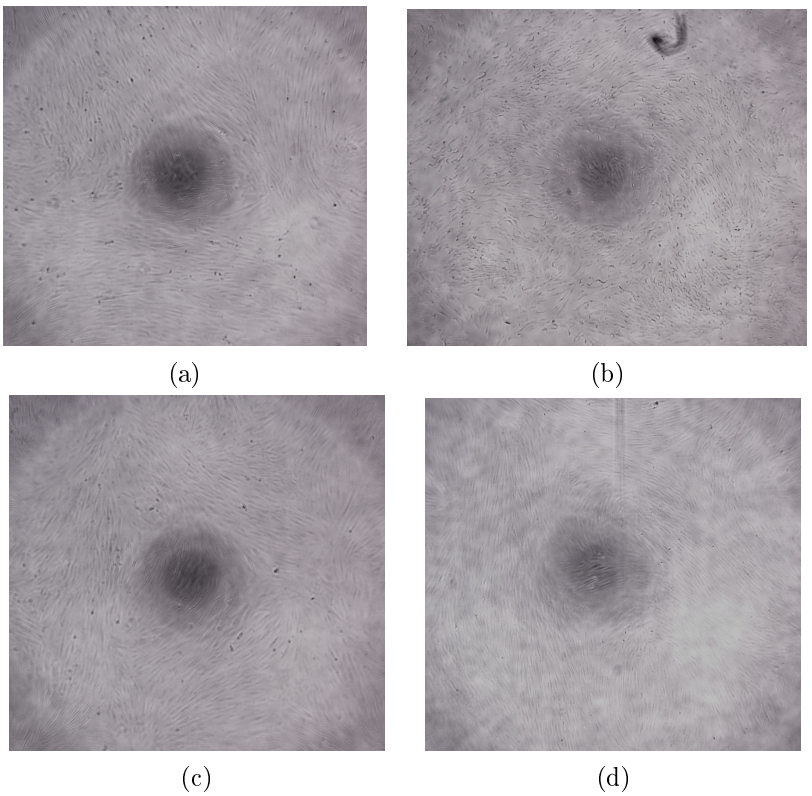

FIGURE B.3: *The 6 kDa CM curve in figure 3.27. (a) and (c) represent the light micro-graphs before incubation with 6 kDa CM, while (b) and (d) represent after.*

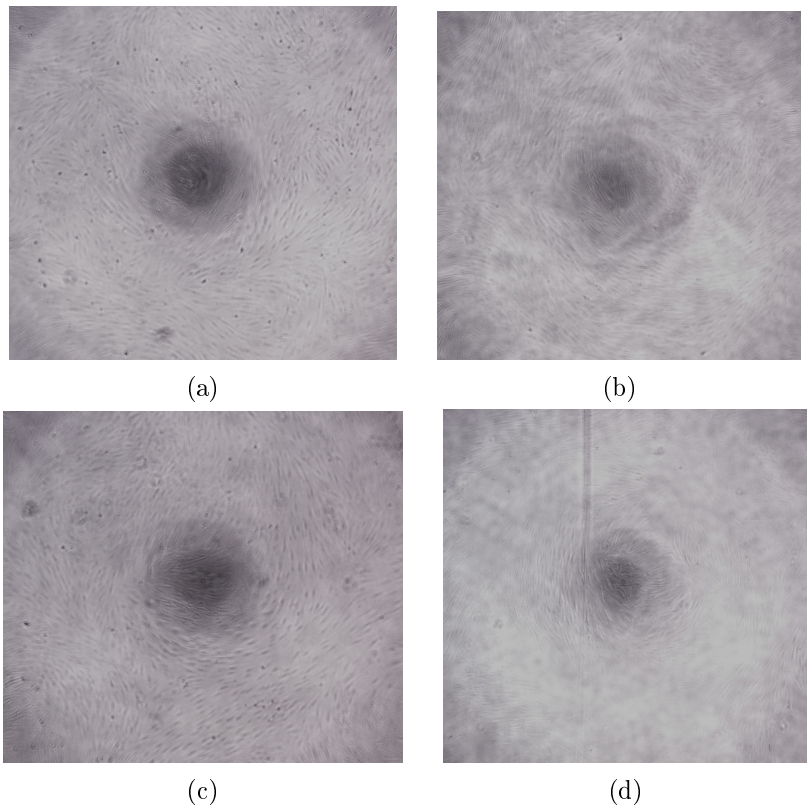

FIGURE B.4: *The 6 kDa CM curve in figure 3.27. (a) and (c) represent the light micro-graphs before incubation with 6 kDa CM, while (b) and (d) represent after.*

The micro-graph images in figure B.5 represent the points for free curcumin.

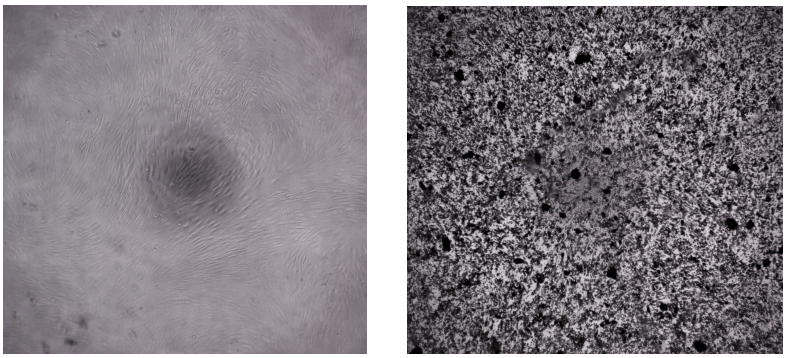

(a) (b)

Figure B.5: *The free curcumin point in figure 3.27. (a) represent the light micro-graphs before incubation with free curcumin, while (b) represent after.*